

ISTANBUL TECHNICAL UNIVERSITY ★ GRADUATE SCHOOL OF SCIENCE
ENGINEERING AND TECHNOLOGY

**SYNTHESIS OF ZnO AND Si NANOWIRES FOR
THE FABRICATION OF 3RD GENERATION SOLAR CELLS**



Ph.D. THESIS

Elif PEKSU

Department of Physics Engineering

Physics Engineering Programme

JULY 2019

ISTANBUL TECHNICAL UNIVERSITY ★ GRADUATE SCHOOL OF SCIENCE
ENGINEERING AND TECHNOLOGY

**SYNTHESIS OF ZnO AND Si NANOWIRES FOR
THE FABRICATION OF 3RD GENERATION SOLAR CELLS**

Ph.D. THESIS

**Elif PEKSU
(509122115)**

Department of Physics Engineering

Physics Engineering Programme

Thesis Advisor: Assoc. Prof. Dr. Hakan KARAAĞAÇ

JULY 2019

İSTANBUL TEKNİK ÜNİVERSİTESİ ★ FEN BİLİMLERİ ENSTİTÜSÜ

**ÜÇÜNCÜ NESİL GÜNEŞ PİLLERİNİN
ÜRETİMİ İÇİN ZnO VE Si NANOTELLERİN SENTEZLENMESİ**

DOKTORA TEZİ

**Elif PEKSU
(509122115)**

Fizik Mühendisliği Anabilim Dalı

Fizik Mühendisliği Programı

Tez Danışmanı: Doç. Dr. Hakan KARAAĞAÇ

TEMMUZ 2019

Elif PEKSU, a Ph.D. student of ITU Graduate School of Science Engineering and Technology student ID 509122115, successfully defended the thesis entitled “SYNTHESIS OF ZnO AND Si NANOWIRES FOR THE FABRICATION OF 3RD GENERATION SOLAR CELLS”, which she prepared after fulfilling the requirements specified in the associated legislations, before the jury whose signatures are below.

Thesis Advisor : **Assoc. Prof. Dr. Hakan KARAAĞAÇ**

Istanbul Technical University

Jury Members : **Prof. Dr. Serap GÜNEŞ**

Yıldız Technical University

Assoc. Prof. Dr. Esra ALVEROĞLU DURUCU

Istanbul Technical University

Assoc. Prof. Dr. Zuhale ER

Istanbul Technical University

Assoc. Prof. Dr. Kadir ERTÜRK

Tekirdağ Namık Kemal University

Date of Submission : 28 June 2019

Date of Defense : 19 July 2019





To my lovely family,



FOREWORD

Throughout my PhD studies, countless people helped and supported me, both academically and privately. First of all, I am deeply grateful to my advisor Assoc. Prof. Dr. Hakan KARAAĞAÇ for his wide knowledge and contribution, the opportunities he has provided. He patiently supported and guided me. I could not have achieved my current level of success without his strong support. It has been a pleasure to work with him all these years.

I wish to express my deepest gratitude to my committee members Prof. Dr. Serap GÜNEŞ and Assoc. Prof. Dr. Esra ALVEROĞLU DURUCU for the constructive and helpful comments during my PhD studies.

Most importantly, I am greatly indebted to my wonderful family, my father Mehmet PEKSU, my mother Nermin PEKSU and my brother Murat PEKSU who supported me with love and understanding at every step of my life. Thank you all for your unwavering support.

I specially would like to thank my dearest friends Tansu ERSOY, Gülay KARAKAYA, Rıdvan ERGUN, Yunus BOYA, Tuğçe ÖZTÜRK, Sanaz GHAFURI, Elnaz GHAFURI, Meltem MENEMEN, Gökhan İPEK, Bihter ZEYTUNCU, Furkan KURUOĞLU, Birsen KESİK ZEYREK, Kadriye GÜNEÇ and to my project partners Makbule TERLEMEZOĞLU, Özge GÜLLER, Eray HUMALI in TÜBİTAK 315M401 project.

I would also like to thank BAP-39349, TÜBİTAK 114F251 and 315M401 projects for their financial supports throughout my PhD studies.

July 2019

Elif PEKSU
(Physicist)



TABLE OF CONTENTS

	<u>Page</u>
FOREWORD	ix
TABLE OF CONTENTS	xi
ABBREVIATIONS	xiii
SYMBOLS	xv
LIST OF TABLES	xvii
LIST OF FIGURES	xix
SUMMARY	xxiii
ÖZET	xxv
1. INTRODUCTION	1
1.1 Purpose of Thesis	5
1.2 Literature Review	7
2. SYNTHESIS OF ZnO NANOWIRES AND THEIR PHOTOVOLTAIC APPLICATION: ZnO NANOWIRES/AgGaSe₂ THIN FILM CORE-SHELL SOLAR CELL	11
2.1 Introduction	11
2.2 Experimental	13
2.3 Results and Discussion	15
2.4 Conclusions	25
2.5 Acknowledgements	25
3. DOPING AND ANNEALING EFFECTS ON STRUCTURAL, ELECTRICAL AND OPTICAL PROPERTIES OF TIN-DOPED ZINC-OXIDE THIN FILMS	27
3.1 Introduction	27
3.2 Material and Methods.....	28
3.3 Results and Discussion.....	29
3.4 Conclusions	42
3.5 Acknowledgements	43
4. A THIRD GENERATION SOLAR CELL BASED ON WET-CHEMICALLY ETCHED Si NANOWIRES AND SOL-GEL DERIVED Cu₂ZnSnS₄ THIN FILMS	45
4.1 Introduction	45
4.2 Material and Methods.....	47
4.3 Results and Discussion.....	48
4.4 Conclusions	56
5. CHARACTERIZATION OF ONE-STEP DEPOSITED Cu₂ZnSnS₄ THIN FILMS DERIVED FROM A SINGLE CRYSTALLINE POWDER	57
5.1 Introduction	57
5.2 Experimental	58
5.3 Results and Discussion.....	60
5.3.1 Cu ₂ ZnSnS ₄ (CZTS) crystal	60
5.3.1.1 Structural analysis	60

5.3.1.2 Hall and photoconductivity measurements	62
5.3.2 Cu ₂ ZnSnS ₄ (CZTS) thin films	64
5.3.2.1 Structural analysis	64
5.3.2.2 Morphological analysis	68
5.3.2.3 Optical analysis	69
5.3.2.4 Hall and photoconductivity measurements	71
5.4 Conclusion	74
5.5 Acknowledgements	75
6. CONCLUSIONS.....	77
REFERENCES	85
CURRICULUM VITAE	97



ABBREVIATIONS

1D	: One Dimensional
AFM	: Atomic Force Microscope
AGS	: AgGaSe ₂
CIGS	: CuIn _x Ga _{1-x} Se ₂
CZTS	: Cu ₂ ZnSnS ₄
EDXA	: Energy Dispersive X-ray Analysis
ITO	: Indium Tin Oxide
NW	: Nanowire
PET	: Polyethylene Terephthalate
SEM	: Scanning Electron Microscope
SLG	: Soda Lime Glass
XRD	: X-Ray Diffraction



SYMBOLS

α	: Absorption Coefficient
β	: Full width at half maximum of diffraction peak
d	: Thickness
E_a	: Activation Energy
E_g	: Energy Band Gap
FF	: Fill Factor
I	: Current
J_o	: Saturation Current Density
J_{sc}	: Short Circuit Current Density
k	: Boltzmann's Constant
η	: Power Conversion Efficiency
R	: Reflectance
σ	: Conductivity
T	: Transmittance
V	: Voltage
V_{oc}	: Open Circuit Voltage



LIST OF TABLES

	<u>Page</u>
Table 3.1 : Lattice parameters obtained following the Rietveld refinement.....	31
Table 3.2 : Electrical resistivity values measured for as-grown and annealed Sn doped ZnO thin films.....	42
Table 5.1 : Atomic ratios and percentages of the content elements for CZTS crystals prepared with Cu-poor and Zn-rich content.	61
Table 5.2 : Calculated conductivity parameters from Hall measurement for Cu-poor CZTS crystal.....	64
Table 5.3 : Atomic percentages and ratios of the content elements for 600 nm thick CZTS films prepared with Cu-poor and Zn-rich.	65
Table 5.4 : XRD peak positions associated with the recorded values for the fabricated CZTS thin films and those provided by JCPDS reference cards.....	66
Table 5.5 : The calculated band gaps for the CZTS samples annealed at different temperatures.....	70



LIST OF FIGURES

	<u>Page</u>
Figure 2.1 : Top- and tilted-view SEM images of ZnO nanowires grown on (a) soda lime glass, (b) indium tin oxide, (c) polyethylene terephthalate (PET), and Silicon (Si) by using hydrothermal technique.	15
Figure 2.2 : Top-view SEM images of ZnO nanowires grown on soda lime glass substrates for growth times of (a) 1.5 h and (b) 3 h.....	16
Figure 2.3 : Top-view SEM images of ZnO nanowires synthesized on ZnO seed layers (on soda lime glass substrates (SLG)) deposited by (a) sol-gel and (b) sputtering technique. Inset figure shown in part (a) presents the AFM image recorded for ZnO seed layer on SLG substrate deposited by sol-gel route.	17
Figure 2.4 : (a) SEM images showing the elemental mapping for the constituent element of as-grown AgGaSe ₂ thin film: Uncolored image at left top shows the bare surface of thin film before the elemental mapping; the one at the center shows combined elemental mapping. (b) EDXA pattern and calculated atomic percentage of constitute elements in as-grown AgGaSe ₂ thin film deposited onto soda-lime glass substrate.	18
Figure 2.5 : X-ray diffraction pattern obtained for as-grown and AgGaSe ₂ thin film annealed between 300 and 550 °C.	19
Figure 2.6 : (a) Transmittance spectra obtained for as-grown and AgGaSe ₂ thin film annealed at different temperatures (400, 500 and 550 °C) and (b) absorption coefficient (α) and photon energy (h ν) relation for AGS thin film annealed at 550 °C.....	20
Figure 2.7 : (a) The variation of conductivity as a function of temperature for as-grown and AgGaSe ₂ thin film annealed at 500 and 550 °C. (b) Temperature dependent conductivity of AgGaSe ₂ thin film annealed at 550 °C under different illumination intensities (between 20 and 115 mW/cm ²).....	21
Figure 2.8 : (a) Cross-sectional view SEM image of the structure of a fully fabricated n-ZnO-NWs/p-AgGaSe ₂ core-shell solar cell. (b) Current (I)-voltage (V) characteristic of the fabricated solar cell recorded under dark condition and (c) under 100 mW/cm ² of simulated solar illumination. .	23
Figure 3.1 : XRD pattern recorded for (a) undoped and Sn doped ZnO thin films with (b) (zoom in) their (002) preferred peak.....	30
Figure 3.2 : Rietveld refinements for 500 °C annealed (a) undoped and (b) 1.5 % doped ZnO thin films.....	31
Figure 3.3 : XRD patterns recorded for (a) ZnO, (b-d) Sn doped ZnO thin films at different Sn concentrations (0.5-3.0 %) and annealed in the temperature range between 150 °C and 500 °C, (e) Rietveld refinements for 250 °C annealed and 3.0 % doped ZnO thin film.	33
Figure 3.4 : SEM micrographs obtained for (a) 0 % (ZnO), (b) 0.5 %, (c) 1.5 % and (d) 3.0 % Sn doped ZnO thin films and films of (a-d) as-grown, (a ₂ -d ₂) annealed at 250 °C and (a ₃ -d ₃) 500 °C.	34

Figure 3.5 : 3-D AFM images with scanning area of $1.5 \times 1.5 \mu\text{m}^2$ recorded for as-grown (a) undoped, (b) 0.5 %, (c) 1.5 % and (d) 3.0 % Sn doped ZnO thin films.	36
Figure 3.6 : 3-D AFM images recorded for (a) undoped, (b) 0.5 %, (c) 1.5 % and (d) 3.0 % Sn doped ZnO thin films annealed at 500 °C, scanning area $1.5 \times 1.5 \mu\text{m}^2$	37
Figure 3.7 : Transmittance spectra of as-grown and post-annealed ZnO thin films with doping concentrations of (a) 0 %, (b) 0.5 %, (c) 1.5 %, (d) 3.0 %. The insets show reflectance spectra obtained for the respective doping concentrations and annealing temperatures.	38
Figure 3.8 : The band gap determination, $(\alpha h\nu)^2$ versus photon energy (h ν) relation, for as-grown ZnO and Sn doped ZnO thin films at different doping concentrations.	39
Figure 3.9 : The band gap determination for as-grown and post annealed 1.5 % Sn doped ZnO thin film.	40
Figure 4.1 : Schematic representation of the fabricated solar cell by decoration of Si NWs with a thin layer of CZTS.	48
Figure 4.2 : (a) The XRD patterns recorded for as-grown and annealed CZTS thin film deposited on SLG substrate. (b) Raman spectra for the same CZTS film.	50
Figure 4.3 : Transmission spectrum for the CZTS annealed thin film deposited on SLG substrate. The inset figure presents the relationship of the absorption coefficient versus photon energy for the same CZTS thin film.	51
Figure 4.4 : (a - b) Top-view and tilted-view SEM images of the fabricated bare Si-NWs. (c - d) Top-view and tilted-view SEM images recorded for the Si-NWs decorated with a 600 nm thick CZTS layer. (e) XRD and (f) Raman scattering spectra of Si-NWs coated with the CZTS absorber layer.	52
Figure 4.5 : (a) The current (I) - voltage (V) characteristic of the fabricated n-Si-NWs/p-CZTS solar cell measured under both dark and AM 1.5G illumination. The inset figure presents the same characteristic shifted into the first quadrant. (b) Reflectance spectra recorded from the fabricated NW based solar cell and its planer counterpart. The zoomed-in reflectance spectrum of the device structure with NW configuration is shown as an inset figure. The SEM micrographs recorded for both device configurations are also given as inset images.	53
Figure 5.1 : (a) EDXA spectrum and (b) top-view SEM image recorded for the obtained CZTS powder. (c) Pictures of sliced wafers of the grown CZTS ingot.	60
Figure 5.2 : (a) X-Ray diffraction pattern and (b) Raman spectrum recorded for a CZTS crystal prepared with a Cu-poor content.	61
Figure 5.3 : Temperature dependent conductivity of CZTS crystals performed under dark and illumination (50 mW/ cm^2) conditions.	63
Figure 5.4 : A typical EDXA spectra recorded for CZTS thin films (annealed at 500 °C) deposited on soda lime glass substrates.	65
Figure 5.5 : (a) The XRD patterns and (b) Raman spectra recorded for as-grown and annealed (250 °C, 350 °C and 500 °C) CZTS films. Inset figure in part (b) represents the zoomed in version of Raman spectrum recorded for the as-grown CZTS thin film.	66

Figure 5.6 : AFM images recorded for CZTS thin films: (a) as-grown, and annealed at (b) 250 °C, (c) 350 °C, and (d) 500 °C. (e,f) Particle size analysis for CZTS film annealed 500 °C..... **69**

Figure 5.7 : (a) Reflectance and (b) transmittance spectra for as-grown and annealed CZTS thin films. (c) The optic band gap determination through the relation between the photon energy and absorption coefficient. **70**

Figure 5.8 : Variation of electrical conductivity of CZTS films annealed at 500 °C measured in dark and under illumination ($\sim 50 \text{ mW/cm}^2$) for the temperature range 100-400 K. **71**

Figure 5.9 : Temperature dependent (a_1 - a_2 and b_1 - b_2) mobility and (a_3 and b_3) hole concentrations of CZTS thin films annealed at 350 °C and 500 °C obtained from Hall Effect measurements performed in the temperature range of 100-400 K. **73**





SYNTHESIS OF ZnO AND Si NANOWIRES FOR THE FABRICATION OF 3RD GENERATION SOLAR CELLS

SUMMARY

Under the present study, ZnO and Si nanowires (NWs) were synthesized by simple and cost-effective techniques for the fabrication of new-generation (one-dimensional (1D) nanostructures based) solar cells by combining them with several optimal solar cell absorber layers.

Hydrothermal technique was preferred for the synthesis of dense arrays of ZnO NWs on a wide range of substrates including silicon, soda-lime glass (SLG), indium tin oxide (ITO) and polyethylene-terephthalate (PET). Results demonstrated that ZnO NWs can be successfully grown on any substrate that can withstand the growth temperature (~90 °C) and precursor solution chemicals. Results also showed that there was a strong impact of growth time and ZnO seed layer deposition route on the orientation, density, diameter and uniformity of the synthesized nanowires. Once the ZnO NWs were obtained with optimum quality, a core-shell n-ZnO-NWs/p-AgGaSe₂ (AGS) solar cell was then fabricated as their opto-electronic device application. To manage this, the synthesized ZnO NWs were homogeneously coated with a ~700 nm thick sputtered AGS layer, which exhibited a power energy conversion efficiency of 1.74 % under AM 1.5G illumination (100 mW/cm²).

In the second part of the study, ZnO was doped with Sn element which is located in the group IV in the periodic table in order to enhance electrical properties of ZnO seed layers. Sn doped ZnO thin films at different Sn content (of 0.5 % to 3.0 %) were successfully deposited on soda-lime glass substrates using RF/DC magnetron sputtering technique. The effects of doping concentration and annealing on structural, electrical, and optical properties of Sn doped ZnO thin films were determined in detail. XRD measurements not only revealed the deterioration of crystallinity but also a gradual shift of main peak position to higher values following the doping process. Following the annealing process at different temperatures (150, 250 and 500 °C) a drastic improvement in crystallinity of both doped and undoped ZnO films was observed. AFM measurements have shown that there is a significant modification in surface morphology following the doping process. The mulberry-like structures, for instance, were observed for the 3.0 % Sn doped ZnO film. The average transmittance in the visible range was found to be around 90 % for all the Sn-doped films after annealing at 500 °C. From the transmission and reflection measurements the band gap energies were calculated, which exhibited a decreasing trend with the increasing Sn content. The observed red-shift in band gap from 3.26 to 3.15 eV was attributed to the band gap shrinkage due to the generation of deep levels in the forbidden band gap following the doping process. It was also revealed that there was an increase in band gap with increase of annealing temperature. The lowest resistivity ($9.8 \times 10^{-3} \Omega \cdot \text{cm}$) measured at room temperature was recorded for the 1.5 % Sn-doped ZnO thin film after annealing at 250 °C.

Under another part of the present study, vertically well-aligned n-type Silicon nanowires (Si NWs) were successfully obtained via a simple and cost-effective fabrication route (i.e., electroless-etching technique). The derived Si NWs from an n-type Si-wafer were then incorporated into an absorber $\text{Cu}_2\text{ZnSnS}_4$ (CZTS) thin layer as an effort to accomplish a core-shell structured n-Si NW/p- $\text{Cu}_2\text{ZnSnS}_4$ solar cell. Single phase CZTS thin films, without any other secondary phases, have been successfully deposited on both soda lime glass substrates and Si NW arrays by sol-gel technique, which is known to be a simple and cost-effective fabrication approach. The formation of single-phase kesterite CZTS structure was proven by both X-ray diffraction and Raman analyses. X-ray diffraction and energy dispersive X-ray analysis studies have revealed that post-annealing process at 350 °C is a sufficient temperature for the growth of a stoichiometric mono-phase CZTS thin film. The band gap energy of the films was found to be 1.55 eV. The fabricated n-Si NWs/p-CZTS solar cell exhibited a power conversion efficiency of ~1.0 % under AM 1.5G. A solar cell based on Si NWs with this device configuration was reported for the first time in the present study. Therefore, we are confident that our research will serve as a base for future studies on these materials combination and this architecture based next-generation solar cells.

In the final part of this study, a new fabrication approach was chosen for the deposition of high quality mono-phase $\text{Cu}_2\text{ZnSnS}_4$ (CZTS) thin films that can be employed as optimal absorber layer for third generation solar cells. First Cu deficient and Zn rich CZTS single crystals were successfully grown by Bridgman technique. Following the investigation of structural and photo-electrical properties of the grown CZTS crystal, the powder extracted from it was evaporated through electron-beam technique for the fabrication of CZTS thin films by one-step deposition. Compositional analysis revealed that CZTS thin films were obtained with a composition stoichiometry very close to that measured for the crystal powder. Detailed XRD and Raman analyses have shown that the as-grown CZTS films have an amorphous matrix and then transform into a polycrystalline form with a mono-phase kesterite phase having (112) oriented plane direction following the post-annealing process at 500 °C. In addition, the optical analyses enabled us to calculate the optic band gap, which was found to be 1.50 eV for the CZTS film annealed at 500 °C. The conducted photo-electrical measurements revealed that CZTS thin films have good sensitivity to the visible light, which is essential for an absorber layer in the solar cell device structure. From the Hall measurements, the conductivity, mobility and hole carrier concentration values for the film annealed at 500 °C at room temperature were determined from the Hall measurement and calculated to be $\sim 5.1 \times 10^{-4} (\Omega \cdot \text{cm})^{-1}$, $1.22 \text{ cm}^2/\text{V} \cdot \text{s}$ and $2.6 \times 10^{15} \text{ cm}^{-3}$, respectively. Finally, from the temperature dependent conductivity measurements two acceptor levels located at 12 meV and 60 meV above the valance band were revealed and identified to be associated with the copper-vacancies, which was attributed to the formation of Cu-poor CZTS thin films.

ÜÇÜNCÜ NESİL GÜNEŞ PİLLERİNİN ÜRETİMİ İÇİN ZnO VE Si NANOTELLERİN SENTEZLENMESİ

ÖZET

Bu çalışmada, basit ve düşük maliyetli, solüsyon tabanlı yöntemler kullanılarak çinko oksit (ZnO) ve silikon (Si) nanoteller (NT) sentezlendi. Sentezlenen bu tek boyutlu nanoyapılar uygun soğurucu katmanla (kalkopirit veya kesterit) birleştirilerek yeni nesil (nanoyapılar kullanılarak elde edilen) güneş hücrelerinin üretimi sağlandı.

Çinko oksit (ZnO) nanotel dizilerinin üretilmesi için solüsyon tabanlı hidrotermal tekniği tercih edildi. Çinko oksit nanoteller, bir çinko oksit çekirdek katmanı üzerinde büyümeye başladığı için nanotel oluşumundan önce, alttaş olarak seçilmiş ve üzerinde çinko oksit nanotel sentezlenecek yüzeyler üzerine ince bir çinko oksit film kaplandı. ZnO nanoteller, soda-kireç cam, silikon, geçirgen-iletken-oksit grubundan indiyum kalay oksit (ITO) kaplı yüzeyler ve polietilen-tereftalat (PET) gibi esnek alttaşlar olmak üzere çeşitli alttaşlar üzerinde sentezlendi. Sonuçlar, ZnO nanotellerin, ~ 90 °C'lik solüsyon sıcaklığına ve sentez sırasında kullanılan kimyasallara dayanabilen herhangi bir esnek ya da esnek olmayan yüzey üzerinde başarıyla büyütülebileceğini gösterdi. Sonuçlar ayrıca, işlem süresinin ve ZnO nanotellerin oluşumu için gerekli olan ZnO çekirdek tabakasının seçilen alttaşlar üzerine hangi yöntemle kaplandığının, sentezlenen nanotellerin oryantasyonu, yoğunluğu, çapı ve homojenliği üzerinde güçlü bir etkisi olduğunu göstermiştir. Büyütme parametrelerinin hangi özelliğe etki ettiğini tespit etmek, istenilen özellikte filmlerin ya da nanoyapıların sentezine olanak sağlar. Büyütme parametreleri optimize edilen ZnO nanoteller, opto-elektronik aygıt uygulaması olarak çekirdek/kabuk diye tabir edilen n-ZnO NT/p-AgGaSe₂ (AGS) mimarisinde güneş hücresi olarak imal edildi. Bu güneş hücresi yapısını oluşturabilmek için, yapının çekirdek kısmını oluşturan ZnO nanoteller üzerine, soğurucu katman olarak p-AGS ince filmi saçırma yöntemi ile homojen bir şekilde kaplandı. Aynı zamanda yapının kabuk kısmını da oluşturacak olan bu kaplanan AGS ince filminin kalınlığı yaklaşık olarak ~ 700 nm olarak ölçüldü. Oluşturulan güneş hücresinin ışık altında performansının değerlendirilmesi için, standart koşullar altında (AM 1.5, 100 mW/cm²) bir güneş simülatörü kullanılarak ölçümler gerçekleştirildi ve % 1.74'lük bir verim elde edildi.

Çalışmanın ikinci kısmında, çinko oksitin özellikle elektriksel özelliklerinin geliştirilmesi için periyodik cetvelin 4. grubunda yer alan Sn ile katkılandırılmasından bahsedilmektedir. ZnO, geçirgen-iletken oksitlerin yerine geçebilecek alternatif malzeme olarak gösterilmektedir. Geçirgen-iletken oksitler opto-elektronik aygıtların en önemli temel bileşenlerinden biridir. Geçirgen-iletken oksitler adından da anlaşılacağı gibi geniş bir dalga boyu spektrumunda yüksek geçirgenliğe ve metaller seviyesinde iletkenliğe sahiptirler. Çinko oksitler ise görünür bölgede sahip olduğu yüksek optik geçirgenliğe rağmen oldukça yüksek dirence sahiptir. Yüksek direncin beraberinde getirdiği zayıf elektriksel iletkenlik aygıt içerisindeki ZnO kullanımını limitler ve performansın düşmesine neden olur. ZnO nanoteller ve kalkopirit AGS soğurucu katmanın bir araya getirilmesiyle oluşturulan güneş hücresinin daha yüksek

bir performans sergileyememesinin nedenlerinden biri çekirdek/kabuk mimarisinde oluşturulan güneş hücresinin çekirdek katmanını oluşturan ZnO malzemesinin sahip olduğu yüksek direnç olarak gösterilebilir. Bu nedenle yüksek dirence sahip olan ZnO bu çalışmada olduğu gibi, uygun elementlerle katkılandırılarak elektriksel özellikler gibi bazı özelliklerin gelişmesi sağlanabilir. Farklı Sn miktarları (% 0.5 – % 3.0) ile katkılandırılmış ZnO ince filmleri RF/DC magnetron saçtırma tekniği kullanılarak soda-kireç cam üzerine başarıyla kaplandı. Doping konsantrasyonunun ve tavlamanın, Sn katkılı ZnO ince filmlerin yapısal, optiksel, elektriksel ve morfolojik özellikleri üzerindeki etkileri ayrıntılı olarak incelendi. X-ışını kırınımı (XRD) ölçümleri, doping işlemi ile kristalliğin bozulduğunu ve aynı zamanda XRD spektrumundaki (002) ana pikinin sağa doğru yani daha büyük 2θ değerlerine doğru kaydığını gösterdi. Farklı sıcaklıklarda (150 °C, 250 °C ve 500 °C) tavlama işlemi uygulandıktan sonra ise, hem Sn ile katkılandırılmış hem de hiç katkılandırılmamış ZnO ince filmlerin kristal özelliklerinde ciddi bir gelişme gözlenmiştir. AFM analizi, doping işleminin yüzey morfolojisinde önemli bir değişikliğe neden olduğunu göstermektedir. Örneğin, % 3 Sn katkılandırılmış ZnO ince filmlerin yüzeyinde dut benzeri yapılar gözlemlenmiştir. Sn katkılandırılmış ZnO ince filmlerin optik özelliklerine bakıldığında, görünür bölgedeki ortalama geçirgenliğin, 500 °C 'de tavllanmış bütün filmler için ~ % 90 civarında olduğu görülmektedir. Geçirgenlik ve yansıma ölçümlerinden elde edilen değerlerle enerji bant aralıkları hesaplandı ve artan Sn konsantrasyonu ile enerji bant aralıklarının azalma eğilimi gösterdiği tespit edildi. Hiç katkılandırılmamış ZnO filmlerde hesaplanan 3.26 eV' luk enerji bant aralığı, % 3 Sn katkılandırılmış ZnO filmlerde 3.15 eV' a düşmekte, yani daha büyük dalga boylarına doğru kaymaktadır. Enerji bant aralığı değerlerindeki bu kayma, doping işlemiyle yasak bant aralığında oluşan derin seviyelerden dolayı bant aralığında oluşan daralmanın göstergesidir. Ayrıca, tavlama sıcaklığının artmasıyla birlikte enerji bant aralığı değerinde de bir artış olduğu ortaya çıktı. Oda sıcaklığında gerçekleştirilen ölçümlerde, % 1.5 oranında Sn katkılandırılmış ve 250 °C' de tavllanmış filmlerin en düşük direnç değeri olan $9.8 \times 10^{-3} \Omega \text{cm}$ direnç değerine sahip olduğu tespit edilmiştir.

Çalışmanın bir diğer bölümünde, yeni nesil güneş hücre yapısının çekirdek katmanını oluşturan ZnO nanoteller yerine Si nanoteller kullanılarak yapı oluşturulmaya çalışıldı. Dikey olarak hizalanmış n-tipi Si nanoteller basit ve düşük maliyetli bir üretim tekniği olan elektrotsuz oyma işlemi ile başarılı bir şekilde elde edildi. N-tipi Si plakadan elde edilen Si nanoteller, daha sonra çekirdek/kabuk güneş hücre yapısını oluşturabilmek için emici katman olarak seçilen p-tipi $\text{Cu}_2\text{ZnSnS}_4$ (CZTS) ince film ile kaplandı. Masrafları azaltmak adına, emici katman olarak kullanılacak CZTS, sol-jel yöntemiyle hazırlanıp, döner kaplama yöntemi ile kaplandı. Hazırlanan CZTS solüsyonu Si nanotellerin üzerine kaplanmadan önce soda-kireç cam alttaş üzerine kaplanarak optimize edildi. Tek fazlı kesterit CZTS yapısının oluşumu, hem X-ışını kırınımı hem de Raman analizleri ile kanıtlandı. XRD ve kompozisyon analiz (EDS) çalışmaları, stokiyometrik ve tek fazlı CZTS ince filmleri elde etmek için uygun tavlama sıcaklığının 350 °C olduğunu ortaya koydu. Büyütülen filmlerin enerji bant aralıklarının 1.55 eV olduğu tespit edildi. Oluşturulan n-Si NT/p-CZTS güneş hücre yapısı, AM 1.5G altında ~ 1.0 % güç dönüşüm verimliliği sergilemiştir. Bu çalışma ile birlikte, ilk kez bu aygıt konfigürasyonuna sahip, Si Nanotel tabanlı güneş hücresi rapor edilmiş oldu. Bu nedenle, çalışmamızın bu kombinasyondaki ve gelecek nesil güneş hücreleri ile ilgili gelecekteki çalışmalar için bir temel oluşturacağından eminiz.

Bu tez çalışmasının son bölümünde ise, üçüncü nesil güneş hücrelerinde soğurucu katman olarak görev yapan CZTS ince filmlerin tek fazlı ve yüksek kalitede

üretilebilmesi için yapılan çalışmalarına yer verilmiştir. CZTS soğurucu katmanlarının tek fazlı ve yüksek üretilebilmesi için yeni bir üretim yaklaşımı seçilmiştir. Bunun için ilk olarak, Bridgman tekniği ile Cu yönünden fakir, Zn yönünden zengin CZTS tek kristalleri başarıyla büyütüldü. Elde edilen kristalin yapısal ve foto-elektriksel özellikleri incelendi. CZTS ince filmlerin üretilmesi için, büyütülen CZTS kristali toz haline getirilerek elektron demeti tekniği kullanılarak tek adımda buharlaştırıldı. Kompozisyon analizi, kristal tozundan elde edilen CZTS ince filmlerin kompozisyonunun, kristal tozu için yapılan ölçümlere çok yakın olduğunu gösterdi. Detaylı XRD ve Raman analizleri, büyütülen filmlerin amorf yapı sergilediğini, 500 °C' de tavlanan filmlerin ise amorf yapıdan tek fazlı, (112) yönelimli kesterit polikristal formuna dönüştüğünü göstermiştir. Buna ek olarak, optik analizler bize yapının enerji bant aralığı değerini hesaplamamıza olanak sağladı. Buna göre, 500 °C' de tavlanan filmlerin enerji bant aralığı 1.50 eV olarak hesaplanmıştır. Yapılan foto-elektriksel ölçümler, güneş hücresi yapısında emici katman olarak kullanılacak olan CZTS ince filmlerin görünür ışığa karşı iyi bir duyarlılığa sahip olduğunu ortaya koydu. 500 °C' de tavllanmış CZTS ince filmler için oda sıcaklığında gerçekleştirilen Hall ölçümleri ile direnç, mobilite ve deşik taşıyıcı konsantrasyonu hesaplandı. Hesaplanan iletkenlik değeri yaklaşık $\sim 5.1 \times 10^{-4} (\Omega \cdot \text{cm})^{-1}$, mobilite $1.22 \text{ cm}^2/\text{V} \cdot \text{s}$ ve deşik konsantrasyonu da $2.6 \times 10^{15} \text{ cm}^{-3}$ olarak bulundu. Son olarak, sıcaklık bağımlı iletkenlik ölçümleri gerçekleştirildi. Bu ölçümler sonucunda da değerlik bandının üstünde 12 meV ve 60 meV değerlerinde yer alan ve bakır boşlukları ile ilişkili olduğu belirlenen iki alıcı seviyesi tespit edildi. Cu yönünden fakir CZTS ince film oluşumu, yapıdaki bu bakır boşluklarına dayandırılmaktadır. Dolayısıyla, iletkenlik ölçümleri sonucu tespit edilen bakır boşlukları, ölçüm yapılan filmlerin Cu yönünden fakir CZTS filmler olduğunu doğrular niteliktedir.



1. INTRODUCTION

Today, the world's energy consumption is known to be around 15 Terawatt (TW). Considering that the world's population has increased exponentially, it is estimated that our energy need will be doubled by 2050 [1]. At the present time, most of our energy needs are met by fossil fuels, which are known to be limited in supplies. As is known, the consumption of these fossil fuels is also the main cause of air pollution due to their byproduct exhaust gases, such as CO₂, NO₂, CO, and SO₂, during the burning process [2]. In today's world, therefore, the use of renewable clean energy as an attempt to replace the conventional fuels is of utmost importance. Solar energy is an inexhaustible source of energy. The energy absorbed from the sun in one hour, for instance, is capable of providing the global energy needs throughout the year. In addition to this, owing to providing a renewable and clean energy, it does not release any detrimental gas emissions, including sulfur and carbon monoxide, into the atmosphere, which make it a completely environmentally friendly source of energy.

It is known that Alexander Edmond Becquerel was the first researcher achieved the direct conversion of solar energy into the electrical energy via solar cells, based on the photovoltaic effect, in 1839 [3]. Since then, researchers in photovoltaic field have been making a massive effort to reduce production costs and to improve the power conversion efficiencies of solar cells. In general, solar cells are classified into three main generations. The so-called first generation solar cells are mainly based on single crystal and multi-crystalline silicon (Si) materials. The first generation solar cells are the most extensively employed ones, making up ~ 93 % of photovoltaic industry, for the generation of electricity from the sunlight not only due to the well-developed mature technology of the Si but also due to its abundance in the earth's crust, which offers the fabrication of high efficiency solar cells in a controlled manner. Second generation solar cells embody thin film-based solar cells, which allows the fabrication of solar cells by using less amount of material compared to that employed in the first generation ones. However, the power conversion efficiencies achieved with them are still well-below those obtained with the first generation solar cells. Consecutive thin

layers in the p-n junction form are used to construct thin film based solar cells. While on the upper side of the solar cell there is a layer with a large band gap energy to absorb the incident high-energy photons, at the bottom of the device, however, there is a layer with a small energy band gap that can absorb the photons with lower energies, not absorbed by the windows layer (upper component). Today, amorphous Si (a-Si), cadmium telluride (CdTe), and copper indium gallium selenide (CIGS) material based solar cells are located at the heart of second generation solar cells. Third generation solar cells were proposed to overcome the problems, such as high cost and low power conversion efficiency, associated with the first and second generation solar cells. The ultimate goal of the third generation of solar cells, therefore, was to realize high efficient solar cells in a cost effective manner. Dye-sensitized solar cells, organic and polymer solar cells, multi-junction solar cells, perovskite and kesterite solar cells, zero and one dimensional (nanowires (NWs), nanorods (NRs), nanotubes (NTs), and quantum dots (QDs)) based solar cells are among the third generation solar cells [3,4].

In particular, the use of nanostructures in solar cells known to be offering numerous advantages owing to their unique properties, such as large surface/interface area, light trapping effect, and high efficient carrier collection through single crystalline channels [5]. For the realization of high efficiency solar cells at lower cost, one of the most extensively preferred route is the incorporation of one-dimensional (1-D) nanostructures into the solar cell device structure so as to construct third-generation solar cells, which combine the benefits of first generation solar cells with the unique features of one-dimensional nanostructures. Up to date, different device architectures built by the 1-D nanostructures have been proposed, such as radial (core-shell), axial and embedded in thin film [5-7]. Among them, the device with the radial configuration has been particularly attracted a great deal of attention due to its effective charge collection as well as its light trapping function, which not only enables the fabrication of high performance solar cells but also the fabrication of them at quite lower cost compared to their planer counterparts. In general, the carbon nanotubes (NTs), Si NWs, ZnO NWs, and TiO₂ NRs, assigned as the core-component in the device structure, are among the most extensively employed one-dimensional materials for the fabrication of the core-shell structured p-n heterojunction solar cells due to their availability on the earth's crust and outstanding chemical/physical properties, such as the convenient optic band gap nature/values for the effective light absorption, non-

toxicity nature and the stability in harsh conditions [8]. The shell component in the core-shell architecture has a crucial role on the power conversion efficiency of the cell [9-11]. Well-known various absorber materials can be assigned as the shell components, such as CdTe, CdS, kesterites, and chalcopyrites [12,13], by taking their compatibility with the core material, such as the lattice matching and the band alignment in the case of p-n heterojunction construction. Among them, chalcopyrites are regarded as potential absorber shell-materials owing to their many advantages, including the adjustable optic band gap by tuning the content of the compound so that it can cover the most abundant part of solar spectrum and their relatively well-developed mature technology with respect to the other thin film materials [14]. Together with CdTe they have been known as the most extensively studied materials that can be employed for the fabrication of high performance thin film based solar cells (more than 20% power conversion efficiencies) [15]. Therefore, for a long time, they were considered to be the strongest alternatives to the crystalline silicon as the photovoltaic absorber layer, which is still dominating the today's photovoltaic market [16]. The chalcopyrite (copper iron disulphide, CuFeS_2) is a name given to the structure of copper iron disulphide (CuFeS_2) compound, which can be derived from the well-known zinc-blende structure [17]. These compounds are also called (I-III-VI₂) semiconductors as they are consisted of groups I (Ag, Cu), III (In, Al, Ga) and VI (S, Se, Te) elements. By using specific element combinations from the respective groups it is possible to construct nearly 35 compounds that can exhibit different optical (band gap) and electrical (resistivity and mobility) properties [18]. I-III-VI₂ semiconductors, in general, are called either Ag- and Cu- based chalcopyrites depending on the preferred element (Cu or Ag) for the group I element in the chemical formula. CuInSe_2 (CIS), a class of Cu-based chalcopyrites, has attracted a great deal of research interest for the thin film solar cell industry due to its remarkable properties, such as having an optimal band gap nature/value (direct band gap with ~ 1.04 eV) extremely high absorption coefficient (10^5 cm^{-1} , a large fraction of ($\sim 99\%$) the incident light absorbed in a depth of just one micrometer), and long-term stability [18-21]. In general, Ga atoms are intentionally replaced by In atoms ($\text{Cu}(\text{In}_x\text{Ga}_{1-x})\text{Se}_2$, CIGS, where $0 \leq x \leq 1$) with a specific proportion to shift its band gap from 1.04 eV to a value that can match the most intense part of the solar spectrum (1.45 eV). Owing the fact that it has a relatively mature technology, CIGS material can be easily obtained with various different fabrication routes, including solution and vacuum-based techniques

(thermal co-evaporation and sputtering) [22-25]. As the efficiency achieved with CIGS material has already surpassed a 20% value, it is regarded as a promising material that can compete with Si material in future [26]. Despite its many advantages, however, CIGS based solar cells faces several challenges. The presence of copper in the CIGS structure, for instance, may induce shorting problems in the device arising from the high diffusion capability of the copper. To address this intrinsic problem associated with this material, the replacement of Cu atoms by Ag atoms (AgGaSe_2 , AGS) has been proposed by many researchers. The proposed AGS compound, a class of Ag-based chalcopyrites, has a direct band gap (1.8 eV) and extremely high absorption coefficient, which is essential for a material to be employed as absorber layer in photovoltaic applications [27]. The conduction character of the AGS is tuned by generation of anion (Se) and cation (Ga, Ag) vacancies. In other words, the n-type and p-type conduction is achieved with anion-vacancies and cation-vacancies, respectively [28]. Besides its photovoltaic application, it is also known that a growing body of literature has studied the employment of AGS for a wide range of electronic and optoelectronic devices, such as frequency doubling (CO_2 laser output) and photodetectors [14,16,18-21,26,29].

As mentioned above, today's thin-film solar cells are mainly based on $\text{CuIn}_x\text{Ga}_{1-x}\text{Se}_2$ (CIGS) and CdTe materials, which are already at the commercialized stage. Despite their high mature technology and the providing high conversion efficiencies, the scarcity and toxic nature of their constituent elements (In, Ga and Cd) limit not only these material based solar cell technology but also their employment for the large-area photovoltaic systems [30,31]. Due to this fact, recently, a great effort has been devoted to find an absorber material that can overcome the afore-mentioned issues. To address all these issues this material must be based on abundantly available and environmentally benign elements. A material, consisted of nontoxic and the earth-abundant constituent elements (Cu, Zn, Sn and S), meet all these requirements is $\text{Cu}_2\text{ZnSnS}_4$ (CZTS). The CZTS material has a structure called kesterite, a name associated with the structure of $\text{Cu}_2(\text{ZnFe})\text{SnS}_4$ mineral kesterite [32]. It is also known as $\text{I}_2\text{-II-IV-VI}_4$ quaternary semiconductor due to the group numbers of the constituent elements. CZTS is a p-type material with a direct band gap energy of ~ 1.50 eV, which is exactly matching the optimal value required for absorbing the most intense part of the solar spectrum reaching on the surface of the earth [33]. Taken all these together,

it appears that the CZTS is an emerging solar cell absorber layer that can allow us to fabricate environment friendly and cost-effective solar cells with theoretical power efficiencies up to ~32.0 % [34].

1.1 Purpose of Thesis

The main aim of the present study is to fabricate cost-effective one-dimensional nanostructures (ZnO and Si NWs) based solar cells, known to be combining the advantages of first generation (e.g., high efficiency) and second generation (e.g., less material consumption and large scale production) solar cells with the unique features of one-dimensional nano-structures (light trapping and effective charge collection).

A prototype of one-dimensional nanostructures based solar cell was fabricated with ZnO NW arrays. For the synthesis of ZnO NWs, the hydrothermal technique was preferred due to its many advantages such as providing a contamination free growth route and allowing large-scale production of ZnO NW arrays in a cost effective manner. The required ZnO seed layers for the growth of ZnO NWs by hydrothermal route were deposited on transparent-conductive-oxide (ITO) pre-coated substrates by two different deposition techniques, sol-gel and RF-sputtering. While it was possible to synthesize homogeneously distributed and well-oriented ZnO NWs on sputter-deposited ZnO seed layers, it was not the case for those deposited by sol-gel technique. Therefore, the ZnO NWs grown on sputter-deposited seed layer were employed for the fabrication of core-shell solar cells. Following the optimization of ZnO NWs, they were employed for the construction of ITO/n-ZnO NWs/p-AgGaSe₂/In core-shell structured solar cell. As an absorber layer (shell) of this architecture, a member of Ag-based chalcopyrite compound (AgGaSe₂ (AGS)) was preferred, which is regarded as an alternative material to the most commonly employed material (CuInSe₂) in thin film based solar cells. In order to form AGS thin films, a route based on sequential deposition of Ag and GaSe layers by RF/DC sputtering was preferred. The n-ZnO NW/p-AgGaSe₂ core-shell structured solar cell with the chosen core and shell materials combination was fabricated for the first time under the present study.

In order to fabricate Si NWs for the realization of Si NWs based solar cells, electroless etching (EE) technique was preferred, which is known to be a quite simple and cost-effective route for controllable fabrication of large-scale one-dimensional Si nano/macro-structures. Si NWs were derived from a p-type Si-wafer as a result of a

series chemical reactions taking place when it is immersed into a reaction solution consisted of HF and AgNO_3 , heated at specific temperature for different time intervals. The effect of growth parameters, such as AgNO_3 concentration relative to DI-water and HF, etching time and reaction temperature on physical properties of derived NWs (radii, length, orientation and density) were studied in detail. Following the optimization cycles to understand the effect of growth parameters on the quality of the produced Si NWs, a set of them were decorated with absorber layers for the realization of Si NWs based core-shell structured solar cells. A prototype core-shell solar cell based on Si NWs was fabricated by coating Si NWs (20-80 nm in diameters and $\sim 3.5 \mu\text{m}$ in length) with sol-derived p-type CZTS absorber layer (~ 600 nm thick). CZTS thin films were obtained via sol-gel processes, which is known to be a promising route to solve many difficulties reported so far associated with obtaining high quality CZTS thin films. The preliminary results obtained with this prototype solar cell suggested that once some issues related to the core-material (e.g., geometry and aspect ratio of NWs) and shell material (e.g., quality of the absorber layer and contact issues) are well addressed, it would be possible to fabricate high efficiency Si/CZTS core-shell structured solar cells that can compete with their planer counterparts.

As a final part of the present study, a new fabrication route for the deposition of high quality CZTS thin films was employed, which is based on the electron-beam evaporation of a single crystalline powder extracted from Bridgman-grown CZTS ingots, allowed us to obtain high quality CZTS thin films by using only one-step deposition. Despite the fact that there have been many works reported on growing CZTS single crystals, very little attention has been given to using the powder extracted from them as an evaporation source to obtain single phase kesterite CZTS thin films. Moreover, even though a number of studies have been published on characterization of CZTS thin films, it is not the case for the CZTS single crystals, which is essential for revealing the fundamental properties of the compound and realization of high-efficiency solar cells. Therefore, the studies conducted under this thesis also fill this gap in the literature by investigating the electrical, structural and optical properties of Bridgman-grown CZTS single crystals.

The remainder of the thesis is organized as follows. Chapter 2 presents ZnO NWs synthesized using hydrothermal technique and then incorporate into AgGaSe_2 chalcopyrite thin film to fabricate a core-shell structured solar cell. It is the first study

reporting solar cell parameters of the device associated with these material combinations. In chapter 3, doping and annealing effects on structural, morphological, optical and electrical properties of undoped and Sn doped ZnO thin films, between 0.5 and 3.0 %, were investigated. ZnO has poor electrical conductivity and doping process enhances its electrical properties. A low cost core-shell like Si-nanowire (NW)/CZTS structured solar cell has been reported for the first time in the chapter 4. In the present study, the constructed solar cell structure couples the efficiency of the 1st generation with the benefits of 3rd generation solar cells. Chapter 5 focuses on the details of single crystal CZTS growth by Bridgman technique and thin film deposition by electron-beam and their electrical, structural and optical properties. Chapter 6 summarizes the results of this work and draws conclusions.

1.2 Literature Review

As noted in the previous part, a large part of our energy requirements are met via fossil fuels, not only a limited source of energy but also cause of a wide range of health and environmental impacts. Solar energy, therefore, has been seen as a solution to these source of energy related problems by many researchers for a long time. Accordingly, in recent years, there has been an increasing amount of literature on studies related to the generation of clean energy via photovoltaic effect. In this part of the chapter, thus, a brief summary of several previous works on solar cells fabricated with the above-mentioned core (ZnO and Si) and shell (CI(G)S, CZTS and AGS) materials will be presented.

The first Si p-n junction solar/photo cell was fabricated with a 6 % efficiency by Chapin et al. which was also the highest efficiency ever reported up to that time. Willeke et al. [35] reported a multicrystalline silicon based solar cell, the conversion efficiency, V_{oc} (open circuit voltage), J_{sc} (short current density) and FF (fill factor) of which were evaluated to be 20.3 % (highest ever reported), 664 mV, 37.7 mA/ cm² and 80.9 %, respectively [36]. For crystalline Si based solar cells, the highest efficiency (24.7 %) was achieved with a 98 μ m thick a-Si/c-Si/a-Si intrinsic thin-layer structured solar cell configuration [37]. In addition to Si material based ones, a number of thin film-based solar cells have been also reported so far aiming at developing low-cost and high-performance solar cells. In this regard, chalcopyrites and kesterites were the most extensively studied materials as the solar cell absorber layer. The first

chalcopyrite crystal heterojunction based solar cell with a 5 % efficiency was reported by Kasper et al. in 1974. In this device structure, CuInSe₂ and CdS were used as the absorber and windows layers, respectively [38]. In 1976, the first CuInSe₂/CdS thin film-based solar cells were fabricated by Kazmerski with efficiencies lying between 4% and 5 % [39]. In 1991, a thin film solar cells based on Ag-chalcopyrite, p-AgGaSe₂/n-CdS, was demonstrated with a 4.5 % power conversion efficiency, 55 % of FF, 0.51 of V_{oc} and 13.8 mA/ cm² of J_{sc} [40]. The addition of Ga to the structure of chalcopyrite, the use of CdS as a buffer layer instead of a window layer and the use of ZnO as a window layer were suggested to be enhancing the power conversion efficiency in another chalcopyrite thin film solar cell based study [31]. In that study, ZnO/CdS/CuInGaSe₂ structured thin film solar cell was constructed on Mo coated soda-lime glass substrate, which exhibited a 19.9 % power conversion efficiency [31]. In another major study , a 20.3 % efficiency was obtained via Cu(In,Ga)Se₂ absorber layer based thin film solar cell [23]. The other solar cell parameters of this device were calculated as V_{oc} of 0.74 V, J_{sc} of 35.4 mA/ cm² and FF of 77.5 %. When the first kesterite thin film-based solar cell with SLG/Mo/CZTS/CdS/AZO configuration was fabricated in 1996, the efficiency was only 0.66 % [41].

In that study, the CZTS absorber layer was fabricated by following two stage process. In other words, the CZTS absorber layer was first evaporated on Mo-coated SLG by electron-beam deposition, and then it was subjected to a post-production sulfurization process. The Voc, FF and Jsc parameters associated with this first CZTS based solar cell were also found to be 400 mV, 27.7 %, and 6.0 mA/cm² respectively. This efficiency value associated with CZTS absorber layer based solar cells was then increased to 8.4 % in 2011 [42], implying a remarkable progress with CZTS absorber layer. In 2018, a record efficiency, 11%, for CZTS based solar cell was declared by Yan et al. [43], which was achieved with heterojunction heat treatment that reduced non-radiative heterojunction recombination. For several years the use of nanostructures in solar cells has been attracted a great deal of attention for the realization of low-cost and high efficiency solar cells [44]. Therefore, in recent years, the research on the fabrication of one-dimensional nanostructures based solar cells has attracted much attention from research teams around the world. Kayes et al. [45] showed that a 14.5% efficiency (theoretically) could be achieved with Si NWs based core-shell solar cell. Despite of this high capacity of Si NWs based solar cells,

however, the efficiency associated with the first Si NW solar cell having core-shell architecture with thin amorphous n-Si layer on p-Si NWs was only $\sim 0.1\%$ [46]. The junction quality and the presence of some sort of impurities were identified to be the cause of the observed quite low solar cell power conversion efficiency. In 2008, Garnett and Yang demonstrated a Si NW core-shell solar cell based on two-step fabrication steps [6]. In that study, n-Si-NWS/p-Si-layer structured core-shell cell was fabricated through the coating of Si NW arrays with a p-type Si layer via chemical vapor deposition. The power conversion efficiency (PCE) for this cell was measured to be 0.46%. The presence of several interfacial recombinations and measured high series resistance were seen as the major factors responsible for the observed low PCE.

In addition to Si NWs, several attempts have been also made to fabricate ZnO NWs based solar cells. For instance, P. D. Yang et al. demonstrated an all-oxide solar cell, in which n-type ZnO NW array covered by a p-type Cu_2O nanoparticles, aiming at the realization of environmentally benign stable solar cells [47]. Results showed that the efficiency that can be achieved with this device configuration were mainly dependent on the morphology, the thickness and the phase of Cu_2O nanoparticles. In that study, it was also revealed that an intermediate 10 nm thick TiO_2 layer inserted between the electrode and Cu_2O could significantly improve the performance of the cell, 50 times higher, compared to that constructed without this layer. In a recent study, a prototype FTO/ZnO-NWs/CdTe /Ni/Au core-shell solar cell was fabricated by decoration of ZnO NWs, synthesized by chemical bath deposition, with a RF-sputtered and 10 nm thick CdTe thin layer [48]. The PCE and J_{sc} of the cell with this material combination was calculated to be 3.41% and 13.3 mA cm^{-2} , respectively. Following the introduction of a thin layer of CdSe to the previous device configuration (i.e., with FTO/ZnO-NWs/CdSe(10 nm)/CdTe/Ni/Au), however, a 5.58% enhancement in power conversion efficiency was recorded. Karaağac et al. demonstrated that ZnO NW based solar cells were fabricated by deposition of an 800 nm thick $\text{AgGa}_{0.5}\text{In}_{0.5}\text{Se}_2$ thin film by an electron beam technique on glass/ITO/ZnO NWs substrates and for the ZnO NWs based solar cell, 0.37% efficiency was obtained under AM 1.5G illumination [49].



2. SYNTHESIS OF ZnO NANOWIRES AND THEIR PHOTOVOLTAIC APPLICATION: ZnO NANOWIRES/AgGaSe₂ THIN FILM CORE-SHELL SOLAR CELL¹

2.1 Introduction

In recent years, there has been an increasing amount of literature on both one-dimensional nanostructures synthesis and employment of a wide range of thin film semiconductor materials for the realization of high-efficiency, low cost solar cells. However, there are a quite few research studies on combining these efforts. In this regard, employing one-dimensional (1D) nanostructures such as nanowires (NWs), nanorods (NRs) and nanotubes (NTs) to construct three-dimensional (3D) device architectures is a very promising approach for the realization of next-generation high-efficiency for solar cells at lower cost [5,7].

In the past two decades, to improve the performance of solar cells 3D photovoltaic device architectures including axial, radial (core-shell) and nanostructures embedded in thin film models have been studied extensively with different material combinations [5]. In particular, core-shell architecture offers significant advantages over its planer counterparts due to its unique properties, such as light trapping, efficient charge collection, quantum confinement and decoupling the photon absorption and carrier collection in an effective way. Currently, silicon (Si), titanium-dioxide (TiO₂) and zinc-oxide (ZnO) are the most commonly employed semiconductor materials for the construction of core-shell solar cells as the core-component. There are many potential reasons to choose these materials such as their abundance in the earth crust, non-toxic nature, convenient band-gap nature/energy value, stability and outstanding chemical/physical and optical properties [8]. In core-shell structure, the shell component plays a crucial role in determining the performance of the designed device [9-11]. As a shell component, chalcopyrite semiconductors (CuInSe₂, Cu(In, Ga)(S,

¹ This chapter has been published in Journal of Nanomaterials. Peksu, E., Karaağaç, H., (2015), Synthesis of ZnO Nanowires and Their Photovoltaic Application: ZnO Nanowires/AgGaSe₂ Thin Film Core-Shell Solar Cell, Journal of Nanomaterials, 2015, 1-10, doi: 10.1155/2015/516012.

Se)₂ and Ag(In, Ga)(S, Se)₂) are regarded as promising candidates due to their convenient band-gap nature and energy value, which exactly matches the most abundant part of solar spectrum reaching on the surface of the earth [14,31]. Therefore, the proper band-gap nature/energy value of these materials suggests that more than 90 % of the incident light can be absorbed in a few micrometer of the material [50]. Chalcopyrites along with CdTe are regarded as the most promising semiconductors alternatives to the Si and are at the heart of today's thin film based solar cells [16].

In the present investigation, we have constructed 3D core-shell solar cell by employing a sputtered AgGaSe₂ (AGS) thin film as shell component due to its high absorption coefficient ($\sim 10^5 \text{ cm}^{-1}$) and convenient bandgap nature/energy (direct band gap with $\sim 1.8 \text{ eV}$). It is a well-known fact that AGS semiconductors can also be used for many other applications including frequency doubling (CO₂ laser output) and photodetectors [27,29,51-53]. For the core-component of the fabricated solar cell, ZnO material was preferred, a semiconductor with a large band gap (3.37 eV) and exciton binding energy (60 meV) at room temperature, due to its many outstanding properties such as the piezoelectricity, near band emission, and transparent conductivity. ZnO has been widely used for many opto-electronic devices so far, including solar cells, light-emitting diodes (LEDs) and gas sensing [8,49,54,55].

A wide range of fabrication techniques have been reported in literature so far for the synthesis of 1D nanostructures, which can be classified into different routes: (i) vapor and (ii) solution based techniques [56-58]. Of several solution based approaches, hydrothermal technique is of a special interest due to its many advantages such as low growth temperature, ease of controllable doping, reliable and contamination free growth, tunable physical parameters, allowing mass production and no requirement of vacuum and expensive equipments [59]. Based on these considerations, therefore, in the present study, ZnO NWs were synthesized using hydrothermal technique. The object of this study is to synthesize ZnO nanowires (NWs) by hydrothermal technique and then incorporate into AgGaSe₂ chalcopyrite thin film to fabricate a core-shell structured solar cell. As n-ZnO NW/p-AgGaSe₂ core-shell type hetero-junctions have not been studied so far, it is going to be the first study reporting solar cell parameters of the device associated with these material combinations.

2.2 Experimental

ZnO NWs were grown onto different substrates including soda-lime glass (SLG) precoated with indium tin oxide (ITO), SLG, PET (Polyethylene terephthalate), and n-Si wafer substrates ((100) orientation and 1-10 ($\Omega\cdot\text{cm}$) resistivity) using hydrothermal growth technique. For the synthesis of ZnO NWs, ~30 nm thick ZnO seed layers were deposited onto the aforementioned substrates by using both sputtering and sol-gel techniques. Sputter-deposited seed layers were deposited using a radiofrequency (RF) magnetron system, the employed power of which was 150 W under 5×10^{-3} Torr in an Ar atmosphere. For the fabrication of ZnO seed layers by sol-gel route, a ZnO precursor solution was prepared by dissolving zinc acetate dihydrate ($\text{ZnAc}:\text{Zn}(\text{COOCH}_3)_2 \cdot 2\text{H}_2\text{O}$) in 2-propanol and diethanolamine (DEA, $\text{C}_4\text{H}_{11}\text{NO}_2$), assigned as solute, solvent and chelating agent, respectively. The molar ratio of DEA/ZnAc and $\text{H}_2\text{O}/\text{ZnAc}$ were chosen as 1 and 1/2, respectively to prepare a solution with 0.4 M concentration, details of which has been given elsewhere [54,60]. The precursor solution was stirred at 70 °C for 1 h to get a clear and homogenous solution. After that, ZnO seed layers were deposited on precleaned SLG substrates by spin coating at one step with spinning speed of 5000 revolutions per minute (rpm) for 1 min. The spin coating process was based on a single stage coating process to obtain ~30 nm thick ZnO seed layer. Spin-coated seed layers were first pre-heated at 300 °C on hot plate for 10 min and then annealed at 550 °C for 1 h in air ambient for the complete crystallization of seed layer and evaporation of the remained organics in the thin film structure. Following the deposition of the ZnO seed layer, the substrates were subjected to a solution based on equimolar 25 mM $(\text{Zn}(\text{NO}_3)_2) \cdot 6\text{H}_2\text{O}$ (Zinc nitrate hexahydrate, Sigma Aldrich) and HMTA (Hexamethylenetetramine, Sigma Aldrich) as precursors in deionized (DI) water (with 18 $\text{M}\Omega\cdot\text{cm}$ resistivity). During the ZnO nanowire growth cycle the solution temperature and the growth time were set as 90°C and 1.5-3 hours, respectively [49].

For the fabrication of n-ZnO NWs/p-AgGaSe₂ core-shell solar cell, ZnO NWs grown on SLG substrate (pre-coated with ITO) were decorated with AgGaSe₂ (AGS) thin films. For the deposition of AGS thin films, a three-source sputtering system (Vaksis) was preferred. 4-inch Ag and GaSe sputtering targets (at a tilt angle of 30°) were used as sources for the sequential deposition of Ag and GaSe thin film layers. For the plasma generation in the chamber, argon gas with 99.99% purity was employed, which was

set to 6 sccm during the film deposition. The distance between targets and the substrate during the deposition cycle was around 25 cm. To enhance the uniformity of AGS thin films, the substrate was rotated on a heated plate during deposition process. As it is semi-insulating material, for the deposition of GaSe thin film RF sputtering was used with power of 75 W under 5×10^{-3} Torr Ar gas pressure. The deposition of Ag thin film layers was carried out by DC magnetron sputtering with a 20 W power in a 5×10^{-3} Torr Ar gas pressure atmosphere. The deposition rates for the sequentially deposited Ag and GaSe layers were chosen as 1 Å/s and 2 Å/s, respectively. Prior to decoration of ZnO NWs with AGS, to optimize the quality of AGS thin films, single layers of Ag and GaSe were sequentially deposited on SLG substrates to form GaSe/Ag/GaSe/Ag/GaSe/Ag/GaSe/Ag/GaSe multilayers. During the optimization cycle the substrate temperature kept constant at 150 °C and the thickness of Ag and GaSe layers was set to 20 nm and 125 nm, respectively. Both deposition rate and thickness of each layer were simultaneously monitored with an integrated oscillatory quartz (Inficon XTM/2). Following the sequential deposition of Ag and GaSe layers, they were annealed in vacuum at temperature of 275 °C for 30 min to trigger the interdiffusion of multilayers. In addition, to investigate the effect of annealing on physical properties of deposited AgGaSe₂ thin films the post-annealing in the temperature range of 300-550 °C was employed, which was carried out on a hot plate under N₂ gas flow for 30 min. After optimization stages of thin film, a ~700 nm thick AGS layer was deposited onto the synthesized ZnO NWs for the realization of SLG/ITO/n-ZnO NWs/p-AgGaSe₂ core-shell solar cell. For the top and bottom contacts of the device, thermally evaporated indium dot contacts (using a dot-patterned copper mask) and SLG pre-coated with ITO were employed, respectively.

To determine the structural, electrical and optical properties of deposited AGS thin films several characterization techniques have been applied. The crystal structure and orientation, existing material phases and the size of the grains were determined by means of X-ray diffraction (XRD) using a Scintag XDS2000 powder X-ray diffractometer with CuK_α radiation source. The optical properties were investigated by performing transmission measurements in the wavelength range of 300-1100 nm using an Ocean Optics UV-VIS spectrometer. Electrical measurements were carried out using a four-point van der Pauw method. Ohmic contacts on chalcopyrite thin films (AGS) were achieved by thermal evaporation of high pure In using a convenient

copper mask. For the electrical characterization of AGS thin films, following the confirmation of ohmic nature of contacts, temperature dependent conductivity and photoconductivity measurements were carried out in temperature range of 100-430 K in a Janis cryostat equipped with a Keithley 220 current source, 619 electrometer, 2400 digital sourcemeter, and a Lake shore 331 temperature controller. The surface morphology, composition and thickness of deposited thin films as well as the morphology of ZnO NWs were determined by a Hitachi S-4100 FE scanning electron microscopy (SEM) equipped with EDXA. The current (I)-voltage (V) characteristic of fabricated solar cell was measured at room temperature (300 K) using a LabVIEW controlled Keithley 2400 source-meter. Finally, testing of fabricated solar cells was performed in a Oriel 1000 W solar cell simulator set up (under AM 1.5 conditions), which was controlled with Newport I-V test software.

2.3 Results and Discussion

Figure 2.1 shows typical scanning electron microscope (SEM) image of ZnO nanowires (NWs) grown on different substrates including silicon (Si), soda lime glass (SLG), indium tin oxide (ITO) pre-coated SLG, and polyethylene terephthalate (PET) by using hydrothermal technique. ZnO NWs were grown on the aforementioned substrates pre-coated with ~30 nm thick ZnO seed layer deposited by RF sputtering. Growth time and temperature were chosen as 3h and 90 °C, respectively.

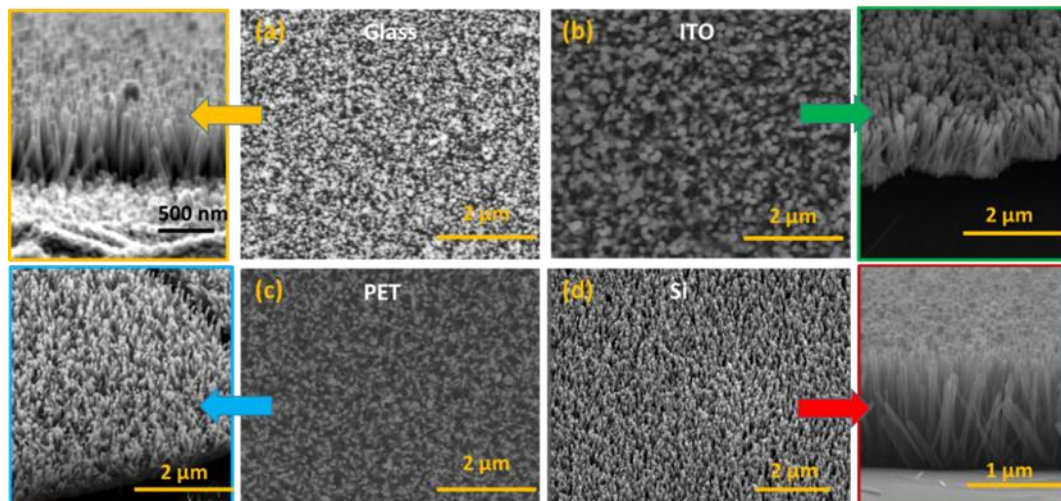


Figure 2.1 : Top- and tilted-view SEM images of ZnO nanowires grown on (a) soda lime glass, (b) indium tin oxide, (c) polyethylene terephthalate (PET), and Silicon (Si) by using hydrothermal technique.

From the images presented in Figure 2.1, it is apparent that ZnO NWs are 1.2-1.3 μm long and 65-95 nm in diameter, which are nearly uniformly distributed over the surface of the substrates. In addition, it can be seen from the images that highly dense and vertically well-oriented ZnO NWs can be grown on any substrates as long as they can withstand growth temperature ($\sim 90^\circ\text{C}$) and chemical used in the precursor solution that required for growth of NWs by hydrothermal approach. In particular, the growth of ZnO NWs on a flexible substrate such as PET is very important since it allows the realization of flexible opto-electronic devices including UV-photodetectors, solar cells and light emitting diodes (LEDs).

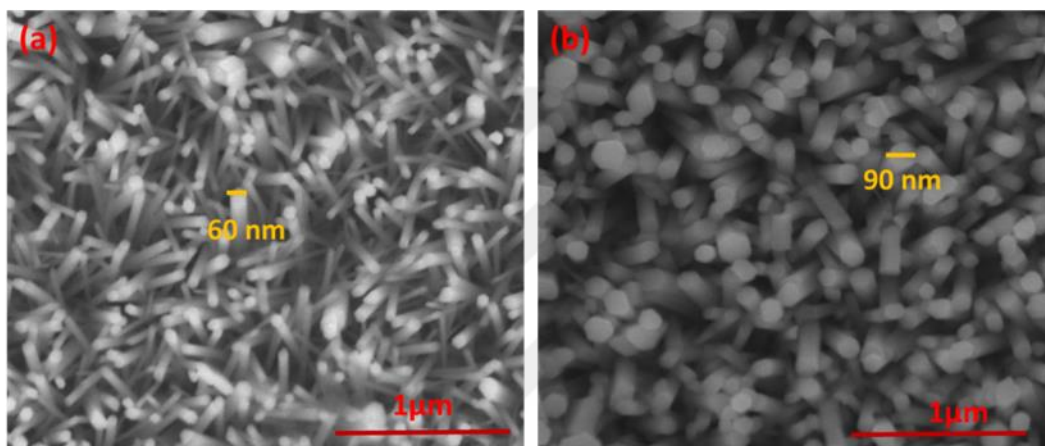


Figure 2.2 : Top-view SEM images of ZnO nanowires grown on soda lime glass substrates for growth times of (a) 1.5 h and (b) 3 h.

In order to reveal the effect of growth time on diameter of ZnO NWs, grown on sputter deposited ZnO seed layer with thickness of ~ 30 nm onto SLG substrates, growth was carried out for 1.5 h and 3 h time duration by keeping the other growth parameters constant. As can be seen from SEM images illustrated in Figure 2.2, there is a significant difference between the diameters of grown ZnO NWs for these growth time durations, which are ~ 60 nm and ~ 90 nm for 1.5 h and 3 h, respectively. The present findings on the relation between growth time and nanowire diameter seem to be consisted with other findings of a great deal of the previous works focused on this correlation. The observed increase in diameter with increasing growth time is generally attributed to the coalescence of poor-oriented longer NWs. It is possible, therefore, that by using the revealed correlation between these two parameters, the aspect ratio of ZnO NWs can be adjusted for specific device applications, such as light scattering, guiding and trapping to enhance the absorption of incident light for photovoltaic applications.

In addition to the effect of growth time, the effect of seed layer deposition route on the morphology of ZnO NWs has been determined by comparing the quality of NWs grown on ZnO seed layers deposited by sol-gel and sputtering technique, SEM images of which are presented in Figure 2.3. During the NW growth stage all the growth parameters including temperature, precursor concentration, and orientation of substrate with respect to the wall of beaker and growth time except seed layer deposition approach were kept constant to reveal the effect of this parameter. As can be seen in Figure 2.3, there is a significant difference between the quality of NWs grown on seed layers deposited by different routes in terms of density, orientation and uniformity of synthesized NWs. The obtained results suggest that seed layer deposition route has a strong impact on NW quality and the best quality comes with NWs grown on sputter-deposited ZnO seed layer.

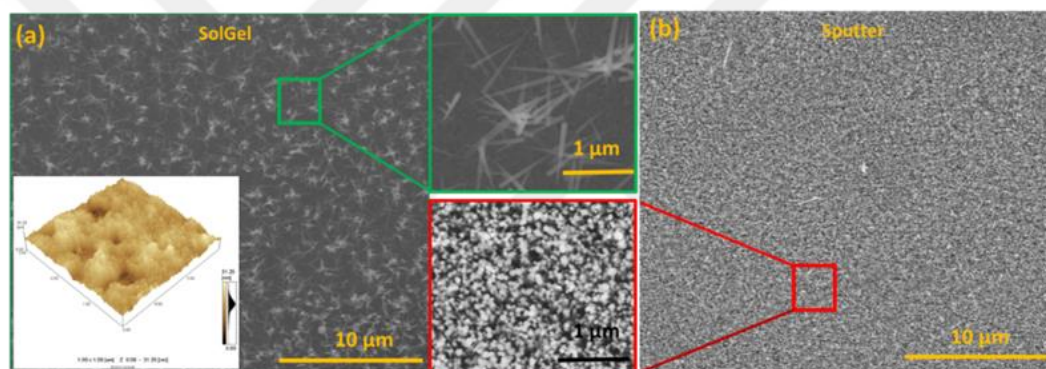


Figure 2.3 : Top-view SEM images of ZnO nanowires synthesized on ZnO seed layers (on soda lime glass substrates (SLG)) deposited by (a) sol-gel and (b) sputtering technique. Inset figure shown in part (a) presents the AFM image recorded for ZnO seed layer on SLG substrate deposited by sol-gel route.

In other words, it was observed that well-oriented, homogeneously distributed dense arrays of ZnO NWs were synthesized on sputtered deposited ZnO seed layer, which was not the case for the NWs grown on sol-gel deposited one. To understand the origin of this difference, the atomic force microscope (AFM) measurement was conducted for the ZnO seed layer deposited by sol-gel, image of which is given as inset in Figure 2.3(a). It is clear from this image that the surface of the deposited seed layer is not uniform and consisted of well-like features that randomly distributed over the surface. As expected, it is not possible to deposit very uniform continuous ZnO thin film layers by sol-gel as opposed to sputtered layers, which promotes the formation of these features.

Among the plausible explanation for the observed low quality of ZnO NWs grown on sol-gel deposited seed layer, in terms of orientation, density and uniformity, we can suggest that it is these well-like features which triggers the formation of poor-oriented low quality NWs. In other words, these randomly distributed features may function as seeding centers that promote the formation of ZnO NW nucleations, from which NWs derive. It is, therefore, expected that the shape and density of these features will be the two important factors that will assign the quality of synthesized ZnO NWs.

To investigate the stoichiometry of deposited AgGaSe₂ thin films, energy dispersive X-ray analysis (EDXA) measurements were performed at 20 keV for as-grown sample. The EDXA pattern and atomic percentage of constituent elements are given in Figure 2.4. As expected, all constitute elements are appeared in the spectrum at specific energy values (Figure 2.4 (b)). Based on the measured values of atomic percentage of elements, it is possible to claim that a nearly stoichiometric AgGaSe₂ thin film (inside the interval of experimental error limit (1-2%)) is successfully obtained.

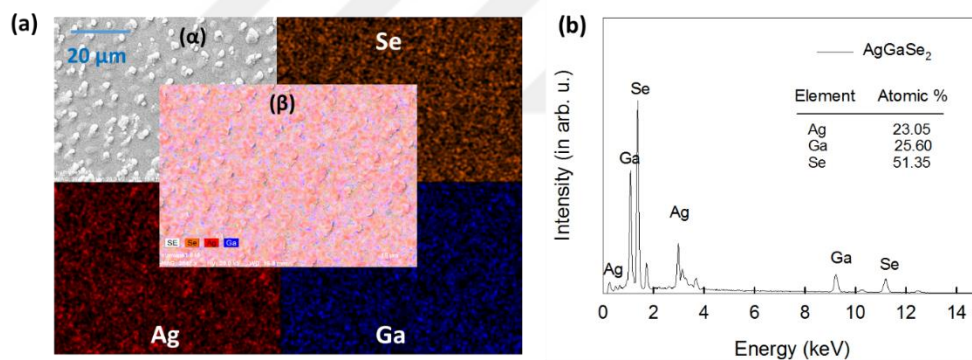


Figure 2.4 : (a) SEM images showing the elemental mapping for the constituent element of as-grown AgGaSe₂ thin film: Uncolored image at left top shows the bare surface of thin film before the elemental mapping; the one at the center shows combined elemental mapping. (b) EDXA pattern and calculated atomic percentage of constitute elements in as-grown AgGaSe₂ thin film deposited onto soda-lime glass substrate.

Beside the EDXA pattern, as shown in Figure 2.4 (a), we have obtained elemental mapping for constitute elements for as-grown thin film to determine the distribution of elements in the sequential layers of deposited AgGaSe₂ thin film. It is clear from the map that Se and Ag elements cover the majority part of surface, while Ga is just beneath them, which implies the existence of uncompleted reaction for the

construction of an ordered AgGaSe₂ structure, possibly due to insufficient heat energy supplied during deposition process (150 °C).

Figure 2.5 shows the X-ray diffraction pattern recorded for as-grown and AgGaSe₂ thin film annealed in the temperature range of 300-550 °C. As can be seen from the figure, the as-grown film is polycrystalline and consisted of single phase AgGaSe₂ having chalcopyrite structure with lattice parameters of a=b=5.993 Å and c=10.884 Å [61]. Following the post-annealing between 300 and 550 °C, it was observed that the intensity of all peaks appeared in XRD pattern increases gradually with increase in annealing temperature, which closely related with the improvement in crystallinity. The improvement of crystallinity can be attributed to the elimination of imperfections in structure following the post-annealing process at high temperatures. In our previous studies, although several attempts have been made to deposit single phase AGS at low substrate or annealing temperatures, we couldn't achieve it due to either appearance of secondary phases such as Ag or the requirement of deposition of this material on substrates that can withstand high annealing temperature (>550 °C). But, here with this study we report the achievement of producing a single phase AGS at quite low substrate temperature (150 °C). Obtaining a thin film in a single phase without any secondary phases is essential for a precise control on opto-electronic devices such as solar cells.

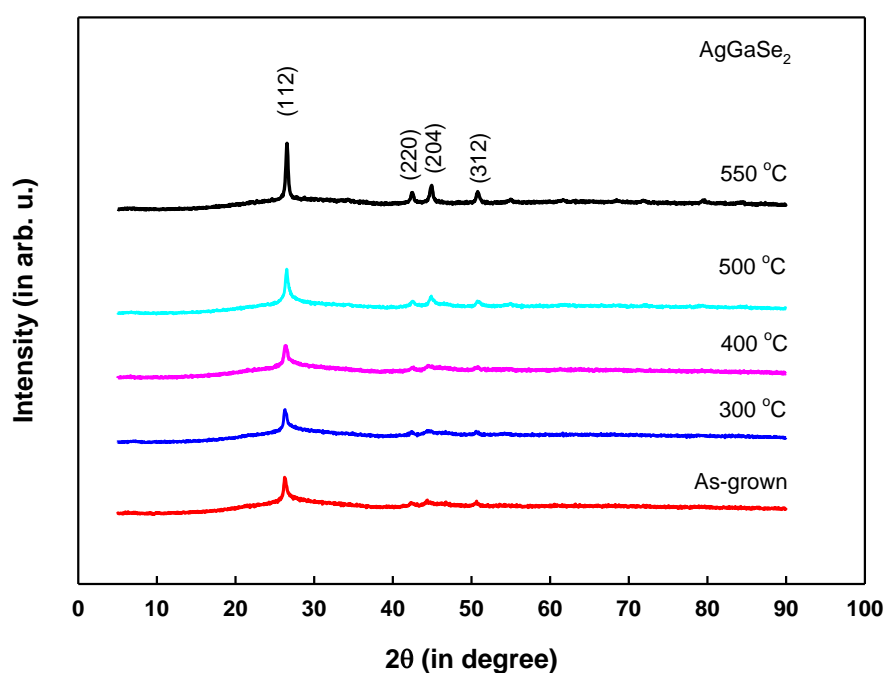


Figure 2.5 : X-ray diffraction pattern obtained for as-grown and AgGaSe₂ thin film annealed between 300 and 550 °C.

The optical transmittance of deposited and AgGaSe₂ thin films has been determined in the wavelength range of 325-1100 nm. The obtained spectra for as-grown and film annealed between 400 and 550 °C are presented in Figure 2.6 (a). It can be seen from the transmission spectra that the post annealing process has a remarkable effect on transmittance of AGS thin films.

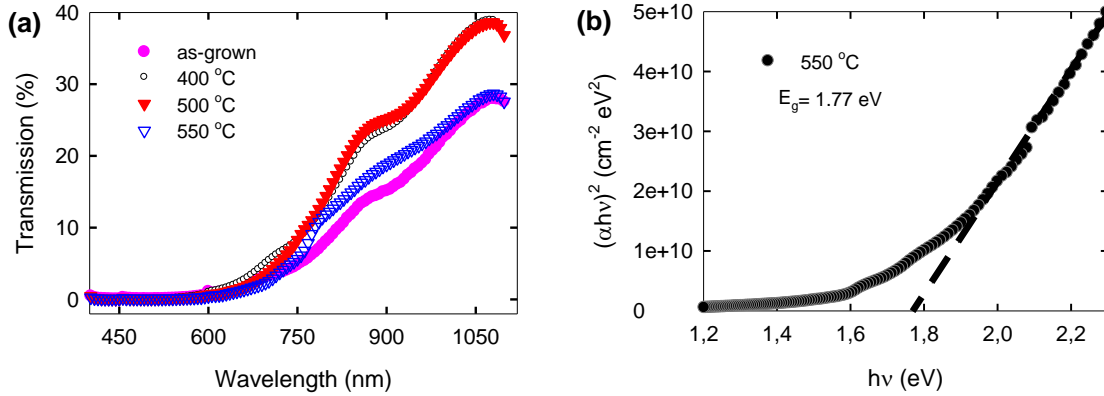


Figure 2.6 : (a) Transmittance spectra obtained for as-grown and AgGaSe₂ thin film annealed at different temperatures (400, 500 and 550 °C) and (b) absorption coefficient (α) and photon energy ($h\nu$) relation for AGS thin film annealed at 550 °C.

That is, it was observed that there is a systematic increase in transparency with increasing annealing temperature, except for the annealing temperature of 550 °C. The observed increase in transparency may be due to the structural modifications deduced from XRD study in which an improvement in crystallinity was deduced after post annealing process. In an other words, post annealing process may ends up with reducing defects in polycrystalline structure by which a better crystallinity and homogeneity provided. This may subsequently result in less scattering of light and enhancement in transparency. The optic band gap (E_g) and absorption coefficient (α) of the deposited films were calculated through transmission spectra presented in Figure 2.6 (a). The relation between absorption coefficient and photon energy ($h\nu$) for the film annealed at 550 °C is shown in Figure 2.6 (b). From this relation, the optic band gap can be determined through the extrapolation its linear portion of plot to zero absorption coefficient. The band gap was found to be around 1.77 eV, which is in a close agreement with reported values in literature [29].

The temperature dependent conductivity measurements were carried out in the temperature range of 100-430 K for as-grown and films annealed between 400 and 550

°C. The variation of conductivity as a function of temperature is shown in Figure 2.7 (a).

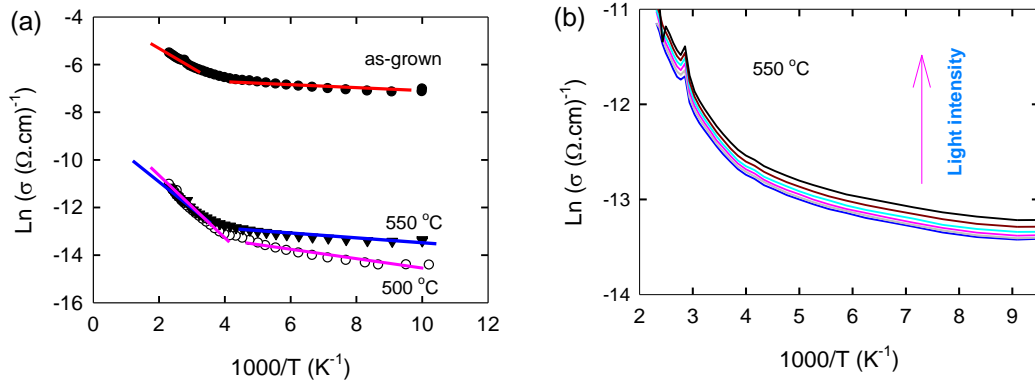


Figure 2.7 : (a) The variation of conductivity as a function of temperature for as-grown and AgGaSe₂ thin film annealed at 500 and 550 °C. (b) Temperature dependent conductivity of AgGaSe₂ thin film annealed at 550 °C under different illumination intensities (between 20 and 115 mW/cm²).

It can be seen from the Figure 2.7 (a) that the conductivity increases as the temperature increases. As mentioned before, this behavior verifies that AGS thin films are acting as semiconductor material. The type of conduction was determined by hot probe method, which revealed that it was a p-type character. Obtaining a p-type AGS thin film was an essential requirement for this study to construct a p-n heterojunction with n-type ZnO nanowires. It can also be seen from Figure 2.7 (a) that the conductivity decreases following the post annealing process. The room temperature resistivity values were found to be around 5.3×10^2 , 5.5×10^5 and 2.6×10^5 ($\Omega \cdot \text{cm}$) for as-grown and sample annealed at 500 and 550 °C, respectively. The increase in resistivity of the annealed film with respect to the as-grown one may stem from the unreacted sequentially deposited single layers of Ag and GaSe at low substrate temperature (150 °C). Therefore, in as-grown polycrystalline structure there may be unreacted Ag agglomerations that have possibility to act as conductive path for the transport of free charge carriers. However, it is not the case for the annealed samples due to the existence of ordered structure of AgGaSe₂, which is a semi-insulating material, following the post annealing process. This result is in line with data extracted from XRD study by which the improvement of crystallinity of AgGaSe₂ phase has been deduced.

In addition, as can be seen from Figure 7(a), the observed behavior of conductivity follows the Arrhenius relation [62];

$$\sigma = \sigma_o \exp \left[-\frac{E_a}{kT} \right] \quad (2.1)$$

where σ_o , E_a , and k are pre-exponential factor, activation energy and Boltzmann's constant, respectively. Here, E_a is the activation energy corresponding to a specific current mechanism activated at a specific temperature interval. The $\text{Ln}\sigma$ vs $1000/T$ plot reveals two distinct linear regions for all samples, implying existence of two different local states with different activation energies, which is activated at low and high temperature intervals. Since the type of conduction was found as p-type, it can thus be suggested that these states are associated with acceptor levels, formation of which are triggered as a consequence of a small deviation from stoichiometry deduced from the EDXA study. It is known that this deviation may results in the generation of group-VI (Se) vacancies that act as acceptors in chalcopyrite structures. In addition to dark conductivities, the temperature dependent conductivities under different illumination intensities (provided by a halogen lamp (from 20 to 115 mW/cm^2)) have also been measured in the temperature range of 100-430K. The variation for the film annealed at 550 °C is shown in Figure 2.7 (b). It can be seen from this variation that the conductivity increases linearly almost at the same increments with increasing light intensity from 20 to 115 mW/cm^2 , which verifies the existence of photo-response for this material under light and it can be employed as an absorber layer in the photovoltaic device structure. Figure 2.8 (a) Shows SEM image of the structure of a fully fabricated n-ZnO-NWs/p-AgGaSe₂ core-shell solar cell. It is apparent from the image that ZnO NWs are decorated with sputtered AgGaSe₂ layer for the realization of p-n heterojunction solar cell. It is also clear that the AGS layer at the top part of ZnO NWs is thicker than that at the bottom part, which can be attributed to the limitation of our technique, sputtering, for the decoration of AGS layer [63]. In other words, ZnO NWs are not conformally coated with AGS layer and are thicker than desired. Therefore, the ZnO NWs in the completed solar cell structure are connected by the p-AGS canopy layer (a continuous film), resulting a planer surface of a hybrid thin film-nanowire architected device. In this type device architecture, although it is reasonable to expect an enhanced carrier collection efficiency, it is not the case for optical properties, which are almost similar to thin film or wafer-based solar cell architecture owing to its planer top surface [64].

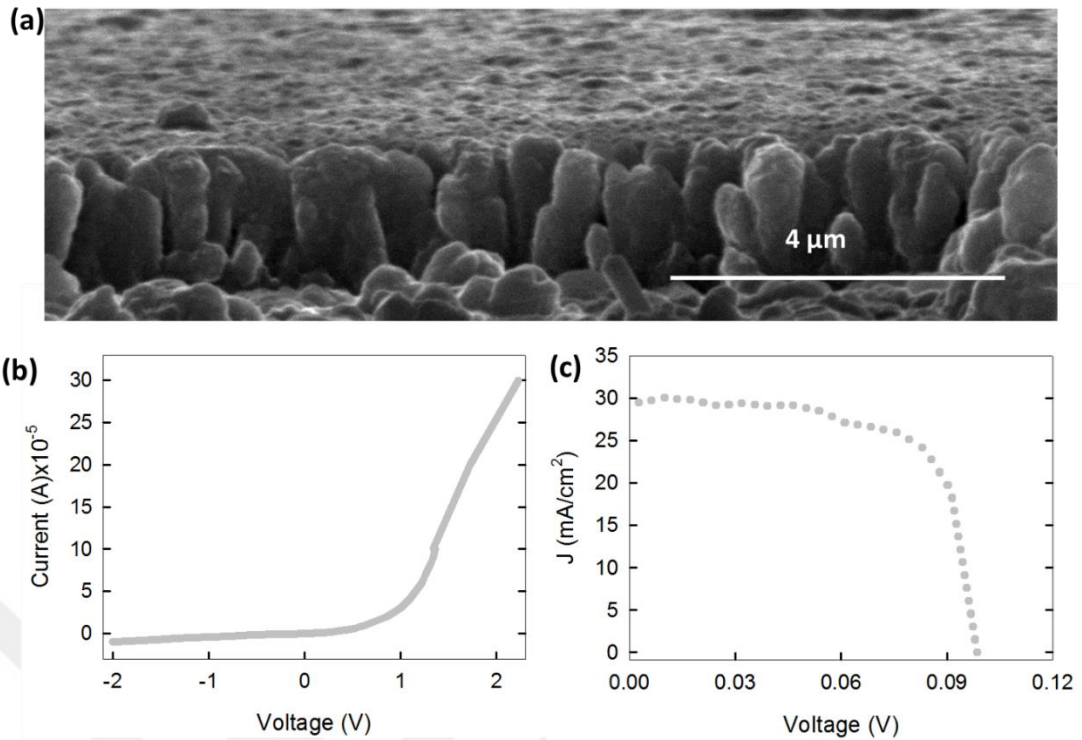


Figure 2.8 : (a) Cross-sectional view SEM image of the structure of a fully fabricated n-ZnO-NWs/p-AgGaSe₂ core-shell solar cell. (b) Current (I)-voltage (V) characteristic of the fabricated solar cell recorded under dark condition and (c) under 100 mW/cm² of simulated solar illumination.

As the constructed device is the first prototype, there are many issues we must address. The surface morphology is among them. Our ongoing work has focused on adjusting the shell layer's thickness for the realization of conformally coated ZnO NWs, which are desired for the more incident light absorption through light trapping and scattering. Figure 2.8 (b) presents the current (I)-voltage (V) characteristic of the fabricated solar cell obtained under dark condition. As can be seen from the I-V curve, there is a good rectification (Forward-current/Reverse-current: 8 at 1V), which verifies the construction of p-n heterojunction between ZnO NWs as core component and AGS as shell component. In order to determine the performance of constructed prototype core-shell solar cell, the I-V measurement was also carried out under light illumination (AM 1.5, 100 mW/cm²). The I-V characteristic of n-ZnO-NWs/p-AgGaSe₂ solar cell with a contact area of 0.06 cm² measured with a solar simulator under standard AM 1.5 condition is shown in Figure 2.8 (c). Solar parameters, such as open circuit voltage (V_{oc}), short circuit current density (J_{sc}), fill factor (FF) and power conversion efficiency (η) were calculated from the I-V curve obtained under light illumination with respective 0.098 V, 29.40 mA/cm², 60.25 % and 1.74 % values. There are only a few studies in literature that deal with core-shell solar cells based on integration of

NWs into chalcopyrite thin films. For instance, energy efficiencies for core-shell solar cells consisted of ZnO/CdS/CIGS and ZnO/(Zn, Mg)O/CIGS were found to be as 2.18% and 4.1%, respectively [65]. However, in the present investigation, as it is the first study based on reporting the performance of core-shell n-ZnO-NWs/p-AgGaSe₂ solar cell, it is not possible to compare the results with that reported in literature. In addition, when compared with its AgGaSe₂ based planer counterparts (with power conversion efficiencies of 4.5-7.8 %), there is no doubt that it has a lower power conversion efficiency that may stem from several potential factors including the quality of AGS thin film, unoptimized geometry of ZnO NWs, high resistivity of ZnO material and some contact issues [66,67]. Especially, it is observed that there is a low V_{oc} associated with the constructed core-shell solar cell. The open-circuit voltage (V_{oc}) of the p-n junction solar cell is given by the relation;

$$V_{oc} = \frac{nkT}{q} \ln \left(\frac{J_{sc}}{J_o} + 1 \right) \quad (2.2)$$

where J_{sc} and J_o are short-circuit current density and saturation current density, respectively. From this relation, it is evident that to get a large V_{oc} , J_o should be small. Since the saturation current density is inversely proportional to the minority carrier life time, to decrease it the minority carrier life time should be long [68]. It is a well-known fact that one-dimensional nanostructures based solar cell architectures offer a high surface/volume ratio, which give rise to the formation of surface defects, traps in depletion region and dangling bonds. These surface defects promote the surface recombination of photo-generated minority carriers and are resulting in short minority carrier life-times. Therefore, the observed low V_{oc} can be attributed to the short minority carrier life (high saturation current density) due to the high recombination rate in the core-shell device structure [69]. A considerable amount of similar results have been reported in literature for core-shell solar cells [7,69-72]. These studies showed that although these architectures provide promising short current densities, it was not the case for open-circuit voltages, which was either attributed to shunt path stemming from non-uniform core-shell structure or short minority carrier life time resulting from high recombination rate due to the large surface/volume ratio. It can thus be suggested that the careful synthesis of a nanostructured p-n junction is playing a critical role in determining the open circuit voltage that can be extracted from a core-shell architecture solar cell. Moreover, it can be expected that more efficient core-shell n-ZnO-NWs/p-AgGaSe₂ solar cells can be realized by producing ZnO NWs by

consideration of right aspect ratio and density for efficient light absorption, low-resistive ZnO and AGS thin films and formation of high quality ohmic contacts.

2.4 Conclusions

Dense arrays of ZnO nanowires (NWs) were successfully synthesized on different substrates such as silicon, soda lime glass (SLG), indium tin oxide (ITO) and polyethylene-terephthalate (PET) by employing hydrothermal technique. In particular, the growth of ZnO NWs on a flexible substrate such as PET is very important since it would allow the realization of flexible opto-electronic devices including photodetectors, solar cells and light emitting diodes. During the nanowire growth cycle, it was found that there was an important correlation between growth time and the diameter of NWs; in other words, there was an increase in diameter with increasing growth time, which was attributed to the coalescence of poor-aligned NWs at longer times. In addition to this, results revealed that there was a strong impact of the deposition route of ZnO seed layer, which were sol-gel and sputtering, on quality of synthesized ZnO NWs in terms of orientation with respect to the normal of the substrate, diameter, homogeneity in length, uniformity, and density of nanowires.

As an application of synthesized ZnO NWs, a core shell type solar cell based on n-ZnO-NWs/p-AgGaSe₂ (AGS) materials combination was fabricated. Prior to realization of the device structure, AGS thin films were deposited on SLG substrates via sputtering technique and then structural, electrical, and optical properties were investigated in detail. Once the best quality AGS thin films were obtained, ZnO NWs were decorated with it deposited with optimum deposition parameters for the fabrication of the device structure. From the measurement under 100 mW/cm² of simulated solar illumination, the open circuit voltage, short circuit current density, fill factor, and energy conversion efficiency were found to be as 0.098 V, 29.40 mA/cm², 60.25 % and 1.74 % respectively, which could be taken as encouraging results for next generation nanowire based solar cells and will serve as a base for future studies.

2.5 Acknowledgements

This work was supported by Turkish Scientific and Research Council (TUBITAK) under Grant No: 114F251.



3. DOPING AND ANNEALING EFFECTS ON STRUCTURAL, ELECTRICAL AND OPTICAL PROPERTIES OF TIN-DOPED ZINC-OXIDE THIN FILMS²

3.1 Introduction

In recent years, ZnO has received a great deal of attention due to its unique properties that can be exploited for a wide range of applications including solar cells [73], sensors [74], transparent electrodes and light emitting diodes (LED) [75]. Since it is a n-type wide-band gap material (3.37 eV) and has a high exciton binding energy (~ 60 meV) at room temperature, ZnO is regarded as one of the most important candidates for the realization of high-performance optoelectronic devices. In particular, it has been considered as a potential alternative to replace indium tin oxide (ITO) material, which is one of the best-known transparent conducting oxides (TCO) that provide high optical transparency and low electrical resistivity [76]. It is a well-known fact that despite its high transparency in the visible region, ZnO has poor electrical conductivity, which limits its usage for numerous possible applications as a TCO material [77]. Doping ZnO with some selective elements is a widely preferred approach to enhance its electrical properties. An increasing number of studies have revealed that the group III (Al, Ga, In) [54,78] and IV (Sn) elements are the potential dopants to improve the electrical and optical properties of ZnO thin films. Sn, having an ionic radius comparable with Zn ($r_{Zn}^{2+} = 0.074 \text{ nm}$, $r_{Sn}^{4+} = 0.070 \text{ nm}$), is recognized as one of the most convenient dopants, which provides an easy replacement of Zn by Sn ions [79]. So far, various methods have been suggested for the deposition of Sn-doped ZnO (SZO) thin films including sol-gel [80], chemical vapor deposition (CVD) [81], RF-sputtering [82], and pulsed laser deposition [83]. However, few researchers have focused on deposition of SZO thin films using layer by layer deposition of RF-sputtered ZnO and DC-sputtered Sn layers to obtain large scale uniformity and a precise

² This chapter has been published in Journal of Alloys and Compounds. Peksu, E., Karaağaç, H., (2018), Doping and Annealing Effects on Structural, Electrical and Optical Properties of Tin-Doped Zinc- Oxide Thin Films, Journal of Alloys and Compounds, 764, 616-625, doi: 10.1016/j.jallcom.2018.06.101.

control over doping concentration. The aim of the present study was thus to fabricate high quality ZnO and layer by layer grown Sn-doped ZnO thin films with different Sn concentrations, between 0.5 % and 3.0 %, on soda-lime glass substrates using RF/DC sputtering technique and then investigate the effects of doping concentration and annealing on their structural, electrical and optical properties.

3.2 Material and Methods

Undoped and Sn doped ZnO (SZO) thin films were successfully deposited on soda-lime glass (SLG) substrates at room temperature by a sequential sputtering of ZnO and Sn sources, performed in a NSC4000- Nanomaster sputtering system. Two-inch ZnO (99.999 % pure, 0.250 " thick, Kurt J. Lesker) and Sn (99.999 % pure, 0.250 " thick, Kurt J. Lesker) targets were used as sources for a layer by layer deposition of ZnO and Sn to obtain high quality SZO thin films in a controlled manner. Before the deposition cycle the distance between the targets and the substrate was adjusted to 20 cm. The vacuum chamber was then pumped down to a base pressure of 5×10^{-6} Torr and sequentially filled with pure Ar (99.99 % purity and 20 sccm flow rate) gas to reach a 5×10^{-3} Torr working pressure. The deposition of ZnO and Sn layers was realized by applying a fixed power of 70 W (RF) and 10 W (DC) to the corresponding targets. The deposition rates during the growth of the films was monitored simultaneously by a quartz crystal monitor (Inficon, XTM/2), which was recorded to be 2 Å/s and 1 Å/s for the deposition of ZnO and Sn layers, respectively. Prior to form SZO thin films, to increase the reliability of obtaining the same thickness of ZnO and Sn layers on SLG substrates, the optimization of corresponding layers was carried out independently by repeating three deposition cycle for each layer. Once the optimization was completed, ZnO and Sn layers, with thickness of 80 nm and 10 nm, were sequentially deposited on SLG substrate at room temperature to form ZnO/Sn/ZnO structured SZO thin film, which was labeled as reference sample. The thickness of the reference sample was exactly 170 nm, measured using a Veeco Dektak (150) profilometer, and the doping concentration was found to be 1.5 %, measured using energy dispersive X-ray analysis (EDXA) measurements. To obtain SZO thin films with 0.5 %, 1.5 % and 3.0 % Sn-doping concentrations, the thickness of Sn layer was adjusted properly while keeping the final thickness of the sample constant. The atomic percentage of Sn element for the desired 0.5 %, 1.5 % and 3.0 % Sn-doping concentrations was measured through EDXA measurements after the

deposition of SZO thin films and found to be exactly 0.49 %, 1.52 % and 2.99 %, respectively. In order to study the effect of post-annealing on structural, electrical and optical properties of the deposited SZO thin film at room temperature, they were heat-treated in the temperature range of 150 to 500 °C on a hot plate under N₂ gas flow for one hour. The post-annealing process was essential for the inter-diffusion of metallic Sn layer to form SZO thin films, which is a heat energy-driven process. The structural characterization of the undoped and Sn doped ZnO thin films was carried out by means of X-ray diffraction (XRD) measurements, in 2θ range 25° – 60° with a scan speed of 2°/min, using a GBC-MMA X-ray diffractometer with CuKα radiation source ($\lambda = 0.154$ nm). The optical properties were investigated by performing transmission and reflection measurements using a NKD- 7000 V spectrophotometer. The surface morphologies of the thin films were studied using a Scanning Electron Microscopy (SEM, Hitachi S-4100 FE equipped with EDS) and tapping mode Atomic Force Microscopy (AFM) (Shimadzu 9500J3). The room temperature resistivity of the SZO thin films was determined through four-point probe method, by using a Keithley 2400 Source-meter.

3.3 Results and Discussion

The structural analysis of undoped and Sn doped ZnO thin films at different concentrations (0.5 %, 1.5 % and 3.0 %) was carried out by XRD measurements. The diffraction peaks recorded for the corresponding doping concentrations (annealed at 500 °C) together with (zoom in) their main peaks are shown in Figure 3.1. It is clear from the figure that all the films exhibit a polycrystalline structure that can be characterized with (002) peak (JCPDS: 36-1451). This indicates the existence of a hexagonal wurtzite structure as well as the preferential orientation along the (002) plane, which is known to be stemming from its lower surface energy [84]. It is also apparent from the figure that the (002) peak intensity slightly decreases following the doping process for all the doping concentrations, which can be taken as a clear indication of the deterioration of the crystallinity after doping process due to the difference between the ionic radii of Sn ($r_{Sn^{4+}} = 0.070$ nm) and Zn ($r_{Zn^{2+}} = 0.074$ nm) [85]. However, as can be seen from the figure, there is no a significant difference between the intensity of 0.5 % and 1.5 % doped ZnO thin films. The incorporation of Sn atoms into lattice of ZnO may trigger an improvement in crystallinity by repairing many forms of crystal defects or deterioration of crystallinity by

generating a stress caused by the ion size difference exist between Zn and Sn atoms at the same time.

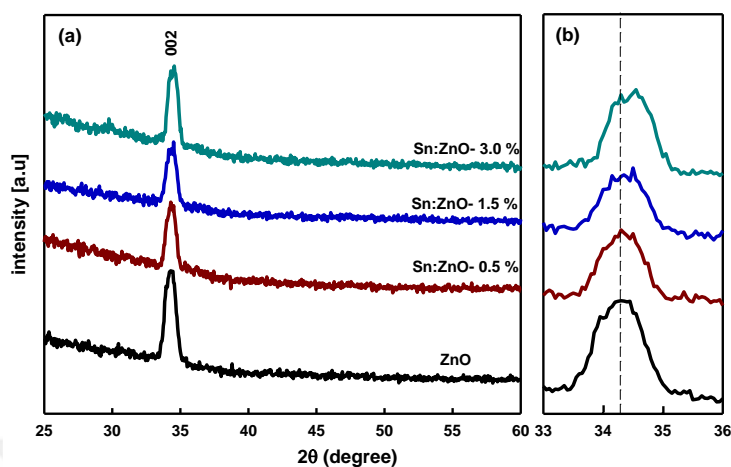


Figure 3.1 : XRD pattern recorded for (a) undoped and Sn doped ZnO thin films with (b) (zoom in) their (002) preferred peak.

There may be a competition between these two Sn doping role in the lattice structure. Therefore, if there is no a significant difference between the intensities of the samples at two different doping concentration, we may suggest that these two functions of Sn doping in the lattice are neutralized. It can be seen in Figure 3.1 (b) that the peak position shifts to higher angel (2θ) values at increasing Sn concentrations. For the 0 %, 0.5 %, 1.5 % and 3.0 % doping concentrations, the peak position was found to be located at 34.27° , 34.32° , 34.33° and 34.55° , respectively. This suggest a decrease in inter-planer spacing of (002) planes following the effective substitution of Zn by Sn ions in the ZnO lattice due to the smaller ionic radius of Sn with respect to that of Zn [85]. The substitution of larger Zn^{+2} ion by the smaller Sn^{+4} ion slightly contracts the ZnO matrix, which subsequently triggers the generation of a residual compressive stress in the structure of the films and the observed shift to larger 2θ values [86]. To further prove the incorporation of Sn atoms into lattice of ZnO, Rietveld analysis (using MAUD software) was applied to $500^\circ C$ annealed undoped and 1.5 % doped ZnO thin films, which have finer data resolution for this kind of analysis. For the refinement process, the hexagonal wurtzite crystal structure with $P6_3mc$ was preferred as starting structure. The obtained refinement plots for undoped and 1.5 % doped samples are shown in Figure 3.2 (a) and Figure 3.2 (b), respectively. In the plots, the red solid lines represent the calculated patterns with Rietveld refinement. In addition, the lower and middle parts of each graph indicates the

difference between the calculated and observed intensities and the expected Bragg reflection plane 2θ positions, respectively. The obtained Rietveld refinement data are listed in Table 3.1. The S shown in the table is standing for the goodness of the fit, which reflects the quality of the conducted fitting process.

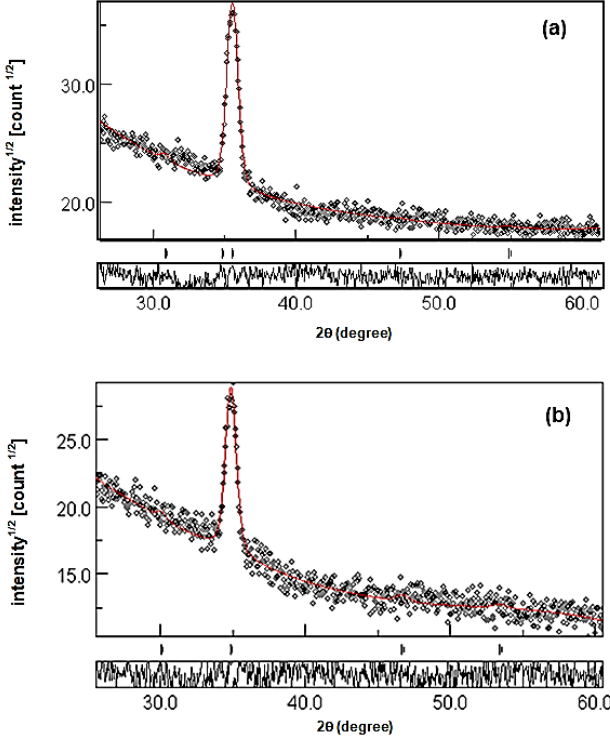


Figure 3.2 : Rietveld refinements for 500 °C annealed (a) undoped and (b) 1.5 % doped ZnO thin films.

Table 3.1 : Lattice parameters obtained following the Rietveld refinement.

Sample	Lattice parameters (Å)		Cell volume (nm ³)	S (Goodness of fit)
	Rietveld analysis			
	a = b	c		
x = 0.0	3.437793	5.143404	0.052613	1.06
x = 1.5	3.430401	5.142447	0.052405	1.33

This value was found to be 1.06 and 1.33 for undoped and doped sample, respectively, which reflects the presence of a well matching between the observed and calculated XRD patterns. As can be seen from the table, there is a decrease in lattice parameters (a = b and c) and unit cell volumes (from 0.052613 to 0.052405) following the Sn doping process. The observed modifications in cell volume and lattice parameters confirm the incorporation of Sn ions into

lattice of ZnO, which is expected to trigger a lattice contraction due to the substitution of Zn^{2+} ions by smaller Sn^{4+} ions.

In order to reveal the effect of annealing on the morphological, structural, electrical and optical properties of layer by layer sputtered SZO thin films, they were annealed in the temperature range of 150 °C to 500 °C on a hot-plate under N_2 gas flow (3 sccm) for one hour.

The XRD patterns of annealed SZO thin films, for the specified temperature range, at 0 %, 0.5 %, 1.5 % and 3.0 % Sn doping concentrations are shown in Figure 3.3 (a-d). It can be seen in the figure that following the annealing process there is a clear trend of increase in intensity of (002) peak with increasing annealing temperature for all the doping concentrations. This suggests an increase in the crystallinity of SZO thin films when subjected to a heat treatment. Namely, a pronounceable improvement in crystallinity of both doped and undoped ZnO films is taking place with annealing and increasing annealing temperature. In addition, it can be observed from the figure that the crystallinity deteriorates initially following the doping process and then gradually improves with increasing annealing temperature. This improvement can be ascribed to the recrystallization process by the supplied sufficient thermal energy. As mentioned earlier, the substitution of Zn by Sn in the ZnO lattice may trigger the formation of disorder as a consequence of the difference between the ionic radii of the elements, which may subsequently release and give rise to the generation of defects and dislocations. The observed enhancement in crystallinity, therefore, can be attributed to the elimination of the disorder, caused by these defects, with annealing [87]. It can also be inferred from Figure 3.3 that the undoped and Sn doped ZnO thin films annealed at 500 °C exhibit the best crystal quality. Furthermore, XRD analysis revealed that there is the peak shifting towards higher angles with increasing annealing temperature, which is an expected behavior that is closely related to the density of defects and the degree of stress generated through the substitution of larger Zn^{+2} ion by smaller Sn^{+4} ions, which is followed by post-annealing process [88,89]. As the Sn doping concentration or annealing temperature is increased, it is expected that more Sn atoms will be incorporated into zinc sites in ZnO matrix until reaching a solubility limit [90]. Doping SZO thin films over the solubility limit, for instance, may cause the formation of secondary phases of constituent elements, such as SnO, SnO_2 and Zn_2SnO_4 [85].

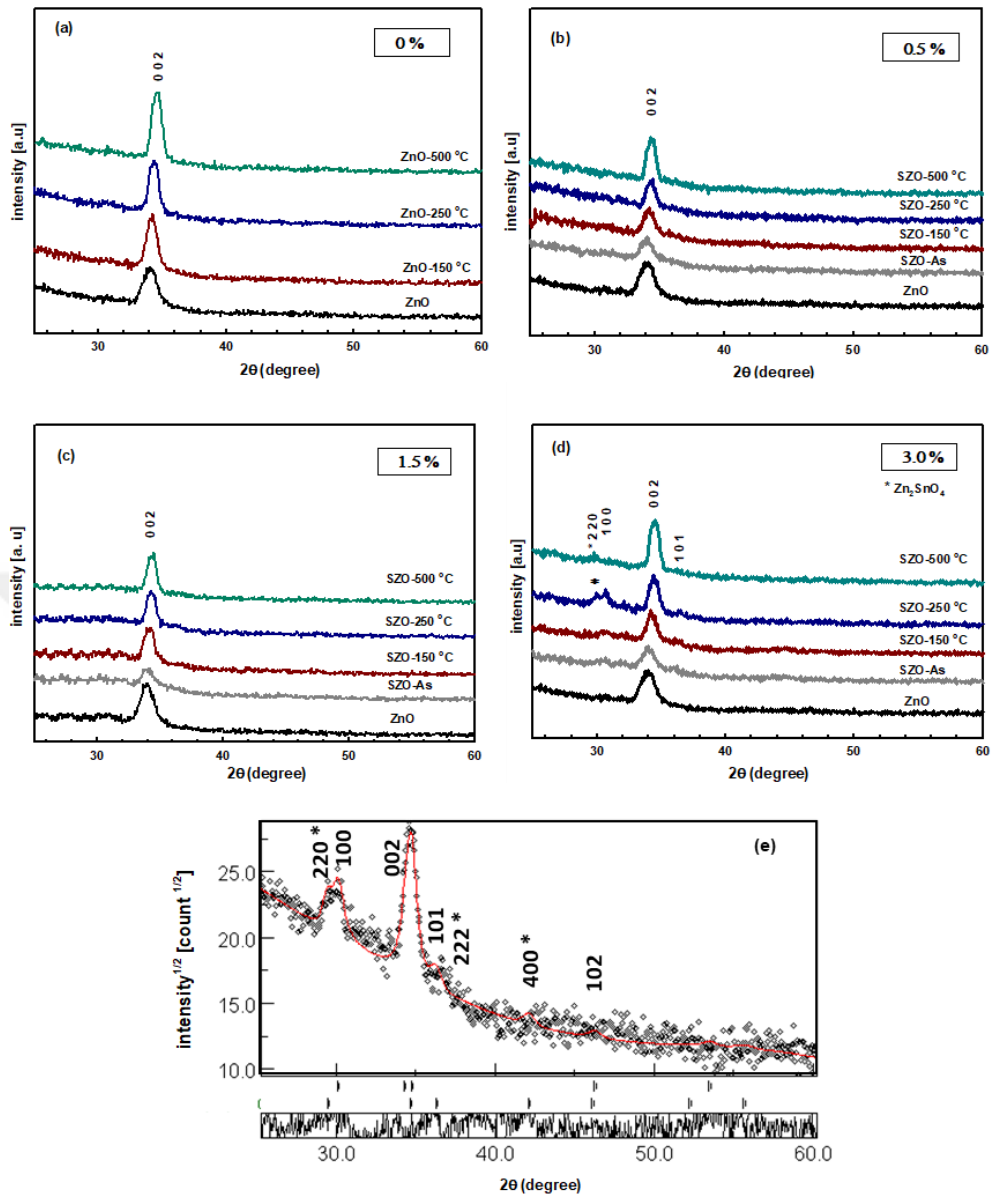


Figure 3.3 : XRD patterns recorded for (a) ZnO, (b-d) Sn doped ZnO thin films at different Sn concentrations (0.5-3.0 %) and annealed in the temperature range between 150 °C and 500 °C, (e) Rietveld refinements for 250 °C annealed and 3.0 % doped ZnO thin film.

In our case, it is clear from Figure 3.3 that no secondary phase appears in the XRD patterns except 3.0 % Sn doped ZnO film. As can be seen in Figure 3.3 (d), for the 3.0 % Sn doped and 250 °C annealed SZO thin film, not only ZnO peaks (100, 002, 101 and 102) but also some small peaks (220, 222 and 400) associated with Zn_2SnO_4 (*) secondary phase (JCPDS: 14-0381) were detected, which implies the saturation of Sn-doping over 1.5 % concentration. In

order to confirm and reveal the amount of the secondary phase (Zn_2SnO_4), the Rietveld refinement was applied to 3.0 % doped and 250 °C annealed ZnO thin film. The conducted refinement (with $S = 1.64$) plot with identified phases and associated reflecting planes is shown in Figure 3.3 (e). Based on this analysis, the amount of SZO and ZnO were calculated to be 35.82 % and 64.18 %, respectively. Therefore, from the obtained results, it can be concluded that at specific doping concentration of Sn both the incorporation of Sn into lattice of ZnO and the formation of a secondary phase (Zn_2SnO_4) in the lattice matrix can exist simultaneously.

The surface morphology of SZO thin films was analyzed using SEM measurements. The recorded micrographs of the as-grown and annealed films for all the doping concentrations are given in Figure 3.4. From the SEM images we can see that the surface of all the films is consisted of irregularly shaped small grains homogenously distributed across the film surface.

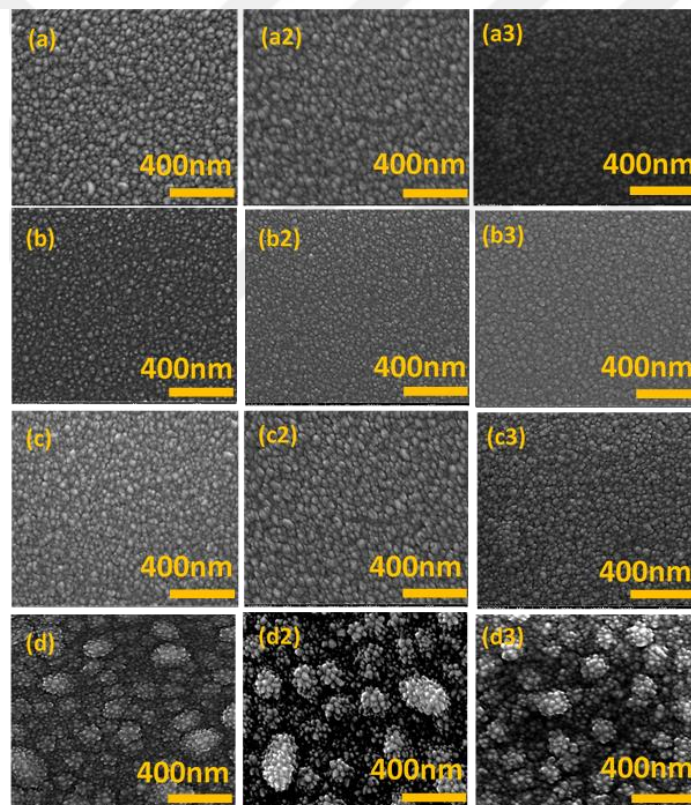


Figure 3.4 : SEM micrographs obtained for (a) 0 % (ZnO), (b) 0.5 %, (c) 1.5 % and (d) 3.0 % Sn doped ZnO thin films and films of (a-d) as-grown, (a₂-d₂) annealed at 250 °C and (a₃-d₃) 500 °C.

In addition to this, the images reveal that the average grain size of SZO thin films is smaller than that of ZnO thin films and decreases with increasing Sn concentration, which can be

attributed to the suppression of crystallization originated from the incorporation of more Sn atoms into ZnO matrix [80]. Moreover, as can be seen in Figure 3.4 (d), for 3.0 % doping concentration, mulberry-like structures are formed throughout the sample, which highlights the existence of doping concentration effect on the morphology of layer by layer sputtered SZO thin films. During the sputtering cycle to obtain 3.0 % Sn-doped ZnO thin film, a relatively thick (~ 20 nm) layer of Sn was deposited on the first ZnO layer at room temperature, which is then covered with the second layer of ZnO to construct a sandwich-like thin film structure. Therefore, when the second layer of ZnO is deposited on the relatively thicker Sn layer, a different thin film growth mechanism is taking place, which can be explained through the well-known metal assisted growth. In this model, Sn layer plays a critical role in thin film growth by acting as a typical catalyst to initiate nucleation process in the early stage of the crystallization. These mulberry-like structures are formed through the agglomeration of dozens of metal-assisted grown small granules. Although similar structures were observed on Ag layer [91], it is the first study that reports the formation of mulberry-like ZnO structures on Sn layer to form SZO thin films. It can be also seen from the SEM micrographs (a_2 - a_3 , b_2 - b_3 and c_2 - c_3) that there is no pronounceable change in surface morphology following the applying post-annealing process to the ZnO and SZO thin films doped with aforementioned doping concentrations.

In order to study the effect of Sn doping concentrations on the surface morphology of the fabricated SZO thin films the atomic force microscopy (AFM) images with the scan size of $1.5 \mu\text{m} \times 1.5 \mu\text{m}$ were recorded in the dynamic mode, which are presented in Figure 3.5 It is apparent from the 3D images that there is a strong correlation between doping concentration and the surface morphology of the films. We can see that the grain size of ZnO thin film is larger than that of 0.5 % and 1.5 % Sn doped ZnO thin films and the 0.5 % doped sample has the smallest surface roughness. In addition, the images reveal that with increasing doping concentration from 0.5 % to 1.5 % a denser thin film structure forms. With further increase in doping concentration over 1.5 %, large agglomerations appear, which was identified earlier from SEM images to be mulberry-like features. Surface roughness values for 0 % (ZnO), 0.5 %, 1.5 % and 3.0 % Sn doped ZnO thin films were measured to be 3.55 nm, 1.40 nm, 1.42 nm and 13.78 nm, respectively.

These roughness values were measured to be 3.66 nm, 3.32 nm, 1.84 nm and 14.40 nm for the respective doping concentrations after annealing the samples at 500°C under N_2 gas flow for

one hour as shown in Figure 3.6. To sum up, AFM measurements showed that the surface roughness of SZO thin films is smaller than that of undoped ZnO thin film and increases with increasing both Sn concentration and annealing temperature, which is in a good agreement with results reported in the literature [92].

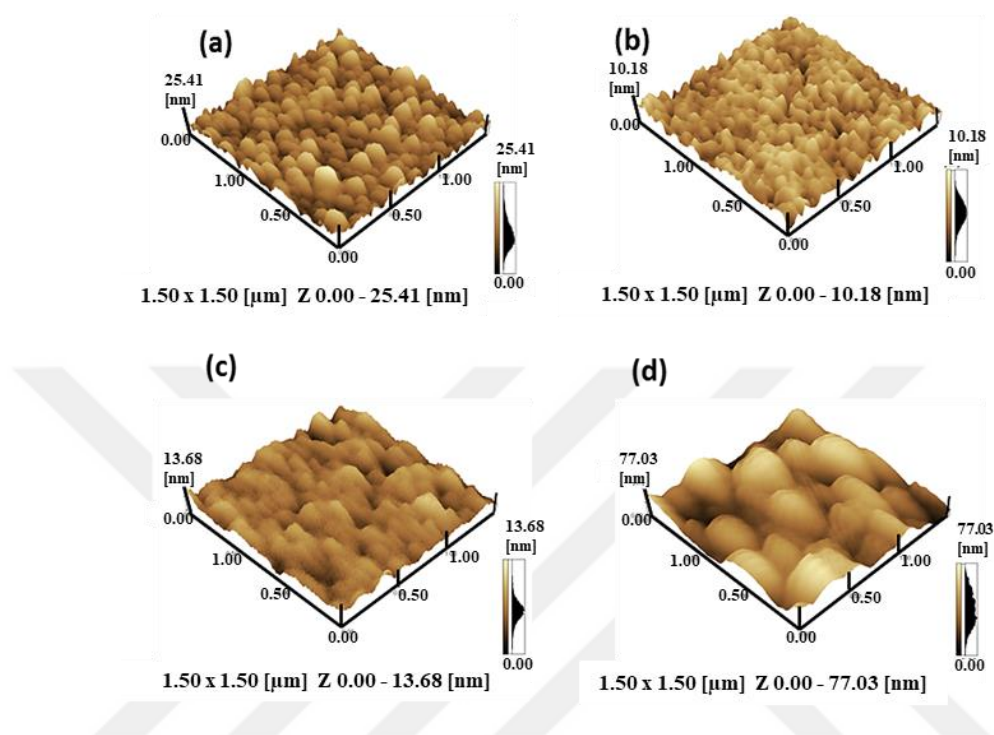


Figure 3.5 : 3-D AFM images with scanning area of $1.5 \times 1.5 \mu\text{m}^2$ recorded for as-grown (a) undoped, (b) 0.5 %, (c) 1.5 % and (d) 3.0 % Sn doped ZnO thin films.

These results are also in line with that obtained from XRD study, by which not only the deterioration of crystallinity following the doping process was observed but also a slight improvement in crystallinity with further increase in doping concentration was deduced.

As it is one of the key parameters required for a TCO material to be employed for a wide range of opto-electronic device applications, the optical transmittance measurements for both undoped and Sn doped ZnO thin films were conducted in the wavelength range of 350-1000 nm. The transmittance spectra of as-grown and the films annealed at 250 °C and 500 °C for undoped and Sn doped ZnO thin films are given in Figure 3.7. From the figures, it is clear that the transmittance decreases with increasing doping concentration for the as-grown SZO thin films. It is seen that, while the average transmittance for the undoped ZnO is about 90 % in the visible wavelength range (390- 800 nm), it is only ~ 17 % for the 3.0 % Sn doped ZnO for the same wavelength range.

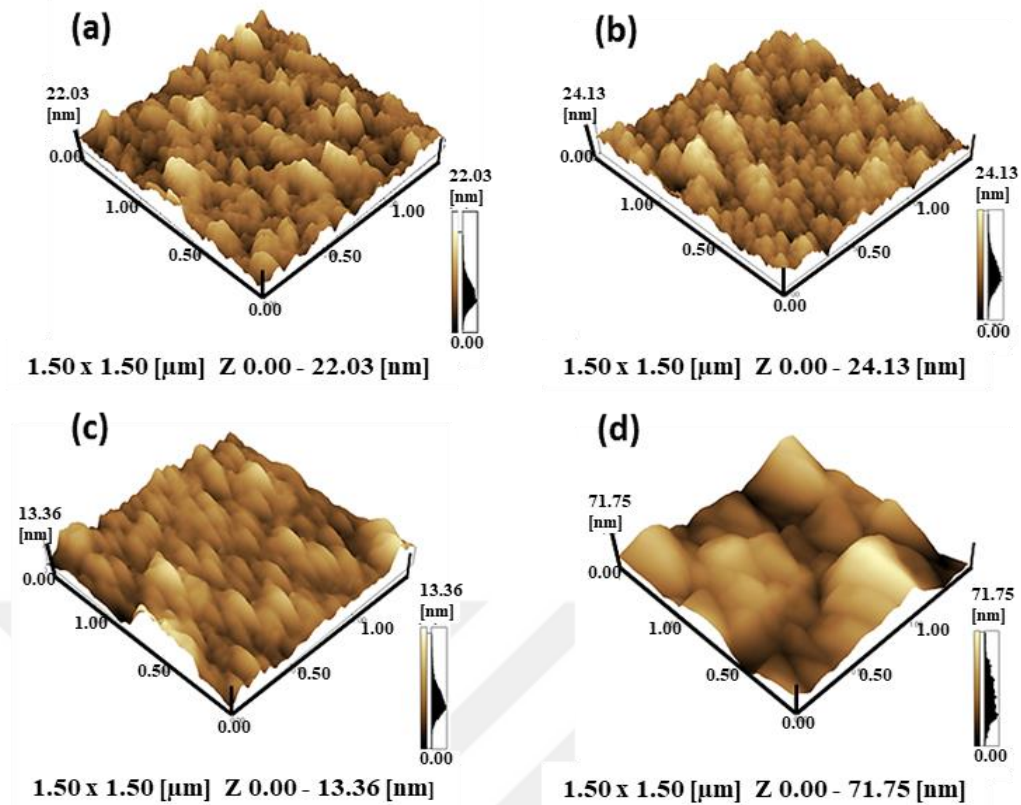


Figure 3.6 : 3-D AFM images recorded for (a) undoped, (b) 0.5 %, (c) 1.5 % and (d) 3.0 % Sn doped ZnO thin films annealed at 500 °C, scanning area 1.5 x 1.5 μm^2 .

The observed decrease in transmittance can be attributed to the deterioration of crystallinity following the substitution of larger Zn^{+2} ion by smaller Sn^{+4} ions when subjected to doping process, which is in line with the results obtained from XRD study. By contrast, it is apparent from the figure that the transparency of SZO thin film drastically increases when subjected to annealing process at 500 °C and has higher value as compared to undoped ZnO thin film in the visible range. This outcome is closely related to the improvement in crystallinity of the SZO thin films after post-annealing process and is supported by XRD results, by which an increase in peak intensity following the annealing process was revealed. The observed enhancement is also related to surface modification of the films following both post-annealing and doping processes, as deduced from SEM and AFM measurements. For the as-grown doped-ZnO thin films, although Sn dopant atoms are introduced into ZnO lattice, zinc sites are not occupied by Sn atoms owing to the insufficient thermal energy required for the inter-diffusion of the deposited Sn and ZnO thin film layers, which may trigger the aggregation of doping atoms at grain boundaries. This mechanism as well as the modification observed in surface roughness

following the annealing and doping processes may promote the scattering of incident light and subsequently an increase in reflectance [93].

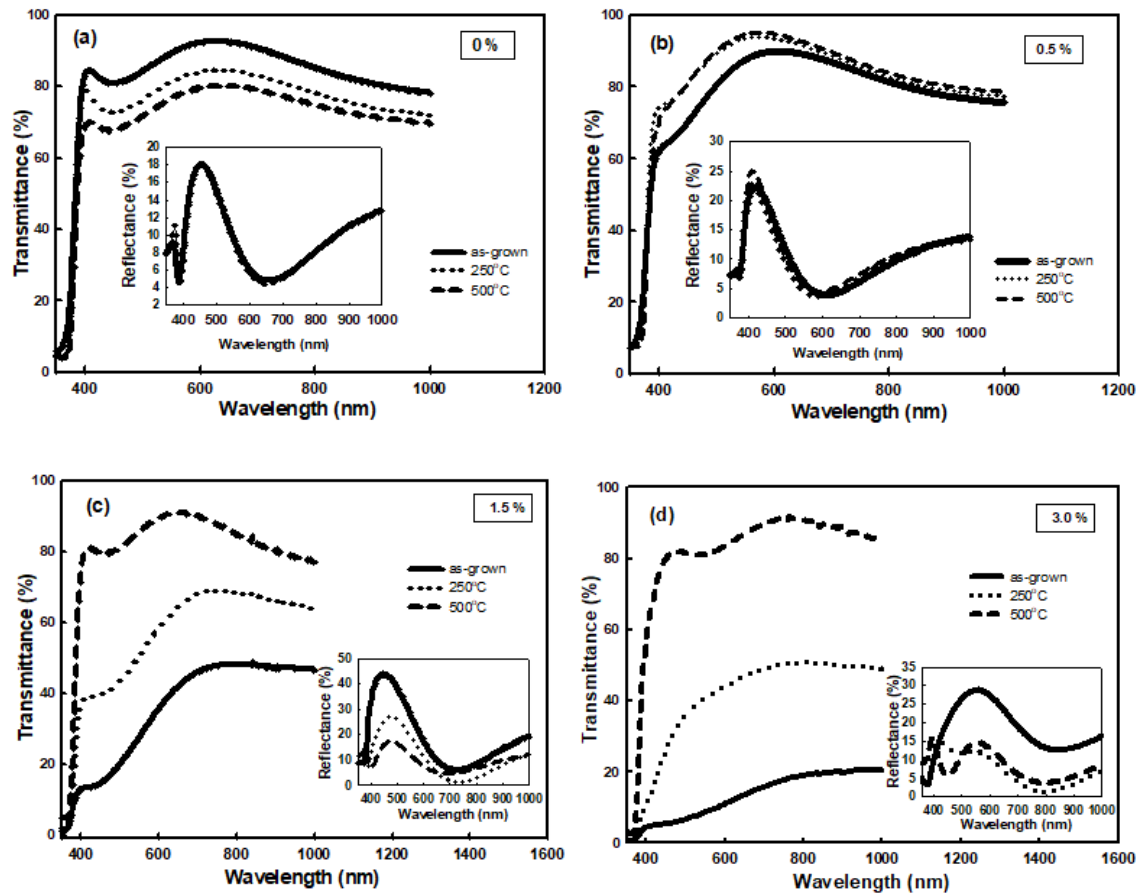


Figure 3.7 : Transmittance spectra of as-grown and post-annealed ZnO thin films with doping concentrations of (a) 0 %, (b) 0.5 %, (c) 1.5 %, (d) 3.0 %. The insets show reflectance spectra obtained for the respective doping concentrations and annealing temperatures.

In order to reveal this, the reflectance measurements for undoped and doped ZnO thin films were carried out as well in the wavelength range of 350-1000 nm. As can be seen from the inset in Figure 3.7, the as-grown ZnO thin film exhibits lower reflectance as compared to the doped samples. In addition to this, a significant decrease in reflectance for the Sn doped samples was revealed following the annealing process at 500°C. It is seen that, the average reflectance at 600 nm decreases from 28 % to 13 % with the increase of annealing temperature from room temperature to 500 °C, which can be ascribed to the elimination of disorder following the post-annealing process. Ultimately, the transmission measurements indicated an average transmittance of 90 % in the visible range for the doped and annealed (500 °C) ZnO thin films.

The absorption coefficient (α) of undoped and Sn doped ZnO thin films was calculated from the reflectance and transmittance spectra through the following relation [94].

$$\alpha = \frac{1}{t} \ln \left[\frac{(1-R)^2}{T} \right] \quad (3.1)$$

where t , R and T represents thickness of the film, reflectance and transmittance at a specific wavelength, respectively. Following the calculation of absorption coefficient, the optic band gaps of the deposited films were calculated from Tauc's model relation as [95]:

$$\alpha h\nu = A (h\nu - E_g)^n \quad (3.2)$$

where $(h\nu)$, A , E_g and n is standing for the photon energy, a constant of energy related to a specific material, the band gap and an index defining the type of transition (direct or in-direct) exists during absorption process, respectively. The index, n , reveals the nature of the absorption transitions and takes $1/2$ and $3/2$ values for the direct allowed and indirect allowed transitions, respectively. From the plot of (α) vs $(h\nu)$, the optic band gaps for as-grown undoped and Sn doped ZnO thin films were determined through the extrapolating the linear part of each curve, obtained with $n = 1/2$, to the $h\nu$ axis, as shown in Figure 3.8.

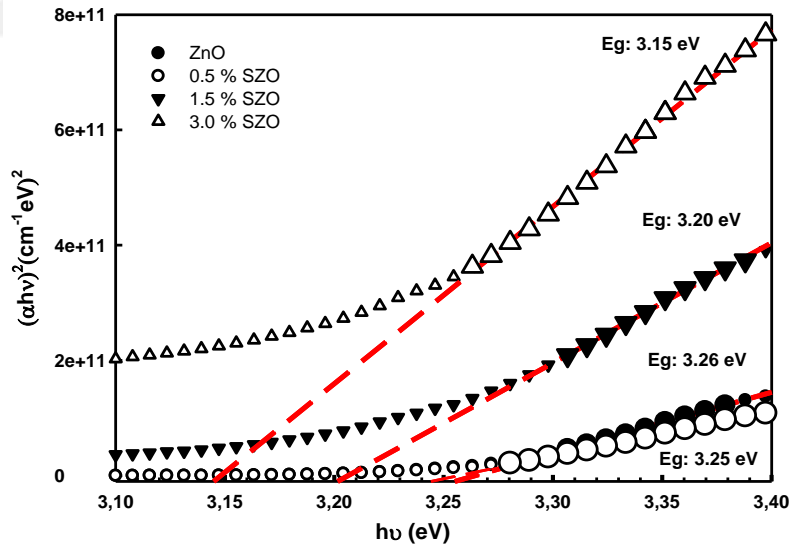


Figure 3.8 : The band gap determination, $(\alpha h\nu)^2$ versus photon energy ($h\nu$) relation, for as-grown ZnO and Sn doped ZnO thin films at different doping concentrations.

From the resulting plots it can be seen that the nature of the band gap for all the films is direct allowed. The band gaps for 0 % (ZnO), 0.5 %, 1.5 % and 3.0 % Sn doped ZnO thin films were

calculated to be 3.26 eV, 3.25 eV, 3.20 eV, 3.15 eV, respectively. It is obvious from the graphs that the absorption edge of the film shifts towards to higher energies (red shift) with increasing Sn concentration. A red shift with increasing doping concentration for as-grown film indicates a shrinkage in the band gap (E_g). A shrinkage of the bandgap correlates well with the impurity concentration and can be attributed to the generated defects and impurity levels following the doping process [96]. It is known that when Sn atoms are substituted in the Zn sites, they can act as an ionized donors, which promote the generation of deep states in the forbidden band gap energy region [97]. This findings support the data obtained from XRD study and are consisted with those of reported in [98,99]. Namely, the observed deterioration of crystallinity after doping process for as-grown SZO thin films, deduced from XRD, suggests the generation of disorder that promotes the formation of defects, responsible for the aforementioned deep levels in the forbidden band gap. In contrast to doping effect, the annealing process applied to both undoped and Sn doped ZnO thin films resulted in a band gap enhancement.

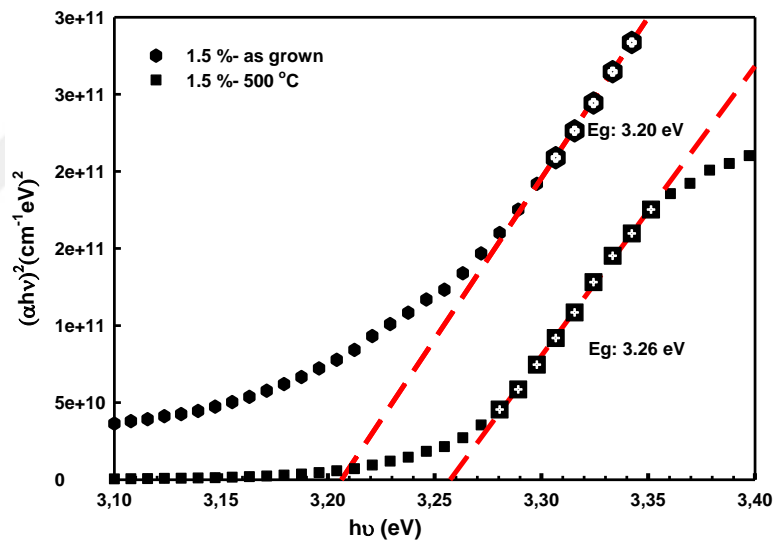


Figure 3.9 : The band gap determination for as-grown and post annealed 1.5 % Sn doped ZnO thin film.

It was found that, for instance, the band gap energy is increasing from 3.20 eV to 3.26 eV with increasing annealing temperature from room temperature to 500 °C for the 1.5 % doped ZnO thin film, as shown in Figure 3.9. The observed enhancement with annealing and increasing annealing temperature can be ascribed to the elimination of defects introduced by incorporation

of Sn atoms from the forbidden band gap region with improvement in degree of crystallinity, as supported by XRD results as well.

As a final part of the present study, the room temperature (RT) resistivities for the undoped and Sn doped ZnO thin films were determined using four-point-probe method. Following the confirmation of the ohmic nature of the contacts through current-voltage (I-V) characteristics in the voltage range of (-2 V) – (+2 V), the room temperature resistivity for 0 % (ZnO), 0.5 %, 1.5 % and 3.0 % Sn doped ZnO thin films annealed at different temperatures were calculated. The RT resistivity value for the undoped ZnO thin film was found to be around $5 \times 10^5 \Omega \cdot \text{cm}$, which confirms the well-known highly resistive nature of this material. After the electrical measurements for the SZO thin films, it was deduced that the resistivity of the films first decreases with increasing both annealing temperature and Sn concentration, reaching the lowest value of $9.0 \times 10^{-3} \Omega \cdot \text{cm}$ at annealing temperature of 250 °C for 1.5 % Sn content, and then increases with further increase in doping concentration and annealing temperature. This behavior correlate fairly well with that reported by Saurdi et al [100] for Sn doped ZnO thin films.

Table 3.2 is revealing that 1.5 % doping and the subsequent 250 °C annealing process led to a dramatic reduction in resistivity ($9.00 \times 10^{-3} \Omega \cdot \text{cm}$), almost seven orders of magnitude, as compared to that of undoped one ($3.90 \times 10^4 \Omega \cdot \text{cm}$). The lowest resistivity value reached in the present study is three orders of magnitude lower than that reported for the SZO thin films in the literature [101]. These results suggest that beyond 1.5 % Sn concentration and over the 250 °C annealing temperature, the electrical resistivity of the SZO thin films decrease, which is closely related to the observed modifications in structure, morphology and as well as the formation of local defects in the forbidden band gap region. It is expected that conductivity (reciprocal of resistivity) will be increased through the substitution of larger Zn^{+2} ion by smaller Sn^{+4} ions by contributing free electrons since Sn^{4+} ions provide two free electrons by this substitution in the ZnO lattice [102]. However, when the solubility limit of the doping element is surpassed it may cause a reduction in conductivity due to the increase in scattering mechanisms that can be induced by inactivated Sn atoms in the ZnO matrix as well as the secondary phases (Zn_2SnO_4) of the constituent elements observed in XRD patterns for doping concentration over 1.5 %. In addition, elevating the annealing temperature over 250 °C may cause the incorporation of O_2

through grain boundaries and compensate the Sn-originated donor levels, which contribute to the current through donating free electrons.

Table 3.2 : Electrical resistivity values measured for as-grown and annealed Sn doped ZnO thin films.

Doping Concentration (% atomic)	RESISTIVITY (Ωcm)		
	Room Temperature	250 °C	500 °C
0	1.80×10^5	3.90×10^4	7.43×10^4
0.5	1.50×10^4	3.80×10^3	9.87×10^3
1.5	10.37	9.80×10^{-3}	40.40
3.0	720.00	4.80×10^{-2}	359.20

3.4 Conclusions

Doping and annealing effects on structural, morphological, optical and electrical properties of undoped and Sn doped ZnO thin films, between 0.5 and 3.0 %, were investigated. ZnO/Sn/ZnO sandwich structure were deposited on SLG substrate by RF/DC sputtering method to obtain Sn doped ZnO thin films. Structural analysis revealed that the preferential orientation is along the (002) plane for all the films and there is a deterioration of the crystallinity after doping process due to the difference between the ionic radii of Sn ($r_{\text{Sn}^{4+}}$) and Zn ($r_{\text{Zn}^{2+}}$). However, following the applying post-annealing process a significant improvement in crystallinity of both doped and undoped ZnO films was observed. AFM measurements have shown that there is a significant modification in surface morphology following the doping process and mulberry-like structures are formed for 3.0 % doping concentration throughout the sample. The transmission measurements indicated an average transmittance of 90 % in the visible range for the Sn-doped ZnO films, when annealed at 500 °C under N₂ gas flow. The band gap enhancement (red shift) from 3.26 eV to 3.15 eV with the increase of Sn content was observed for the SZO thin films. After the electrical measurements for the SZO thin films, it was deduced that the resistivity of the films first decreases with increasing both annealing temperature and Sn concentration,

reaching the lowest value of $9.0 \times 10^{-3} \Omega \cdot \text{cm}$ at annealing temperature of 250 °C for 1.5 % Sn content (three orders of magnitude lower than Sn doped ZnO reported in the literature) and then increases with further increase in doping concentration and annealing temperature. The fabrication of SZO thin films in the present study with an average transmittance of 90 % in the visible range and a $9.0 \times 10^{-3} \Omega \cdot \text{cm}$ resistivity value reveal that the obtained results represent an excellent initial step for us toward the production of a high transparent-conductive-oxide (TCO) material by using relatively cheap and abundant constituent elements in our future studies.

3.5 Acknowledgements

This work was supported by Istanbul Technical University under Grant No: BAP-39349.



4. A THIRD GENERATION SOLAR CELL BASED ON WET-CHEMICALLY ETCHED Si NANOWIRES AND SOL-GEL DERIVED $\text{Cu}_2\text{ZnSnS}_4$ THIN FILMS³

4.1 Introduction

Today, silicon is the leading material used in photovoltaic solar cells based on its various advantages such as cost efficiency, stability, high reliability, well balanced electrical/optical properties and well established processing techniques [103]. As an alternative to this material based solar cells, a search for highly efficient low cost inorganic solar cells has also occurred over the last two decades. Research has been focused on using various materials in solar cells, such as; amorphous Si, organic, II-VI and I-III-VI₂ materials. Most of today's thin-film solar cells are mainly based on CuInSe_2 (CIS), $\text{CuIn}_x\text{Ga}_{1-x}\text{Se}_2$ (CIGS) and CdTe semiconductor materials, which are consisted of rare, expensive and toxic elements (In, Te, Ga, and toxic Cd) [30,31]. Although these solar cells have reached the commercialization stage with high power conversion efficiencies, the requirement of using rare and expensive elements severely limit the mass production and deployment of them. Therefore, in recent years, a considerable research effort has been focused on development of new photovoltaic absorber materials that can embody earth-abundant, low-cost, and environmentally benign constituent elements for the realization of highly efficient thin film solar cells at lower cost. $\text{Cu}_2\text{ZnSnS}_4$ (CZTS) compound has recently emerged as a potential photo-absorber material for thin-film solar cells due to their superior physical and chemical properties, which addresses almost all the issues related to the drawbacks of the aforementioned materials [104,105]. The kesterite structured CZTS is a quaternary (I₂-II-IV-VI₄) p-type material with a high absorption coefficient (10^4 cm^{-1}) and direct band gap energy (~1.45 eV) that match the most intense part of solar spectrum reaching

³ This chapter has been published in Journal of Alloys and Compounds. Peksu, E., Karaağaç, H., (2019), A Third Generation Solar Cell Based on Wet-Chemically Etched Si Nanowires and Sol-Gel Derived $\text{Cu}_2\text{ZnSnS}_4$ Thin Films, Journal of Alloys and Compounds, 774, 1117-1122, doi: 10.1016/j.jallcom.2018.10.012.

the surface of the earth [33]. It is regarded as a potential next generation absorber layer that can allow the fabrication of environment friendly and cost-effective high efficient solar cells with theoretical power efficiencies up to 32.2% [34]. Up to now, a wide range of deposition techniques have been reported for the fabrication of CZTS thin films such as thermal evaporation [106], electron beam evaporation [41], sputtering [107], pulsed laser deposition [108], sol-gel [109] and chemical vapor deposition [110]. Among the aforementioned techniques, the sol-gel method has numerous advantages such as the well control over the homogeneity, less energy consumption, no need for special or expensive equipment and ease of large-scale production [111]. In addition to these, sol-gel method allows to modify the electrical, optical and structural characteristics of CZTS thin films in a controlled manner by altering growth parameters such as precursor concentration, solution temperature and pre-heating temperature.

In recent years, although there are large number of studies in the literature related to the deposition of high quality CZTS thin films by several deposition routes, the works on the construction of this material based third generation solar cells are very limited [30,31,33,104,112]. The aim of this work, therefore, was an attempt to fill this gap in the literature and test the photovoltaic performance of the sol-gel derived CZTS thin film in a third generation solar cell device architecture. According to our best knowledge, a solar cell based on Si nanowires decorated with a thin layer of CZTS for the realization of a low cost core-shell like Si-nanowire (NW) /CZTS structured solar cell has been reported for the first time in the present study. The constructed solar cell structure couples the efficiency of the 1st generation solar cells (Si-based solar cells) with the benefits of the 3rd generation solar cells (core-shell device architecture). In other words, the combination of an absorber thin film layer (CZTS) with a high absorption coefficient and the commercialized Si technology as well as the unique features (light trapping, enhanced charge collection and large surface-to-volume ratio) of Si nanowires enables the realization of cost-effective high efficient solar cells. The fabrication of the third generation device structure with CZTS/Si material combination was particularly preferred due to both the simplicity of the hetero-junction and the similarity in the lattice structures of the materials that allows us to form high quality p-n heterojunction with low lattice mismatching, which is essential for the realization of high efficient hetero-junction solar cells.

4.2 Material and Methods

For the fabrication of stoichiometric high quality thin films, a production route based on a combination of spin-coating and thin film deposition by sol-gel processes was preferred, which is believed to address many issues associated with the difficulties reported so far in literature in obtaining highly stoichiometric CZTS thin films. The CZTS thin films were deposited onto both soda lime glass (SLG) substrates and n-Si nanowire (NW) arrays derived from the n-Si wafer through the electroless etching technique, details of which was given elsewhere [49]. The solution for the fabrication of CZTS thin films was prepared by dissolving copper acetate (Acros, 98%, 1.7 M), zinc acetate (Sigma Aldrich, 99.99%, 1.1 M), tin chloride (Sigma Aldrich, 98%, 0.7 M), thiourea (99% Sigma Aldrich, 6.5 M), and triethanolamine (Alfa Aesar, 98%, 1.2 mL) in 2-methoxyethanol (99%, Sigma Aldrich, 10 mL). The resulting solution was then gently stirred at room temperature for 2 h, which led to obtaining of a homogenous transparent yellow solution. Following a two day aging process, the solution was filtered through a 0.46 μm syringe filter and then deposited onto both SLG and Si-NW arrays at 3000 rpm for 30 s. To remove the organic solvent the heat-treatment at 200 $^{\circ}\text{C}$ for 90 min on a hot plate under ambient atmosphere was conducted for each deposited layer. The thickness of each deposited layer was measured by a surface profilometer (a Veeco Dektak 6 M) and found to be around 600 nm. After preheating process, the post-annealing process at 350 $^{\circ}\text{C}$ under inert gas flow (N_2) was applied to the deposited films so as to trigger the reaction of the constituent elements, which is required for the formation of mono-phase CZTS thin films. The structural (X-ray diffraction (XRD), a GBC-MMA X-ray diffractometer with $\text{CuK}\alpha$ radiation source ($\lambda = 0,154\text{nm}$), and a Horiba-Jobin Yvon i550 Raman instrument, equipped with a laser providing an excitation wavelength of 532 nm) and optical (Reflection and Transmission, a NKD-7000V spectrophotometer) properties of the deposited CZTS thin films deposited onto SLG were investigated first prior to the construction of n-Si NWs/p-CZTS structured solar cell by decoration of the produced Si NWs (with diameters ranging from 20 to 80 nm and lengths up to 3.5 μm) with a thin layer (600 nm) of CZTS thin film. Following that, ~ 60 nm thick silver dot contacts were made on top of CZTS thin film by thermal evaporation to form the ohmic top-contacts of the solar cells structure by using a copper-shadow mask with a dot pattern (1 mm diameter). As a back contact of the solar cells, the back side of the unpolished n-Si

wafer (1-10 Ω -cm) was coated with a 150-nm thick silver thin film layer via thermal evaporation technique. The schematic representation of the constructed device is shown in Figure 4.1.

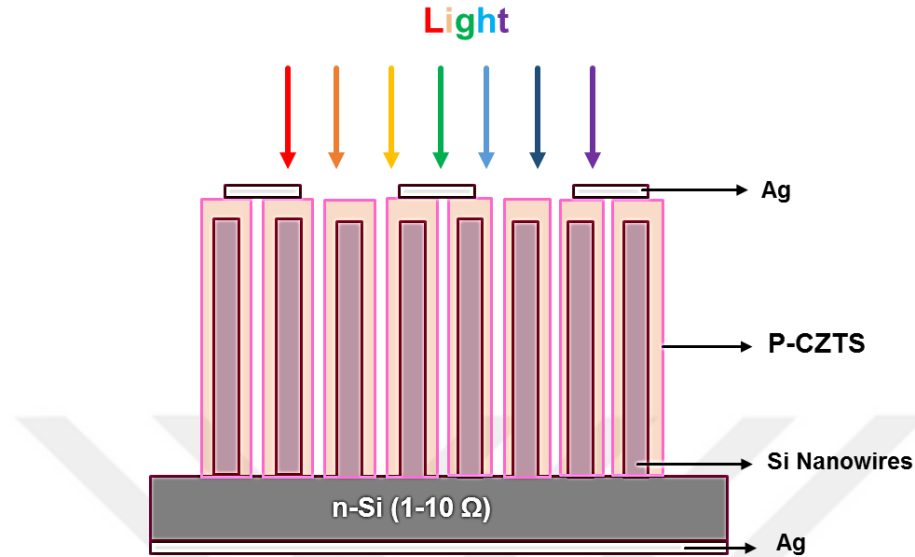


Figure 4.1 : Schematic representation of the fabricated solar cell by decoration of Si NWs with a thin layer of CZTS.

The photovoltaic behaviour of the constructed prototype solar cell was examined under AM 1.5G illumination (100 mW/cm^2) by using a solar simulator (LCS-400 solar simulator). From the measured PC controlled Current – voltage characteristics of the solar cells under dark and light illumination conditions, the solar parameters including open-circuit voltage (V_{oc}), fill factor (FF), short-circuit current (I_{sc}) and power conversion efficiency were calculated.

4.3 Results and Discussion

The elemental composition of the deposited CZTS thin film was determined through energy dispersive X-ray analysis (EDS) measurements, which was conducted for the film annealed at $350 \text{ }^\circ\text{C}$. The atomic percentages of copper (Cu), zinc (Zn), tin (Sn) and sulfur (S) were found to be 26.45, 12.50, 11.69 and 49.36 %, respectively, which reveals the presence of a slightly Cu-rich and Sn-poor chemical composition of the fabricated CZTS thin films. In other words, the $\frac{\text{Cu}}{\text{Zn}+\text{Sn}}$, $\frac{\text{Zn}}{\text{Sn}}$ and $\frac{\text{S}}{\text{Cu}+\text{Zn}+\text{Sn}}$ ratios were calculated to be 1.09, 1.07, and 0.97, respectively, which indicates the fabrication of CZTS thin films with a stoichiometry of $\text{Cu}_{2.12}\text{Zn}_{1.00}\text{Sn}_{0.94}\text{S}_{3.94}$. It is also important to note that even the film is annealed at $350 \text{ }^\circ\text{C}$, there is still a nearly stoichiometric

composition, which does not require any post-production processes such as sulfurization process, needed to compensate the loss of highly volatile sulfur during the post-annealing stage. This suggests the elimination of one additional step for the fabrication of CZTS absorber layer and highlights the importance of the preferred deposition route for the fabrication of the films.

In order to determine the structural characteristics of the deposited CZTS thin film the XRD in combination with Raman scattering measurements were performed for as-grown (only pre-heated) and annealed (350 °C) samples. The optimization processes for the CZTS absorber layer prior to its incorporation into the n-Si-NWs/p-CZTS device structure was initially applied to the films deposited on soda-lime-glass (SLG) substrates.

Figure 4.2 (a) presents the XRD patterns of the as-grown and annealed CZTS thin films deposited on SLG substrates in 2θ range 20-60°. From the pattern recorded for as-grown film it can be noted that the deposited film is polycrystalline in nature and consisted of kesterite CZTS (JCPDS Card No: 26-0575) and Cu_{2-x}S (JCPDS Card No: 23-0958) phases with indexed corresponding reflection peaks. It is also apparent from the figure that the observed secondary phase (Cu_{2-x}S) disappears and there is an increase in intensity of peaks associated with a single kesterite CZTS phase (JCPDS Card No: 26-0575) when the film is annealed at 350 °C. In other words, a stoichiometric monophasic kesterite CZTS phase with (112) preferred orientation is formed at only 350 °C annealing temperature. As XRD is insufficient to distinguish the kesterite CZTS phase from its secondary phases due to their similar structures [113], Raman measurement is required to confirm the formation of pure CZTS for the annealed film. Figure 4.2 (b) shows Raman spectra of CZTS thin film annealed at 350 °C. As can be seen from the figure, several peaks located at 255, 289, 339, 350 and 370 cm^{-1} are observed in the spectrum which are known to be associated with CZTS phase [113]. The results thus obtained from Raman scattering analysis are compatible with those derived from XRD study and confirm the presence of monophasic kesterite phase without any secondary phases in the structure following the post-annealing process at 350 °C.

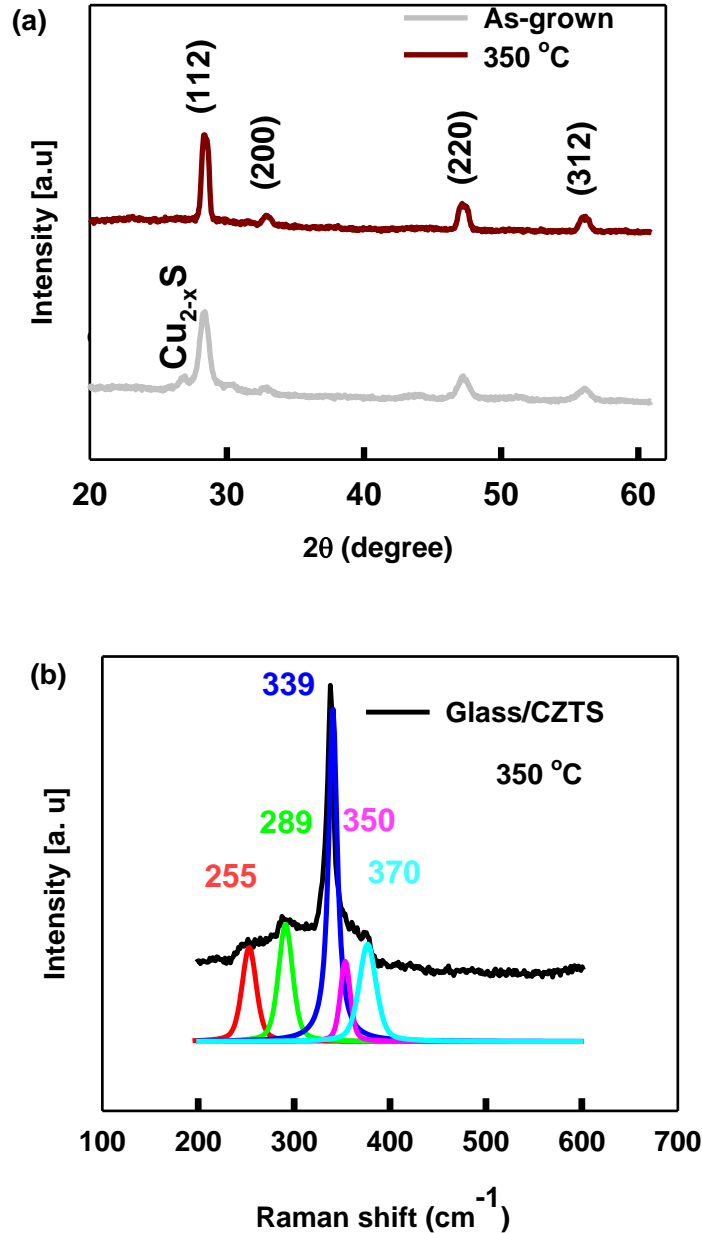


Figure 4.2 : (a) The XRD patterns recorded for as-grown and annealed CZTS thin film deposited on SLG substrate. (b) Raman spectra for the same CZTS film.

The transmission spectrum for the CZTS thin film deposited on SLG substrate (annealed at 350 °C) is shown in Figure 4.3. From the measured transmittance and reflectance spectra, which is below 10% (not shown here) in our case, the absorption coefficient (α) was first calculated by using the following relation [114];

$$T = (1 - R)^2 e^{-\alpha d} \quad (4.1)$$

where α , d , and R are the absorption coefficient, the film thickness and the reflectance, respectively. The optical band gap energy was then obtained from the Tauc plot [115],

$$(\alpha h\nu)^{\frac{1}{n}} = A(h\nu - E_g) \quad (4.2)$$

where A , h , ν , and E_g are a constant, Planck constant, incident photon frequency and the band gap energy, respectively. The n in the expression is an exponent that determine the nature of the optical transition (direct or indirect). To determine the optical band gap energy of the film the absorption coefficient versus photon energy ($h\nu$) plot for $n = \frac{1}{2}$ is also given as an inset in Figure 4.3. As can be seen from the figure, from the intersection of the straight line with the energy axis at $\alpha = 0$, the band gap energy was determined, which was calculated to be 1.55 eV for the annealed film. The obtained energy value is in a good agreement with the results reported for the same material in the literature [109,116]. Following the optimization of CZTS thin films on SLG substrates, a prototype solar cell based on decoration of Si-nanowires (NWs) with CZTS absorber layer was constructed.

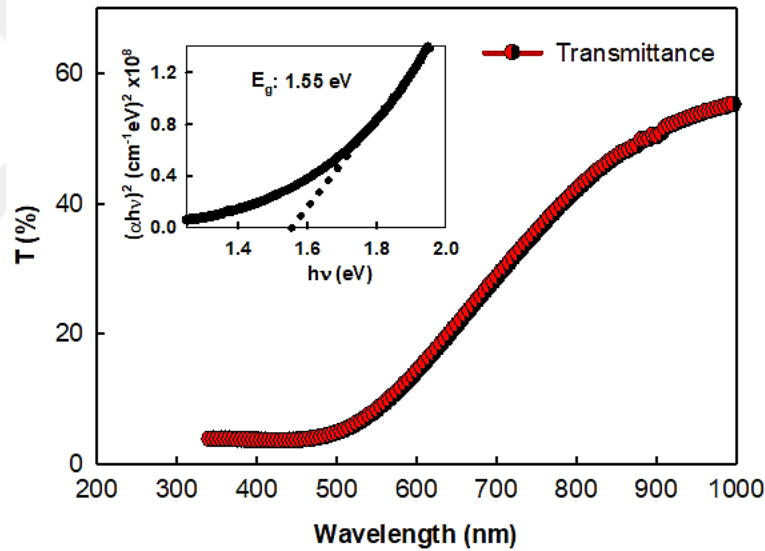


Figure 4.3 : Transmission spectrum for the CZTS annealed thin film deposited on SLG substrate. The inset figure presents the relationship of the absorption coefficient versus photon energy for the same CZTS thin film.

Figure 4.4 shows the cross-sectional and tilted-SEM images of the fabricated uncoated (a-b) and CZTS-coated Si NWs (c-d) with different magnifications. Figure 4.4 (a-b) present the top-view and tilted-view SEM images of bare Si-NWs, which reveal a nearly homogenous etching profile as well as an etching depth of $\sim 3.5 \mu\text{m}$. The average diameter of the produced NWs were found to be varying from 20 to 80 nm. Figure 4.4 (c-d) show the top-view and tilted-view SEM images of the Si-NWs decorated with a 600 nm thick CZTS layer. It is apparent from the images that almost all the NWs both

longitudinally and radially are completely coated with CZTS layer, demonstrating the formation of a high interaction interface between Si-NWs and CZTS absorber layer. It is also obvious that the tops of CZTS-coated Si NWs exhibit a bunching characteristic.

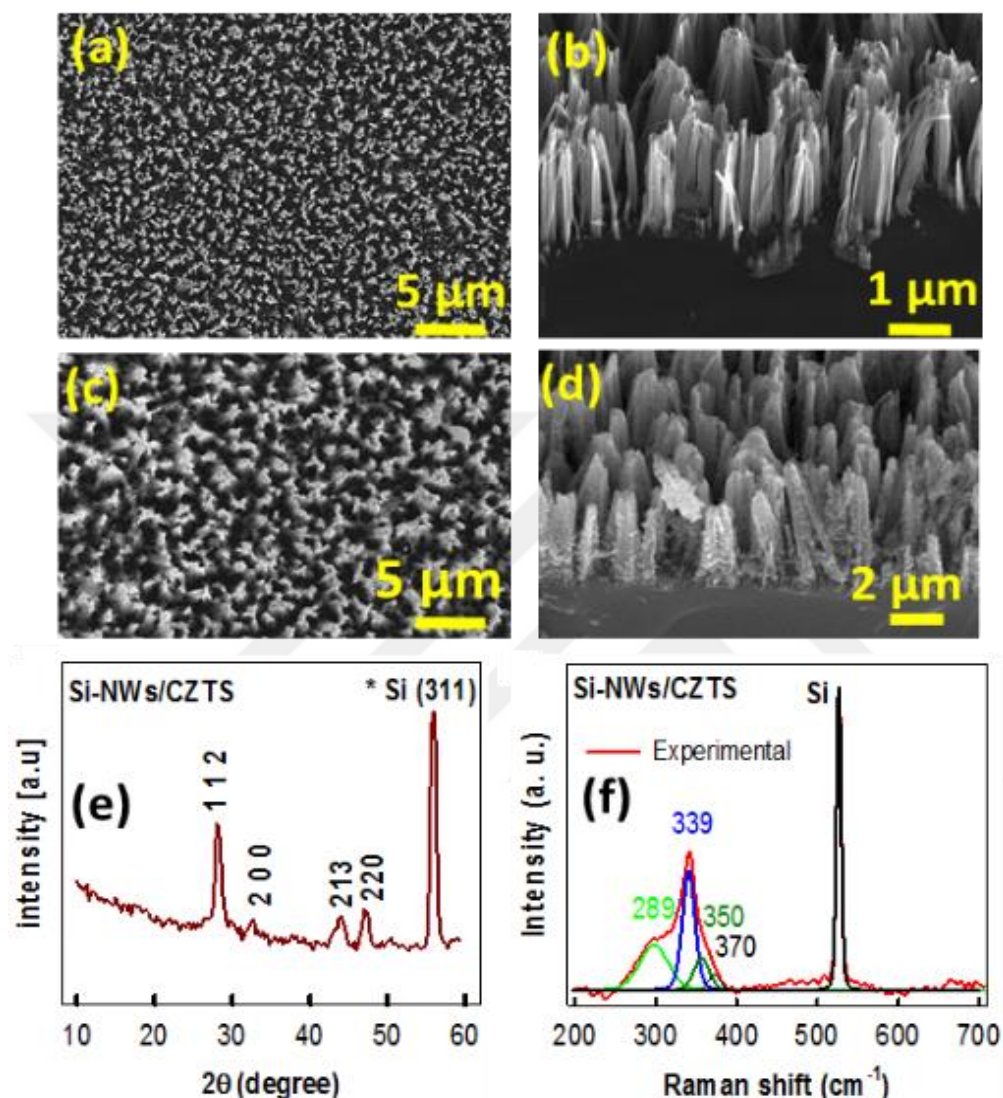


Figure 4.4 : (a - b) Top-view and tilted-view SEM images of the fabricated bare Si-NWs. (c - d) Top-view and tilted-view SEM images recorded for the Si-NWs decorated with a 600 nm thick CZTS layer. (e) XRD and (f) Raman scattering spectra of Si-NWs coated with the CZTS absorber layer.

The XRD pattern of the constructed n-Si-NWs/p-CZTS structure is shown in Figure 4.4 (e). From the recorded pattern it can be deduced that only reflection peaks associated with CZTS (112, 200, 213 and 220) and Si (311) are distinguishable. As in the case of CZTS film deposited on SLG substrates, Raman measurement was also conducted to detect the possible secondary phases and confirm the XRD results. In Figure 4.4 (f), the Raman spectrum of n-Si-NWs/p-CZTS device configuration is

shown with identified peaks associated with CZTS (289, 339, 350 and 370 cm^{-1}) and Si (521 cm^{-1}) structure, which verifies the formation of a mono-phase CZTS thin film in the solar cell device structure at a 350 °C annealing temperature.

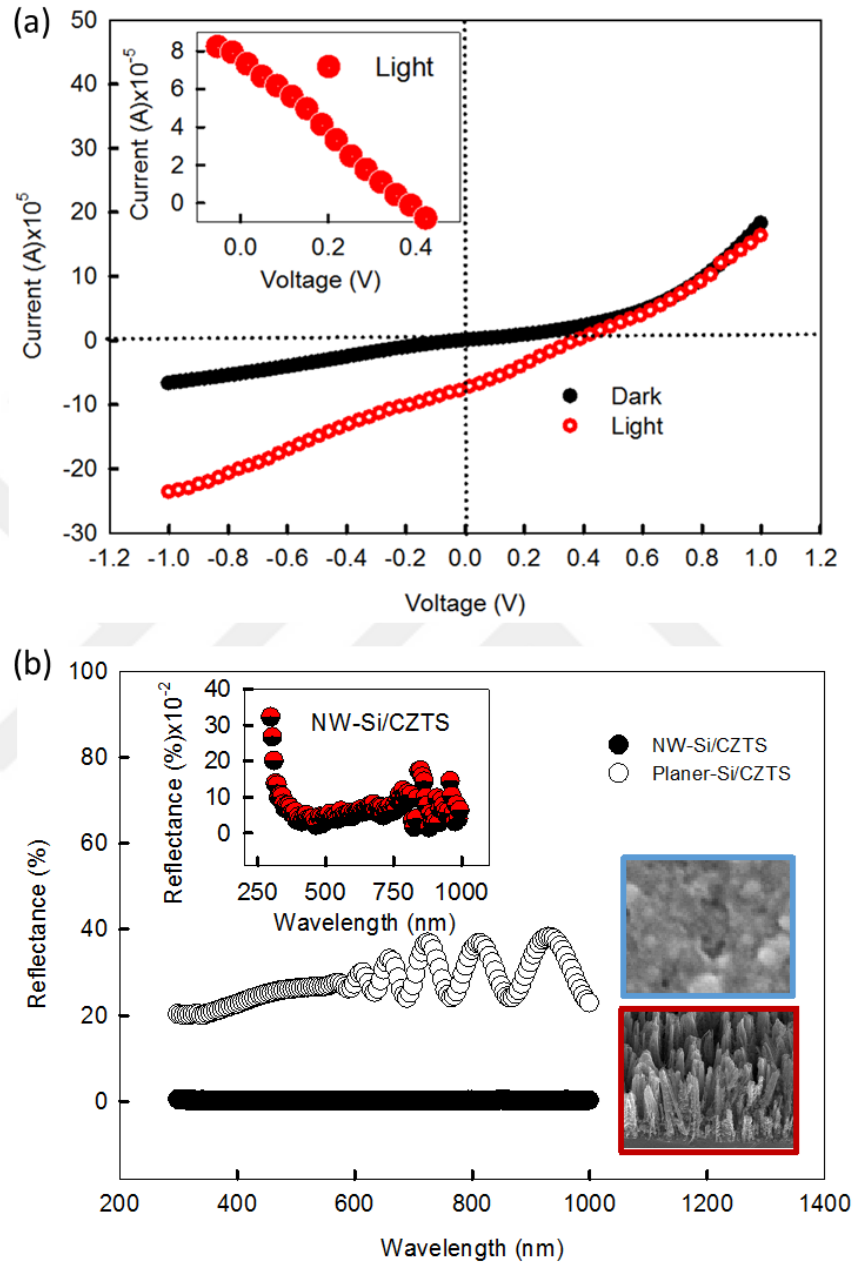


Figure 4.5 : (a) The current (I) - voltage (V) characteristic of the fabricated n-Si-NWs/p-CZTS solar cell measured under both dark and AM 1.5G illumination. The inset figure presents the same characteristic shifted into the first quadrant. (b) Reflectance spectra recorded from the fabricated NW based solar cell and its planer counterpart. The zoomed-in reflectance spectrum of the device structure with NW configuration is shown as an inset figure. The SEM micrographs recorded for both device configurations are also given as inset images.

The performance of fabricated n-Si-NWs/p-CZTS structured solar cell was measured under an AM 1.5 illumination (100 mW/cm^2). The current (I)-voltage (V) characteristic of a typical constructed device when it is exposed to the AM 1.5 illumination through the dot-patterned top contacts (Ag) is shown in Figure 4.5 (a), utilized to determine solar cell parameters including open circuit voltage (V_{oc}), short circuit current (I_{sc}), fill factor (FF) and power conversion efficiency (η). Energy conversion efficiency (η) of a solar cell is calculated by:

$$\eta = \frac{V_{oc}I_{sc}FF}{P_{in}} \quad (4.3)$$

in which P_{in} is incident power. The performance of the fabricated twenty cells were tested and the V_{oc} , J_{sc} (short circuit current density), FF and η parameters were calculated to be $0.40 \pm 0.01\text{V}$, $9.60 \pm 0.20 \text{ mA/cm}^2$, $26 \pm 1 \%$ and $1.0 \pm 0.2 \%$, respectively. These are the first results associated with n-Si-NWs/p-CZTS configured solar cell; therefore, it is not possible to compare with those reported in literature. However, in comparison with conventional planer CZTS and CIGS based thin film solar cells (typically over 20 %), it is clear that the achieved power conversion efficiency ($\sim 1 \%$) is relatively low. It is very important at this point to note that these are only preliminary results and an experimental systematic study on optimization of device structure and its component materials is required to improve the power conversion efficiency of the solar cell. Up to now, to our knowledge, very few studies are available in the literature that report the photovoltaic performance of planer counterpart of n-Si-NWs/p-CZTS investigated in the present study [117-119]. Among them, Song et al [118] studied the photovoltaic behavior of Ag/n-Si/p-CZTS/Au planer solar cell fabricated by growing a CZTS epitaxial layer on Si (111) substrate using molecular beam epitaxy (MBE). The V_{oc} and J_{sc} solar parameters associated with that solar cell were reported to be 0.12 V and 0.138 mA/cm^2 , respectively, which are less than the values accomplished with NW based solar cell configuration in the present study. In another study, the highest power conversion efficiency accomplished so far was reported for a solar cell with Mo/p-CZTS/n-Si/Al planer heterojunction architecture, which was fabricated by deposition of spin-coating CZTS layer on an n-type Si wafer and then annealing at $350 \text{ }^\circ\text{C}$ in thiourea for sulfurization process [119]. The corresponding parameters of the solar cell such as V_{oc} , and J_{sc} , and η were found to be 0.52 V, 3.28 mA/cm^2 and 1.13 %, respectively. Even the power conversion efficiency of the device is slightly higher than that of measured in the present study, it

is not the case for the J_{sc} , which is well below the one achieved with NW based device configuration ($9.60 \pm 0.20 \text{ mA/cm}^2$), demonstrating a ~ 3 -fold lower short-circuit current density. The higher J_{sc} with NW configuration compared with its planer counterpart can be attributed to unique features of NWs, led to low reflection losses, enhanced charge collection and large surface-to-volume ratio. Figure 4.5 (b) shows the reflectance spectra of CZTS thin film deposited on Si NWs and planar-Si wafer in the 300-1000 nm wavelength range. It can be seen from the inset figure that the reflectance for the Si-NWs decorated with CZTS over the measured wavelength range is lying between 0.01 % and 0.3 %. In comparison, the CZTS thin film deposited on planer Si-wafer exhibits a quite high reflectance, from 20 % to 40 %, for the same wavelength region. Compared to its planer counterpart, therefore, the measured higher J_{sc} in the present study can be attributed to the observed ultra-low reflectance of solar cell with NW configuration. There is no doubt that more efficient solar cells based on Si NWs can be realized by addressing several issues associated with both shell-layer and core-material in the core-shell device architecture. In other words, nanowire architecture (i.e., density, aspect ratio, orientation etc.), surface defects arising from large surface to volume ratio, thin film quality in term of electrical, structural and optical properties, and contact quality are among the most important factors that determine the performance of this type solar cells and they can be tuned for the realization of high efficient core-shell solar cells. It is known that the power conversion efficiency of the first core-shell solar cell reported in literature was consisted of thin amorphous n-Si on p-Si NWs and exhibited only $\sim 0.1 \%$ power conversion efficiency [46]. In that study, the low energy conversion efficiency was attributed to both junction quality and impurities. In another study, a core-shell solar cell based on Si NWs using two-step procedure was reported by Garnett and Yang [6]. They realized the core-shell structure by decoration of electroless-etched n-Si NWs with a p-type Si layer via chemical vapor deposition, which exhibited a 0.46 % energy conversion efficiency. The low conversion efficiency of the solar cell was ascribed to the interfacial recombinations and high series resistance, which was suggested to be overcome by surface passivation of Si NWs and lowering the bulk resistivity of p-Si shell layer. All the problems associated with core-shell solar cell device structure are solvable. For instance, from the previous studies we know that surface passivation to eliminate the surface defects alone would increase the energy conversion efficiency significantly [120]. Currently, based on all these considerations, our ongoing research has focused on optimization of

device structure by tuning nanowire geometry, employing surface passivation and producing high quality CZTS thin films to improve the performance of n-Si-NWs/p-CZTS structured solar cell over the energy conversion efficiency of ~ 1.0 % achieved in the present study.

4.4 Conclusions

In the present study, an attempt was made to fabricate a solar cell that combine the efficiency of 1st generation of solar cell with the benefits of 3rd generation solar cells. A prototype of n-Si-NWs/p-CZTS structured solar cell, therefore, with an efficiency of ~1.0 % was fabricated through the decoration of electroless-etched Si-NWs with a sol-gel derived monophase CZTS absorber layer. The constructed solar cell exhibited superior short circuit current density compared with its previously reported planer counterparts, which is very crucial for the realization of low cost high-efficient third generation solar cells in the future. On the basis of the promising findings presented in this paper, work on the remaining issues such as tuning nanowire geometry and improving CZTS thin film quality is continuing and will be presented in future studies.

5. CHARACTERIZATION OF ONE-STEP DEPOSITED $\text{Cu}_2\text{ZnSnS}_4$ THIN FILMS DERIVED FROM A SINGLE CRYSTALLINE POWDER⁴

5.1 Introduction

Today, it is a well-known fact that the world photovoltaic (PV) market is still dominated by silicon (Si) material due to its abundance in the Earth's crust (~25 %), mature and advanced technology, non-toxic nature, and high energy conversion efficiency [121]. Despite these benefits, increasing the efficiency of Si solar cells above 20% requires high quality single crystalline Si materials that increase the cost tremendously. To solve this issue, therefore, research on the realization of low cost high efficient thin film based solar cells has become very popular in recent years [122]. $\text{CuIn}_x\text{Ga}_{1-x}\text{Se}_2$ (CIGS) thin film solar cells, for instance, have already exceeded power conversion efficiencies over 20% [123]. In particular, the focus of recent research has been on fabrication of $\text{Cu}_2\text{ZnSnS}_4$ (CZTS) thin film solar cells, which offers significant advantages over the well-known materials (CIGS and CdTe) based thin film solar cells in term of the availability in the Earth's crust (Cu:50 ppm, Zn:75 ppm, Sn:2.2 ppm, S:260 ppm), the cost and toxic nature of their constituent elements [124]. The quaternary kesterite CZTS, consisted of earth-abundant and environmentally benign constituent elements relative to those present in CIGS, has emerged as a potential photo-absorber material due to their superior physical and chemical properties [125]. It has a direct band gap (1.4-1.5 eV) and high optical absorption coefficient ($> 10^4 \text{ cm}^{-1}$), optimum optical parameters for the realization of high efficient thin film solar cells. So far a variety of deposition techniques have been proposed for the fabrication of CZTS thin films such as co-evaporation, sol-gel, electron-beam and sputtering [13,41,107,126]. Based on the results obtained from the aforementioned CZTS thin film deposition techniques, it was clearly revealed that it is not easy to grow mono-phase kesterite CZTS phase due to the observed significant deviations from the

⁴ This chapter has been published in Renewable Energy. Peksu, E., Terlemozoglu, M., Parlak, M., Karaagac, H., (2019), Characterization of One-Step Deposited $\text{Cu}_2\text{ZnSnS}_4$ Thin Films Derived From A Single Crystalline Powder, Renewable Energy, 143, 1133-1142, doi: 10.1016/j.renene.2019.05.076.

stoichiometry of the film during the deposition cycle [127]. In the present work, a fabrication process based on a combination of single crystal growth by Bridgman technique and thin film deposition by electron-beam was used as a response to the problems associated with the CZTS thin film fabrication with techniques reported so far in literature. To the best of our knowledge, this is the first study presenting the characterization results of CZTS thin films prepared by one-step process with Cu-deficient composition using e-beam technique without applying a post-production step of sulphurization. Although several studies have been reported on the growth of CZTS single crystals [128], little attention has been given to using the powder extracted from the single crystal ingot as an evaporation source to grow mono phase CZTS thin films, which is expected to provide a stoichiometric film composition by preventing the sequential evaporation of constituent elements due to their different vapor pressures. In addition to this, even though a considerable amount of literature has been published on characterization of CZTS thin films, it is not the case for the CZTS single crystals, which is crucial for understanding the fundamental properties of the compound and fabrication of high-efficiency solar cells. Therefore, the present study also aims to fill this gap in the literature by investigating the electrical, structural and optical properties of Bridgman-grown CZTS single crystals.

5.2 Experimental

For the growth of CZTS single crystals by vertical Bridgman technique, polycrystalline state of the compound was first obtained by sintering process. The sintering process is based on reaction of highly pure constituent elements at a temperature above their melting point in a sealed quartz crucible under a vacuum. For sintering process, therefore, highly pure raw materials Cu (6N), Zn (6N), Sn (6N) and S (6N) with different stoichiometries (Cu-poor and Cu-rich) were sealed under vacuum of about 2×10^{-6} Torr in quartz crucibles (1 cm in diameter and 30 cm in length and with cone-shape bottom) and synthesized in a special designed horizontal furnace (Lindberg) at above the melting point of the constituent elements (1050 °C) for 48 h. After sintering process, the prepared crucible was placed into a Crystalox MSD-4000 model three zone vertical Bridgman-Stockbarger system for the growth of CZTS single crystals. A suitable temperature profile was used to grow single crystals by setting the temperature of upper, middle and lower zones to 1100, 900 and 600 °C,

respectively with a withdrawal rate of 1 mm/h. Once the solidification was completed, the crucible was slowly cooled down to room temperature to minimize the thermal stress. Following that, the ingot was removed from the crucible and subsequently cut into small cylindrical pieces with dimensions 5x10x10 mm³. In the end, the extracted pieces were mechanically polished for the physical measurements. The powder extracted from the grown ingot was also used as an evaporation source for the fabrication of CZTS thin films using electron-beam technique.

The CZTS thin films were grown on soda lime glass substrates by e-beam evaporation of the powder extracted from the single crystal, which is placed into a graphite crucible and situated 15 cm below the sample holder. During the evaporation process the base pressure, substrate temperature and evaporation rate were 5x10⁻⁶ Torr, 150 °C and 5 Å/s, respectively. The thickness of the film was controlled in situ by an inficon XTM/2 thickness monitor and confirmed subsequently by a Veeco DEKTAK 150 surface profilometer following the deposition cycle, which was found to be around 600 nm.

In order to investigate the effect of heat treatment on structural, electrical and optical properties of the deposited films, the post-annealing process between 250 °C and 500 °C was applied to them under N₂ gas flow for 30 min. For electrical measurements, the films were produced with van der Pauw geometry, the ohmic contacts of which were made through the deposition of indium (In) by thermal evaporation.

The Hall and photo-conductivity measurements of single crystal samples were carried out through attaching copper electrodes to the ohmic In contacts made onto the crystal surfaces via Nanomagnetics Hall Effect system at a magnetic field strength of 0.9 T. To determine the structural properties of samples, X-ray diffraction (XRD, GBC-MMA with λ : 0.154 nm CuK α radiation source) and Raman scattering (Horiba-Jobin Yvon iHR550, an excitation wavelength of 532 nm) measurements were conducted. Atomic force microscope (AFM, Shimadzu 9500J3), Scanning electron microscope (SEM, Hitachi S-4100 FE) equipped with energy dispersive X-ray analysis (EDXA) was used for the purpose of revealing the morphological properties and chemical composition of the samples.

Transmission measurements in the wavelength range 400 nm-1000 nm were performed in order to understand the optical properties of the samples by using Aquila NKD-7000 V Spectrophotometer System.

5.3 Results and Discussion

5.3.1 $\text{Cu}_2\text{ZnSnS}_4$ (CZTS) crystal

5.3.1.1 Structural analysis

The elemental composition of the CZTS single crystal prepared with Cu-poor content was determined by EDXA measurements. The recorded SEM image of a piece of CZTS crystal ingot and the photograph of a sliced wafers from the grown ingot (L:23 mm, dia:13 mm) are given in Figure 5.1.

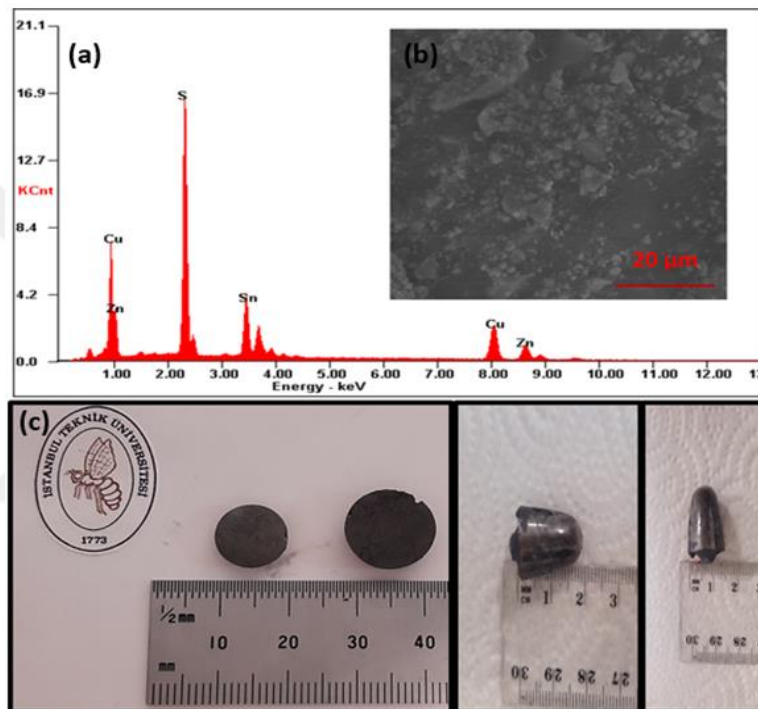


Figure 5.1 : (a) EDXA spectrum and (b) top-view SEM image recorded for the obtained CZTS powder. (c) Pictures of sliced wafers of the grown CZTS ingot.

As can be clearly seen from the spectrum, the relevant peaks of all the expected constituent elements in the structure were observed. The calculated atomic ratios of elements and atomic percentages of the content elements are given in Table 5.1. It is clear from the table that the elemental composition of the grown crystal is off-stoichiometry. In other words, the crystal has a Cu-poor and Zn-rich composition with the calculated $\text{Cu}/(\text{Zn} + \text{Sn}) = 0.98$ and $\text{Zn}/\text{Sn} = 1.05$ atomic ratios.

It is a well-known fact that the high efficiency CZTS thin film based solar cells are achieved with a Cu-poor and Zn-rich chemical composition [129].

Table 5.1 : Atomic ratios and percentages of the content elements for CZTS crystals prepared with Cu-poor and Zn-rich content.

Element	Cu	Zn	Sn	S	$\frac{\text{Cu}}{\text{Zn} + \text{Sn}}$	$\frac{\text{S}}{\text{Cu} + \text{Zn} + \text{Sn}}$	$\frac{\text{Zn}}{\text{Sn}}$
At %	24.30	12.62	12.06	51.01	0.98	1.04	1.05

The main reason for demanding the production of CZTS compounds with Cu-poor and Zn-rich content is to prevent the generation of defect and defect clusters ($\text{Cu}_{\text{Zn}} + \text{Sn}_{\text{Zn}}$) and/or ($2\text{Cu}_{\text{Zn}} + \text{Sn}_{\text{Zn}}$) with harmful and high activation energies, which are possible in the structure of CZTS compound grown with Cu-rich and Zn-poor content [130]. The structural properties of the CZTS crystals were examined through X-Ray diffraction (XRD) measurements conducted in the 2θ range of 10° to 80° with a scan rate of $2^\circ/\text{min}$. XRD pattern recorded for a piece of CZTS crystal ingot prepared with a Cu-deficient content is present in Figure 5.2 a.

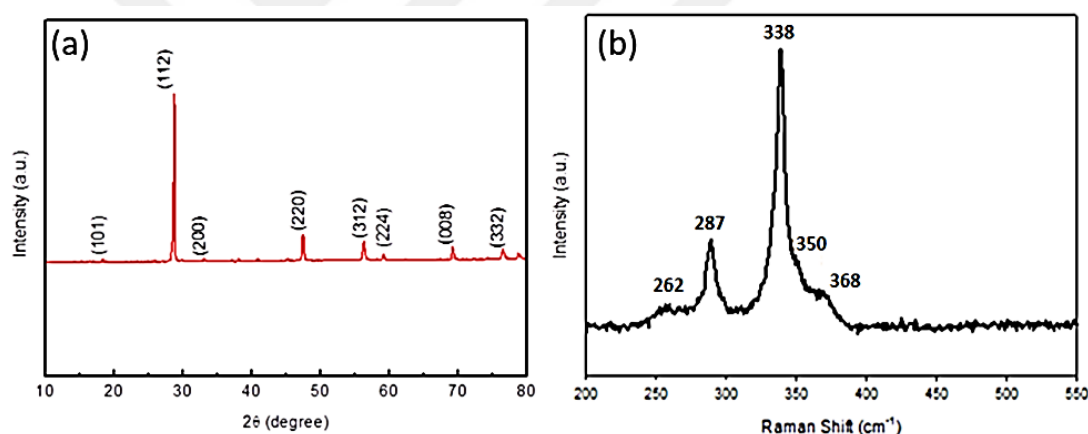


Figure 5.2 : (a) X-Ray diffraction pattern and (b) Raman spectrum recorded for a CZTS crystal prepared with a Cu-poor content.

As can be seen from the XRD pattern, diffraction peaks are identified with certain reflection planes. Following the comparison of the recorded spectra with the ICDD cards in database it was found that the resolved peaks are associated with monophasic kesterite CZTS phase (card no: 026-0575). Before the formation CZTS phase, double and triple phases are formed with a rather high probability the structure of which, such as ZnS, is very similar to that of CZTS compound. Therefore, it is impossible to distinguish these phases by using only XRD analysis. Raman analysis is also required to detect the secondary phases and confirm the formation of monophasic CZTS. Raman spectrum provides an information about the vibrational properties of crystalline samples. Therefore, it is a strong tool to investigate the presence of double and triple

phases in ternary and quaternary compounds. Figure 5.2 b presents the Raman scattering spectrum recorded for CZTS crystal. As can be seen from the figure, peaks located at 262, 287, 338, 350 and 368 cm^{-1} can be clearly resolved from the spectrum. These peaks are in good agreement with those previously reported in the literature, which belong to the kesterite structure of CZTS [131]. The dominant peaks located at 338 and 287 cm^{-1} are known to be stemming from A1 mode, as a result of the vibration of S in the CZTS structure. The peak located at 368 cm^{-1} belongs to the B1 oscillation mode, which arises from the vibrations of cations only in the z-direction [131]. Based on the combined analyses of XRD and Raman spectroscopy, the presence of monophasic CZTS with kesterite structure is proven.

5.3.1.2 Hall and photoconductivity measurements

For the Hall effect and photoconductivity measurements, 5 mm thick CZTS crystal samples (10 mm in diameter) were prepared in the van der Pauw geometry. Prior to performing conductivity measurement, the conduction characteristics of prepared sample was determined by hot probe and found to be p-type. Temperature-dependent (100-350 K) conductivity (σ) measurements were initially performed under dark conditions (Figure 5.3). It can be seen from the Figure 5.3 that the conductivity increases with increasing temperature, indicating that the grown crystal behaves as semiconductor material. In addition, it is clear from the resulting curve, $\ln\sigma$ versus $1000/T$ graph reveals 3 distinct temperature zones. Each of these linear temperature zones represents different temperature-activated current mechanisms. In other words, it shows that there are 3 acceptor levels with different activation energies. Activation energies associated with 100-150K, 180-220K, 250-340K temperature regions were revealed by the Arrhenius equation and were calculated to be ~ 1, 5 and 30 meV, respectively. In the literature, the activation energy for Cu_{Zn} anti-sites point defects in CZTS crystal was determined as 110 meV [132]. This value is considerably higher than those values (1-30 meV) found in the present study. Energy levels with low activation energy are generally attributed to presence of V_{Cu} (copper vacancy) point defects in the kesterite structure [133]. The acceptor levels associated with Cu_{Zn} and V_{Cu} point defects are known to be responsible for the p-type character of the CZTS compound. In terms of formation energies, the Cu_{Zn} level is more likely to be present in the structure owing to the fact that the value of the Cu_{Zn} level is lower than that of V_{Cu} .

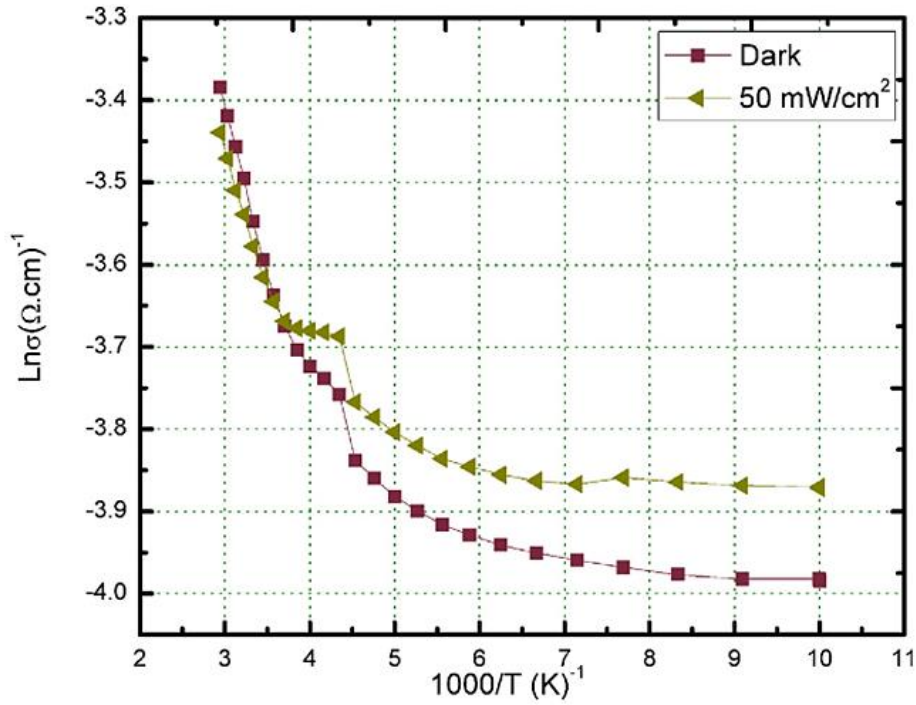


Figure 5.3 : Temperature dependent conductivity of CZTS crystals performed under dark and illumination (50 mW/ cm²) conditions.

But in some cases, depending on the stoichiometry of the compound, both types of structures can be found together [132]. Cu-poor CZTS composition grown in the present study may have led to the formation of V_{Cu} levels. In addition to measuring the conductivity under dark condition, it was also examined a halogen lamp illumination (~ 50 mW/ cm²) in order to measure the sensitivity of the grown Cu-poor CZTS crystals to a light in the visible range. As can be seen from the curve provided in Figure 5.3, in the low temperature range the conductivity increases with respect to that of measured under illumination, which is not the case at higher temperatures. Namely, no noticeable difference is detected between dark and light conditions at high temperature zone. This behavior may stem from that the thermally generated carriers are dominating photo-generated ones as a source of the current at high temperature.

To determine the electrical properties of the grown crystal in more detail, Hall Effect measurements were also carried out as a function of temperature in the 240-360 K range. Extremely important parameters such as carrier concentration, resistivity, mobility and conductivity character were calculated were determined from these measurements, which are summarized in Table 5.2.

Table 5.2 : Calculated conductivity parameters from Hall measurement for Cu-poor CZTS crystal.

Temperature (K)	Hole Concentration (cm ⁻³)	Resistivity (Ω.cm)	Mobility (cm ² /V.s)
240	3.34x10 ¹⁷	4.39	4.26
260	6.76x10 ¹⁷	4.70	1.97
280	5.11x10 ¹⁷	4.31	2.83
300	1.05x10 ¹⁸	3.91	1.52
320	9.71x10 ¹⁷	3.54	1.82
340	1.16x10 ¹⁸	3.20	1.69
360	7.13x10 ¹⁸	2.88	3.04

As it can be seen from the table, hole concentration, resistivity, mobility and conductivity character were found to be $1.05 \times 10^{18} \text{ cm}^{-3}$, $3.91 \text{ } \Omega \cdot \text{cm}$, $1.52 \text{ cm}^2/\text{V.s}$, and p-type, respectively at room temperature. In the literature, the respective values were reported to be 1.4×10^{16} - $1.6 \times 10^{17} \text{ cm}^{-3}$, 51 - $135 \text{ } \Omega \cdot \text{cm}$, 15 - $35 \text{ cm}^2/\text{V.s}$ and p-type for CZTS crystal grown by THM [132], which are different from those measured in the present study. This difference is a quite normal due to the fact that both crystals have different stoichiometry and different crystal quality. It is apparent from these values that in terms of electrical properties, CZTS crystal with Cu-poor, Zn-rich content exhibits acceptable electrical properties that are required for a material to be employed as an absorber layer for the production of high-efficiency CZTS-based solar cells.

5.3.2 Cu₂ZnSnS₄ (CZTS) thin films

5.3.2.1 Structural analysis

Following the optimization of Bridgman grown Cu-poor and Zn-rich CZTS crystals, a specific amount of powder extracted from the grown ingot was used as starting material for the single-step deposition of CZTS thin films on soda lime glass substrate by electron-beam evaporation. A typical EDXA spectrum recorded for the CZTS annealed at 500 °C is presented in Figure 5.4. The measured atomic percentages of the constituent elemental for the 600 nm thick CZTS film as-grown and annealed at different temperatures for 30 min are summarized in Table 5.3. It is clear from the table that the deposited CZTS thin films have an Cu-poor and Zn-rich chemical composition, very close to that measured for the Cu-deficient powder used as an evaporation source. In other words, the atomic percentage of Cu and Zn and Cu/(Zn + Sn) ratio were found to be 24.21 %, 14.14 % and 0.99, respectively for the as-grown sample. The respective values for a stoichiometric CZTS compound are 25.00 %, 14.14 %, and 0.99, respectively.

12.50 % and 1.00. Therefore, there is a slightly Cu- deficient and Zn-rich chemical composition for the deposited CZTS thin films.

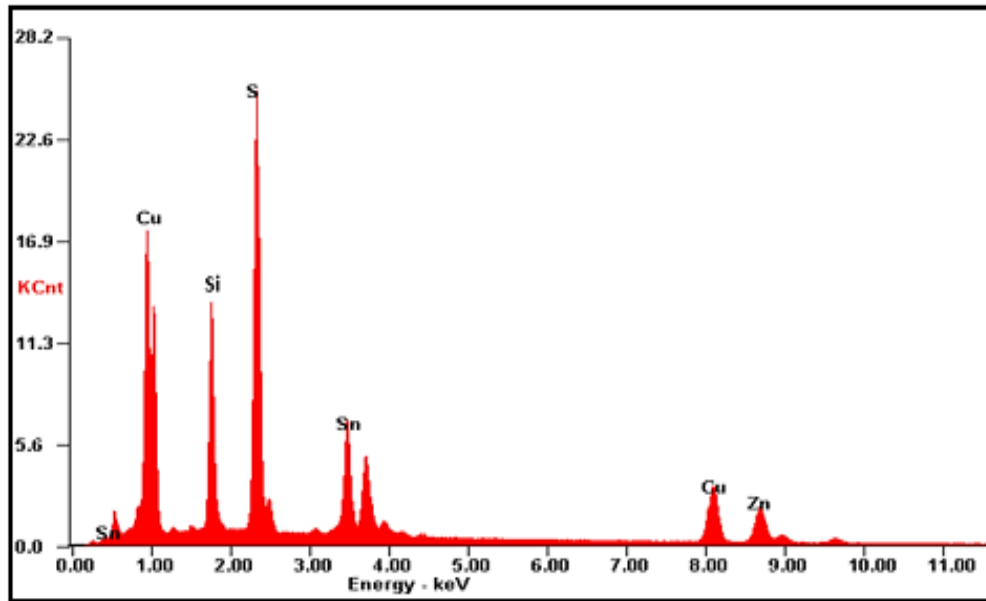


Figure 5.4 : A typical EDXA spectra recorded for CZTS thin films (annealed at 500 °C) deposited on soda lime glass substrates.

It is also obvious from the EDXA results that there is no notable change in atomic percentages of the constituent elements with increasing annealing temperature except a slight decrease in amount of volatile sulphur.

Table 5.3 : Atomic percentages and ratios of the content elements for 600 nm thick CZTS films prepared with Cu-poor and Zn-rich.

Element (%)	Cu	Zn	Sn	S	Cu/(Zn+Sn)
As-grown	24.21	14.44	10.11	51.24	0.99
250 °C	24.08	14.38	10.69	50.85	0.96
350 °C	23.92	14.10	12.01	49.97	0.92
500 °C	23.86	14.00	12.82	49.32	0.89

The consistency of the composition of the CZTS film with that of starting material clearly demonstrates the success of e-beam technique for the fabrication of CZTS thin film via one-step deposition.

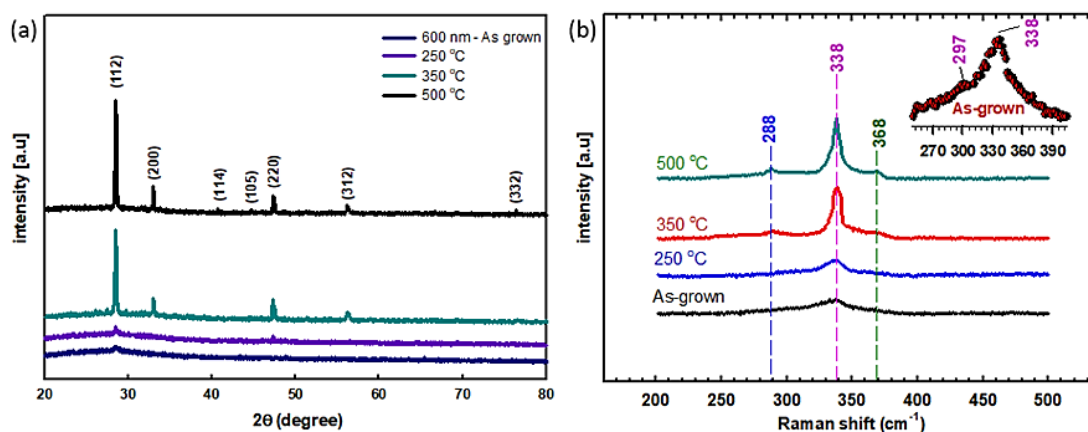


Figure 5.5 : (a) The XRD patterns and (b) Raman spectra recorded for as-grown and annealed (250 °C, 350 °C and 500 °C) CZTS films. Inset figure in part (b) represents the zoomed in version of Raman spectrum recorded for the as-grown CZTS thin film.

In order to reveal the effect of annealing on structural properties of CZTS thin films, they were annealed in the temperature range of room temperature - 500 °C under N₂ gas flow for 30 min. X-Ray diffraction patterns and Raman spectra recorded for as-grown and annealed CZTS thin films are presented in Figure 5.5 a and b, respectively. XRD measurements were carried out in the range from 2θ : 20° to 80° with a step size of 2°/min. Structural analysis has revealed that the as grown and the sample annealed at 250 °C CZTS films have a nearly amorphous matrix and then transform into a polycrystalline form with a kesterite phase after the post-annealing process at 500 °C. The diffraction peaks and 2θ values of as-grown and annealed films at different temperatures are summarized in Table 5.4.

Table 5.4 : XRD peak positions associated with the recorded values for the fabricated CZTS thin films and those provided by JCPDS reference cards.

Samples	Miller Indices						
	(112)	(200)	(114)	(105)	(220)	(312)	(332)
Card No: 026-0575	28.53	32.99	40.76	44.99	47.33	56.17	76.44
As-grown	28.44	-----	-----	-----	-----	-----	-----
350 °C	28.48	33.00	-----	-----	47.30	56.14	76.40
500 °C	28.52	33.02	40.74	44.86	47.32	56.16	76.42

As can be deduced from the table, (112), (200), (114), (105), (220), (312) and (332) diffraction peaks matches well with JCPDS card no 026-0575. From the XRD patterns it was observed that there was no reflecting peaks corresponding to binary or ternary secondary phases of CZTS compound. The peak position of (112) main diffraction peak was found to be located at 28.44° for as-grown films whereas it slightly shifted to

28.52° upon annealing at 500 °C. It is known that compressive stress induces the peak shifting [134] towards higher angles at high annealing temperatures. In addition, it can be seen from the XRD pattern that there is a clear trend of an increase in peak intensities and a decrease in full width at half maxima (FWHM) with increasing the annealing temperature, which suggests an increase in the grain size and an enhancement in crystallinity of the CZTS thin films subjected to a post-annealing treatment. FWHMs of (112) main diffraction peak were found to be 0.41° and 0.197° for CZTS thin films annealed at 350 °C and 500 °C, respectively. Scherrer formula was used to calculate the particle size [135];

$$D = \frac{0.9\lambda}{\beta \cos \theta} \quad (5.1)$$

where λ : 0.154056 nm, β is full width at half maximum of diffraction peak in radian, and θ is half of Bragg diffraction angle (2θ). The average grain sizes were calculated to be 21 nm and 44 nm for the CZTS films annealed 350 °C and 500 °C, respectively, suggesting the formation of larger grains for the CZTS thin films annealed at higher temperatures. Figure 5.5 b shows the recorded Raman spectrum (with 532 nm excitation wavelength) for CZTS films annealed between room temperature and at 500 °C. From the Raman spectrum above, we can see that for the annealing temperatures over 250 °C in all spectra the strongest peak is located at 338 cm⁻¹ and the other two weaker peaks are at 288 and 368 cm⁻¹. As mentioned earlier in the text, these peaks match well with those previously reported in the literature for the same material [136]. The main peak located at 338 cm⁻¹ is arising from the vibrations of sulphur atoms [137]. These three peaks in the Raman spectrum can be taken as a clear indication of the presence of single phase kesterite CZTS phase for the annealing temperatures over 250 °C and support the findings of XRD analysis. On the other hand, for the low annealing temperatures (as-grown and 250 °C) in addition to the peaks observed at higher annealing temperatures, an additional one located at 297 cm⁻¹ was detected as shown in Figure 5.5 b as an inset plot, demonstrating a zoomed in version of Raman spectrum recorded for the as-grown CZTS thin film. The resolved peak at this location is known to be associated with highly conductive Cu₂SnS₃ (CTS) ternary phase as reported earlier in the literature [138,139]. It is clear from the Figure 5.5 b that this secondary phase gradually disappears and there is an increase in intensity of the resolved peaks with increasing annealing temperature. The observed increase in intensity with the increase in annealing temperature indicates a gradual improvement

in the crystallinity of the deposited films. Based on the combined results extracted from XRD and Raman spectroscopy, it can now be claimed that there is a single phase CZTS kesterite structure formed at 500 °C annealing temperature.

5.3.2.2 Morphological analysis

Following the structural analysis, morphological properties of as-grown and annealed CZTS thin films deposited on SLG substrates were also examined through AFM measurements. The results obtained from morphological (AFM) analysis revealed that heat treatment has a significant impact on determining the morphology of the fabricated CZTS films. Figure 5.6 presents the images obtained from the AFM measurements in the tapping mode. The scanning area for all two dimensional AFM images is 5 μ m x 5 μ m. From the image in Figure 5.6 a, it is apparent that as-grown CZTS thin film is consisted of small grains distributed homogenously throughout the substrate. The average grain size and RMS value for the as-grown film are measured to be 0.1 μ m and 9.814 nm, respectively. At low temperatures, the kinetic energy is known to be insufficient for the agglomeration of grains [140]. Therefore, it is expected that the grain size on the surface would be too small for as-grown films. Elevating the annealing temperature will increase kinetic energy and provide the required threshold diffusion energy [141], which subsequently trigger the agglomeration of small grains. The formation of larger clusters with increasing annealing temperature causes the observed increment in surface roughness. It can be observed from Figure 5.6 (b) that there is an increase in grain size when the annealing temperature increased from room temperature to 250 °C. Figure 5.6 (e) and (f) illustrates the recorded 2-D AFM image and profile analysis of the CZTS films annealed at 500 °C, respectively to determine the particle size. The average grain size of the film annealed 500 °C was calculated as 0.73 μ m, whereas it was found to be 0.1 μ m for the as-grown film. In other words, when the CZTS thin films are subject to heat treatment, it triggers a significant enhancement in particle size of the grains. Although this situation is related to the grains on the surface, it is still in good agreement with those extracted from XRD study and suggest an increase in the particle size and degree of crystallization following the post-annealing process. Figure 5.6 also shows that annealing process has a pronounceable effect on determining the surface roughness's of the films.

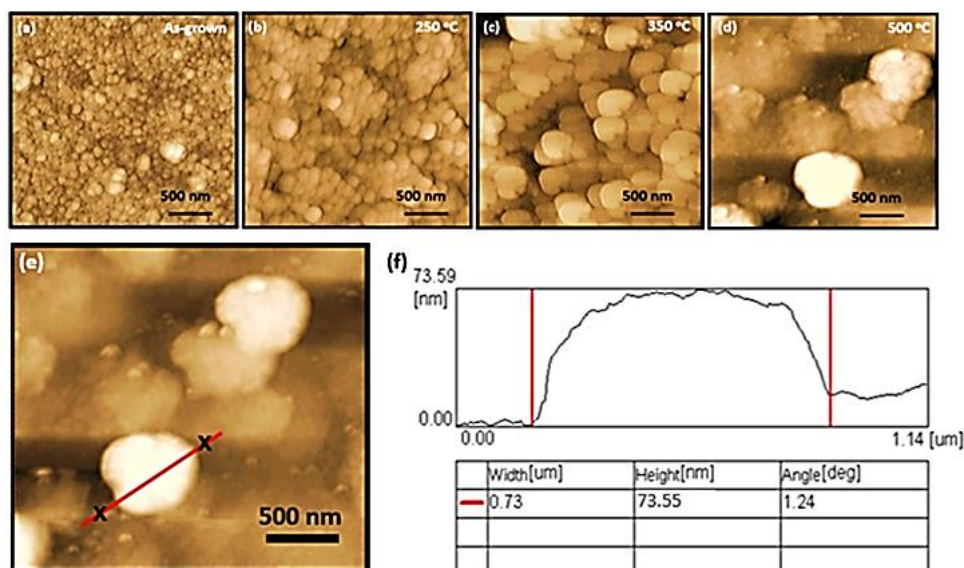


Figure 5.6 : AFM images recorded for CZTS thin films: (a) as-grown, and annealed at (b) 250 °C, (c) 350 °C, and (d) 500 °C. (e,f) Particle size analysis for CZTS film annealed 500 °C.

RMS values were found to be 81.988 nm, 117.278 nm and 278.296 nm for CZTS films annealed at 250 °C, 350 °C and 500 °C, respectively.

5.3.2.3 Optical analysis

In Figure 5.7, the optical reflectance and transmittance measurements in the wavelength range of 400-1000 nm, for as-grown and annealed CZTS thin films deposited onto soda-lime glass substrates were presented. It is clear from the reflectance spectrum that the reflectance value is approximately 30 % for as-grown films in the visible region, whereas this value reduces to 10 % upon annealing at 500 °C. These behavior is consistent with that reported in the literature for the same compound [142]. Results showed that the transparency of CZTS thin film is around 40 % for as-grown film, it has the lowest value for the film annealed at 500 °C. With increasing the annealing temperature, it is seen that the absorption edge shifts towards higher wavelengths. Shifting towards higher wavelengths means that the band gap shifts to small energy values. The observed reduction in band gap energy may stem from the revealed increase in grains size or the expected decrease in grain boundaries with increasing annealing temperature [143]. The energy band gap values of the CZTS thin films are known to be varying from 1.4 eV to 1.5 eV [144]. The energy band gaps were calculated for as-grown and annealed CZTS thin films by means of the recorded transmittance and reflectance spectra.

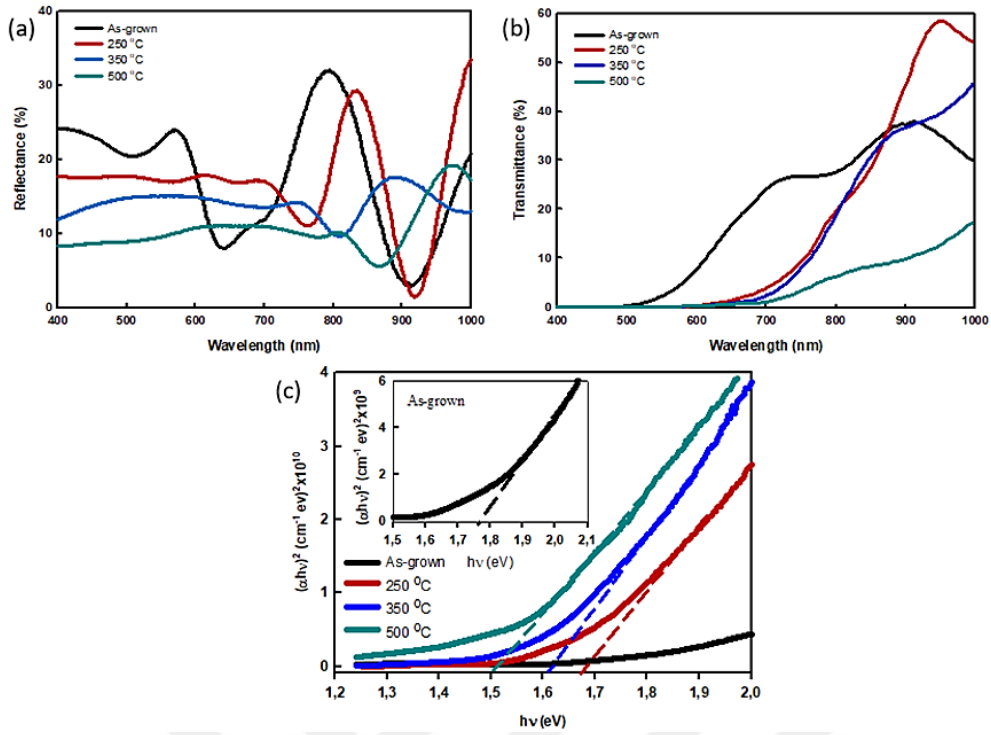


Figure 5.7 : (a) Reflectance and (b) transmittance spectra for as-grown and annealed CZTS thin films. (c) The optic band gap determination through the relation between the photon energy and absorption coefficient.

The absorption coefficient (α) was calculated through the following expression [142];

$$\alpha = \frac{1}{d} \ln \frac{(1-R)^2}{T} \quad (5.2)$$

where d is the thickness of the film, T and R are standing for transmittance and reflectance, respectively. After calculating the absorption coefficients, to determine the band gap energies of the films the absorption coefficient vs photon energy graphs were plotted as shown in Figure 5.7 c. The intersection of linear region on the photon energy (at $\alpha=0$) gives the optical band gap energy of the material. The calculated band gaps for the samples annealed at different temperatures are summarized in Table 5.5.

Table 5.5 : The calculated band gaps for the CZTS samples annealed at different temperatures.

Sample	Band Gap (E_g)
As-grown	1.76 eV
250 °C	1.67 eV
350 °C	1.61 eV
500 °C	1.50 eV

As can be seen from the Figure 5.7 c, the band gap energy decreases from 1.76 eV to 1.50 eV as the annealing temperature increases from the room temperature to 500 °C.

The elimination of the detected secondary phase of CTS formed at the early stage of crystallization, the improvement in crystallinity, the change in the homogeneity and the increase in grain sizes (elimination of quantum effect) with increasing annealing temperature may be the reasons for the observed shift in band gap energy, as reported elsewhere [145-147]. The energy band gap of CZTS film annealed at 500 °C was calculated to be 1.50 eV, which is in good agreement with those reported in the literature [148].

5.3.2.4 Hall and photoconductivity measurements

In order to reveal the photo-electrical properties of CZTS thin films with best crystal quality (500 °C), conductivity measurements were performed in 100-400 K temperature range under both dark conduction and illumination (50 mW/ cm²) provided by a halogen lamp. The obtained variation was presented in Figure 5.8.

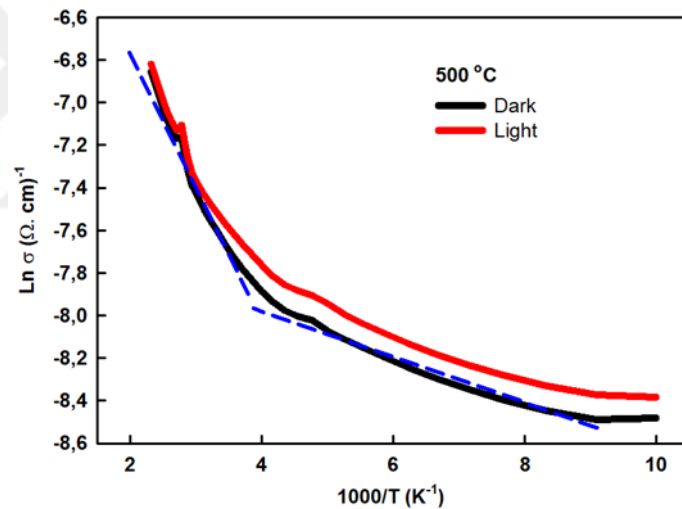


Figure 5.8 : Variation of electrical conductivity of CZTS films annealed at 500 °C measured in dark and under illumination (~ 50 mW/cm²) for the temperature range 100-400 K.

Conductivity measurements under dark condition revealed that there is an increment in conductivity with increasing temperature, which is a clear indication of that the fabricated films behave as semiconductor material. It is apparent from the figure that variation of $\text{Ln } \sigma - 1000/T$ reveals two linear regions, one of them is at low temperature (120-230 K) and the other is at high temperature (300-430 K) range. The presence of these regions indicates the existence of two types of current mechanisms which are activated at different temperature regions. Activation energies of these current

mechanisms in the range of 120-230 K and 300-430 K were calculated as $E_{a1} = 12$ meV and $E_{a2} = 60$ meV, respectively. It is deduced that these levels are associated with acceptor states due to the fact that the sample was predetermined by hot probe technique to be a p-type. In the literature, low activation energy levels (10-60 meV) in the kesterite CZTS structure is known to be originated from the copper-vacancies (V_{Cu}). Depending on the chemical composition (stoichiometry) of the fabricated CZTS thin films, Cu_{Zn} or V_{Cu} can be found predominantly in the kesterite structure. Cu-poor content may lead to the formation of V_{Cu} levels [149]. From the temperature dependent variation of conductivity measured under an illumination intensity of about 50 mW/cm², which is provided by a halogen lamp, it is clearly seen that the CZTS films coated on the glass substrate have a response to the visible light over the entire studied temperature range (Figure 5.8). While the resistivity in dark at room temperature was measured to be $\sim 2 \times 10^3 \Omega \cdot cm$, this value was found to be $\sim 1.8 \times 10^3 \Omega \cdot cm$ under illumination. This change clearly demonstrates the response of CZTS films to light.

Besides temperature-dependent conductivity measurements, temperature-dependent (100-400 K) Hall measurements were also performed to reveal the carrier concentration and mobility parameters. As the as-grown and the sample annealed at 250 °C had a metallic rich conductive surface, the ohmic contacts to the surface of the films made through the deposition of indium by thermal evaporation were shorted, which prevented the conductance of the Hall measurements. The metallic behavior of the sample may stem from the presence of highly conductive secondary phases such as CTS and $Cu_{2-x}S$ at the surface of the films at the early stage of crystallization. The resolved CTS secondary phase for the as-grown film supports this suggestion. The mobility-temperature and hole concentration-temperature graphs for the samples annealed at 350 °C and 500 °C obtained from the Hall measurements are presented in Figure 5.9 (a₁-a₂ and b₁-b₂) and (a₃ and b₃), respectively. From the Hall measurements the conductivity, hole concentration and mobility at room temperature were calculated to be $\sim 1.5 \times 10^{-4} (\Omega \cdot cm)^{-1}$, $1.1 \times 10^{15} cm^{-3}$ and $0.9 cm^2 / V \cdot s$, respectively for the films annealed at 350 °C. The respective values were found to be $\sim 5.1 \times 10^{-4} (\Omega \cdot cm)^{-1}$, $2.6 \times 10^{15} cm^{-3}$ and $1.22 cm^2 / V \cdot s$ for the sample annealed at 500 °C. Results clearly show that there is a significant improvement in conductivity when the annealing temperature is elevated from 350 °C to 500 °C. The observed increase in conductivity

with the increasing annealing temperature can be attributed to the improvement in crystallinity as revealed by XRD, Raman and AFM studies.

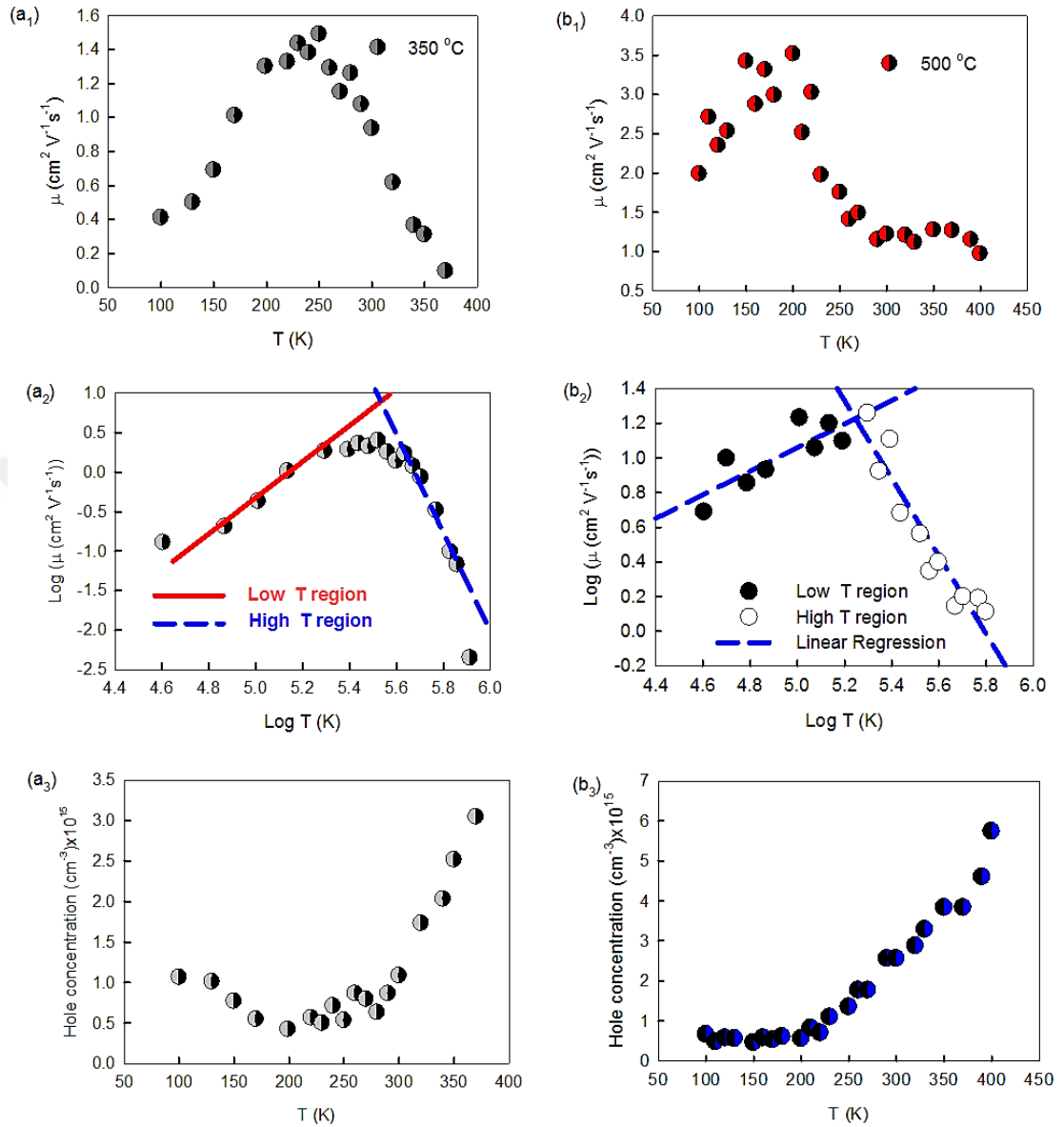


Figure 5.9 : Temperature dependent (a₁-a₂ and b₁-b₂) mobility and (a₃ and b₃) hole concentrations of CZTS thin films annealed at 350 °C and 500 °C obtained from Hall Effect measurements performed in the temperature range of 100-400 K.

The improvement in crystallinity results in the decrease in density of grain boundaries as well as the elimination of secondary phases, which are acting scattering centers. Therefore, the increase in both mobility and carrier concentration can be attributed to the increase in grain sizes and elimination of defects at high annealing temperatures.

It is reported in the literature that the hole concentration for the CZTS thin film is mostly in the range of 10¹⁶-10¹⁸ cm⁻³ [150,151], however, there are also many different

values reported to be out of this range [152,153]. In addition, mobility values in the range of 0.1-30 cm²/ V.s have been reported for the CZTS thin films [154]. The present findings seem to be consistent with the literature. The plots of Log (μ) versus Log (T) presented in Figure 5.9 (a₂ and b₂) shows that as temperature increases, the mobility first increases and then reaches a value of saturation in low temperature zone, as predicted by the theory. However, it starts to decrease systematically from the high saturation value in high temperature zone. This behavior shows that the impurity-originated scattering mechanism is the dominant process in the low temperature region, while the phonon-based scattering mechanism then start to be dominant one in the high temperature region.

5.4 Conclusion

Cu₂ZnSnS₄ (CZTS) single crystals were successfully grown by using vertical Bridgman technique. The energy dispersive X-ray analysis (EDXA) measurements revealed a Cu-poor and Zn-rich chemical composition of the grown single crystal, which is known to be very crucial for the realization of high efficient CZTS compound based solar cells. The formation of single phase CZTS single crystal with kesterite structure was proved by XRD and Raman spectroscopy. The electrical properties of Cu-poor and Zn-rich CZTS crystals were investigated by conducting temperature dependent Hall Effect measurements. Three distinct current mechanisms with activation energies between 1 meV and 30 meV were resolved from the conductivity versus temperature plot, identified to be associated with copper-vacancies (V_{Cu}). The room temperature resistivity, mobility and hole concentration values were found to be 3.91 Ω .cm, 1.52 (cm²/ V.s), and 1.05x10¹⁸ cm⁻³, respectively. A powder extracted from the grown CZTS single crystal ingots was employed as evaporation source for the one-step deposition of CZTS thin film using electron-beam technique. The fabricated thin films were found to have a Cu-poor and Zn-rich chemical composition (off-stoichiometry), which is desirable for the construction of high performance CZTS based thin film solar cells.

In order to reveal the effect of annealing on the morphological, structural, electrical and optical properties of CZTS thin films, they were annealed between room temperature and 500 °C under an inert gas flow. Structural analysis has revealed that while the as-grown CZTS films has an amorphous structure it is transform into a

polycrystalline monophase kesterite CZTS structure with (112) plane orientation upon annealing at 500 °C. The presence of single phase of kesterite CZTS structure without any secondary phases was also confirmed by resolving 262, 287, 338, 350 and 368 cm^{-1} peaks from the recorded Raman spectrum. Surface morphologies of the CZTS thin films were studied by SEM and AFM measurements. A significant increase in surface roughness of the films was observed as the annealing temperature increased from room temperature to 500 °C. The band gap was found to be 1.50 eV for the CZTS film annealed at 500 °C. A systematic decrease in band gap energy with increasing annealing energy was also observed.

Finally, the conducted photo-electrical measurements revealed that CZTS thin films have good sensitivity to the visible light, which is essential for an absorber layer in the solar cell device structure. In addition to this, from the Hall Effect measurements, the room temperature conductivity, mobility and hole concentration values were found to be $5.1 \times 10^{-4} (\Omega \cdot \text{cm})^{-1}$, $1.22 \text{ cm}^2 / \text{V} \cdot \text{s}$, and $2.6 \times 10^{15} \text{ cm}^{-3}$ for the film annealed at 500 °C, respectively.

5.5 Acknowledgements

This work was supported by Turkish Scientific and Research Council (TUBITAK) under Grant no 315M401.



6. CONCLUSIONS

The aim of this thesis was the synthesis of ZnO (zinc-oxide) and Si (silicon) NWs (nanowires) by solution based low cost and simple fabrication techniques and their integration into a new generation solar cell device architecture (core-shell) for the realization of low cost and high efficiency solar cells. This section of the thesis is devoted to summarizing the important experimental results obtained from the work conducted under this thesis.

For the synthesis of ZnO NWs the hydrothermal technique was preferred due to its many advantages such as providing a contamination free growth route and allowing large-scale production of ZnO NW arrays in a cost effective manner. The required ZnO seed layers for the growth of ZnO NWs were deposited on transparent-conductive-oxide (ITO) pre-coated substrates by two different deposition techniques, sol-gel and RF-sputtering. The effect of growth parameters, such as temperature, precursor concentration, growth time, seed layer thickness and the type of the substrate, were investigated in detail for the both seed layer deposition techniques. From the NW growth cycles it was revealed that ZnO NWs can be successfully fabricated on any substrate (soda-lime-glass, indium tin oxide and polyethylene-terephthalate, etc.,) provided that they can withstand a temperature of 90 °C and the constituent precursors used for the preparation of the growth solution, such as zinc acetate dehydrate in 2-proponal and ethanolamine. In particular, achieving the synthesis of ZnO NWs on PET (a flexible substrate) is very crucial for the realization of flexible solar cells. In addition, it was found that there was a significant effect of growth time and the diameter of the grown ZnO NWs, ascribed to the fusion of poorly aligned NWs at longer growth periods. Result also revealed that while it was possible to synthesize homogeneously distributed and well-oriented ZnO NWs on sputter-deposited ZnO seed layers, it was not the case for those deposited by sol-gel technique. Therefore, the ZnO NWs grown on sputter-deposited seed layer were employed for the fabrication of core-shell solar cells.

Following the optimization of ZnO NWs, they were employed for the construction of ITO/n-ZnO NWs/p-AgGaSe₂/In core-shell structured solar cell. As an absorber layer

(shell) of this architecture, a member of Ag-based chalcopyrite compound (AgGaSe₂ (AGS)) was preferred, which is regarded as an alternative material to the most commonly employed material (CuInSe₂) in thin film based solar cells. In order to form AGS thin films, a route based on sequential deposition of Ag and GaSe layers by RF/DC sputtering was preferred. Before their incorporation into the core-shell device structure as the shell component, they were deposited on glass substrates for determining their structural, electrical and optical properties in detail. Once the optimum parameters (single phase, band gap and annealing temperature) for an effective absorber layer was determined, ZnO NWs 1.2-1.3 μm in length and 65-95 nm in diameter were decorated with a ~ 700 nm thick AGS thin film for the fabrication of the aforementioned solar cell architecture. Thermally-evaporated In and pre-coated ITO were employed as bottom and top contacts of the device, respectively. On completion of the device structure, to check the formation of p-n heterojunction between the core-material (ZnO) and shell-material (AGS), the I-V characteristic under dark condition was first recorded. After ensuring the formation of p-n heterojunction, the performance of the fabricated prototype solar cell was then tested under standard light illumination (100 mW/cm^2). Based on this measurement, the solar parameter, such as J_{sc} (short circuit current density), V_{oc} (open circuit voltage), FF (fill factor), and η (power conversion efficiency) were calculated to be 29.40 mA/cm^2 , 0.098 V , 60.25% and 1.74% , respectively. As it is discussed in the related part of the text, the constructed solar cell is the first reported so far in literature. Despite the fact that the power conversation efficiency for this first prototype is low compared to its planer counterpart, we believe that these results constitute an excellent initial step toward the realization of high efficiency solar cells that can be fabricated in a cost-effective way.

ZnO is regarded as one of the most important candidates for the realization of high-performance optoelectronic devices. Despite its high transparency in the visible region, ZnO has poor electrical conductivity, which can lead to reduction of solar cell performance. ZnO thin films which have poor electrical conductivity were doped with Sn element. Doping and annealing effects on structural, morphological, optical and electrical properties of undoped and Sn doped ZnO thin films, between 0.5 and 3.0 %, were investigated. ZnO/Sn/ZnO sandwich structure were deposited on SLG substrate by RF/DC sputtering method to fabricate Sn doped ZnO thin films. Structural analysis

revealed that all films exhibited a polycrystalline structure that can be characterized with (002) peak and there is a deterioration of the crystallinity after doping process due to the difference between the ionic radii of Sn ($r_{Sn^{4+}}$) and Zn ($r_{Zn^{2+}}$). However, following the applying post-annealing process a significant improvement in crystallinity of both doped and undoped ZnO films was observed. It was observed that the peak position shifts to higher angle (2θ) values at increasing Sn concentrations. AFM measurements have shown that there is a significant modification in surface morphology following the doping process and mulberry-like structures are formed for 3.0 % doping concentration throughout the sample. The transmission measurements indicated an average transmittance of 90 % in the visible range for the Sn-doped ZnO films, when annealed at 500 °C under N₂ gas flow. The band gap enhancement (red shift) from 3.26 eV to 3.15 eV with the increase of Sn content was observed for the SZO thin films. After the electrical measurements for the SZO thin films, it was deduced that the resistivity of the films first decreases with increasing both annealing temperature and Sn concentration, reaching the lowest value of $9.0 \times 10^{-3} \Omega \cdot \text{cm}$ at annealing temperature of 250 °C for 1.5 % Sn content (three orders of magnitude lower than Sn doped ZnO reported in the literature) and then increases with further increase in doping concentration and annealing temperature. The fabrication of SZO thin films in the present study with an average transmittance of 90 % in the visible range and a $9.0 \times 10^{-3} \Omega \cdot \text{cm}$ resistivity value reveal that the obtained results represent an excellent initial step for us toward the production of a high transparent-conductive-oxide (TCO) material by using relatively cheap and abundant constituent elements in our future studies.

A second prototype core-shell solar cell based on Si NWs was fabricated by coating Si NWs (20-80 nm in diameters and $\sim 3.5 \mu\text{m}$ in length) with sol-derived p-type CZTS absorber layer ($\sim 600 \text{ nm}$ thick). CZTS thin films were obtained via sol-gel processes, which is known to be a promising route to solve many difficulties reported so far associated with obtaining high quality CZTS thin films. For the chemical (composition), structural and optical characterization of the fabricated CZTS thin films prior to integration into the core-shell device structure, they were first deposited on soda lime glass substrates (SLG) and then subjected to a post-annealing process conducted at 350 °C for 30 min under N₂ flow. Energy dispersive X-ray analysis (EDXA) measurements showed that there was a slightly Cu-rich and Sn-poor chemical

composition of the deposited CZTS thin films. That is, respective values of $\frac{\text{Cu}}{\text{Zn}+\text{Sn}}$, $\frac{\text{Zn}}{\text{Sn}}$ and $\frac{\text{S}}{\text{Cu}+\text{Zn}+\text{Sn}}$ ratios were found to be 1.09, 1.07, and 0.97, which clearly revealed a chemical formula $\text{Cu}_{2.12}\text{Zn}_{1.00}\text{Sn}_{0.94}\text{S}_{3.94}$ for the deposited films. The results suggested that even the samples were not subjected to the sulphurization process the films were grown with a nearly stoichiometric composition, which also highlight the importance of the present study. From the XRD and Raman measurements it was found that a post annealing temperature at 350 °C was sufficient for the fabrication of mono-phase kesterite CZTS thin films with (112) main orientation without any binary, ternary and quaternary secondary phases. The optical properties of the deposited films were studied by performing reflectance and transmittance measurements in the wavelength range of 300-1000 nm at ambient temperature. The obtained spectra were used for the calculation of absorption coefficient, which was subsequently utilized for the determination of the band gap through the relation that exist between absorption coefficient and photon energy. Based on this relation, the band gap energy for the CZTS thin film annealed at 350 °C was evaluated to be 1.55 eV, which is very close to that required for an optimum absorber layer (1.45 eV) in the solar cell structure. The proposed core-shell device structure based on Si NWs was completed by thermal evaporation of Ag-metallic layer with dot pattern (60 nm thick and 1 μm in diameter) and 150 nm - thick Ag film onto the CZTS (shell) and back-side of the Si-wafer (1-10 Ω-cm), respectively. Tilted and top-views of the SEM images recorded for the Si NWs arrays decorated with CZTS clearly showed that almost all the NWs were perfectly covered with the CZTS layer, which is crucial for the effective charge collection as a result of high interaction interface in such a type solar device architecture. The formation of monophase kesterite CZTS with (112) main orientation onto Si NWs were also verified through the XRD and Raman measurements by observing the respective corresponding peaks as in the case of the films deposited onto SLG substrates. The photovoltaic performance of the constructed cell was tested under AM 1.5 light illumination and the V_{oc} of 0.40, J_{sc} of 9.60 mA/cm², FF of 26 % and power conversion efficiency of ~1.0 % were calculated. As discussed in the results and discussion part, the power conversion efficiency achieved with current device structure and material combination is well-below the ones obtained with planar-CZTS thin film based solar cells (~20 %). However, it must be pointed out at this juncture that these are the results obtained with the first prototype cell, which requires an extensive

optimization cycles for the core-material (Si NWs), shell-material (CZTS), contacts (degree of ohmicity and transparency) and passivation of Si-NWs for the saturation of dangling bonds. These results, while preliminary, suggest that once these issues are well addressed high efficiency core-shell Si/CZTS solar cells that comparable with their planer counterpart can be realized, which requires further experimental studies. This was reserved for a future work that will embody the effect of nanowire geometry and the CZTS thin film quality on the performance of the Si NWS/CZTS core-cell structure solar cells.

As a final part of the present study, a new fabrication route for the deposition of high quality CZTS thin films was preferred, which is based on the electron-beam evaporation of a single crystalline powder extracted from Bridgman-grown CZTS ingots, allowing us one-step deposition of a quaternary compound (CZTS). We started with the growth of Cu-poor and Zn-rich single crystalline CZTS compound, via a 3-zone vertical Bridgman system, that was employed as evaporation source for evaporation by electron-beam (e-beam) technique. In addition to supplying an evaporation source for the e-beam evaporation for the fabrication of CZTS thin films, to understand the fundamental properties of the CZTS material the grown single crystalline CZTS ingot was used for the extraction of a set of CZTS single crystalline wafers ($5 \times 10 \times 10 \text{ mm}^3$), which subsequently subjected to polishing process for the structural and electrical characterization stages. The elemental composition of the grown CZTS crystals was studied by performing EDX measurements, which indicated the growth of crystals having a Cu-poor and Zn-rich chemical composition with the evaluated $\text{Cu}/(\text{Zn} + \text{Sn}) = 0.98$ and $\text{Zn}/\text{Sn} = 1.05$ ratios. It is very crucial to obtain a starting material with a Cu-poor and Zn-rich composition since it is known that this stoichiometry prevents the formation of the detrimental defects or defect clusters, such as $\text{Cu}_{\text{Zn}} + \text{Sn}_{\text{Zn}}$ and/or $2\text{Cu}_{\text{Zn}} + \text{Sn}_{\text{Zn}}$. For the structural analysis the XRD and Raman measurements were carried out for the single crystalline CZTS samples. The combined results verified the formation of monophasic kesterite CZTS with (112) main orientation without precipitation of any secondary phases. For the study of revealing the photo-electrical properties of the grown single crystalline samples, the Hall Effect and photo-conductivity measurements were carried out by assigning thermally evaporated In in the van der Pauw geometry as the ohmic contacts. From the temperature dependent conductivity measurements it was deduced that the CZTS behaves as

semiconducting material. From the hot-probe technique, the conduction type of the CZTS was found to be p-type. To understand the response of the grown crystal to the visible light, the temperature dependent conductivity was repeated under a halogen lamp providing a $\sim 50 \text{ mW/ cm}^2$ intensity. The results showed that there was a pronounceable increase in the conductivity of the sample measured under light illumination with respect to that one measured in the dark, which suggests the responsivity of the CZTS crystal to the visible light. From the Hall effect measurements, the room temperature values of resistivity, hole concentration and mobility values were calculated to be $3.91 \text{ } \Omega\cdot\text{cm}$, $1.05 \times 10^{18} \text{ cm}^{-3}$, and $1.52 \text{ cm}^2/\text{V}\cdot\text{s}$, respectively. When compared to the values reported in the literature, it is seen that there is a difference, which can be taken as a normal outcome due to employed different technique and the amount of deviation from the stoichiometry.

Following the investigation of fundamental physical properties of the grown CZTS single crystals, a specific amount of crystalline powder was derived from the ingot and placed into a graphite crucible as an evaporation source for the e-beam method to fabricate Cu-poor and Zn-rich CZTS thin films onto soda lime glass substrates (substrate temperature: $150 \text{ }^\circ\text{C}$) with a high quality in terms of its electrical, structural and optical properties. The thickness of the deposited films was measured to be around 600 nm . To deduce the effect of annealing on physical properties of the deposited films, they were annealed between $250 \text{ }^\circ\text{C}$ and $500 \text{ }^\circ\text{C}$ under inert gas for 30 min time interval. From the EDXA measurement performed for the CZTS thin film annealed at $500 \text{ }^\circ\text{C}$, it was found that there was a chemical composition, which is very close to that recorded for the starting material. Namely, the values for Zn, Cu and Cu/(Zn+Sn) ratio were measured as 14% , 23.86% and 0.89 , respectively, suggesting the formation of a Cu-poor and Zn-rich chemical composition, which is a crucial requirement for the fabrication of high efficiency CZTS based thin film solar cells. The close atomic percentages of the constituent elements measured for both single crystalline and thin film samples clearly highlight the success of the present study. The XRD studies showed that while the as-grown samples had an amorphous structure, it then transformed into a mono-phase kesterite CZTS phase with (112) main orientation without any secondary formations when subjected to an annealing process performed at $500 \text{ }^\circ\text{C}$. The presence of mono-phase kesterite CZTS structure without additional secondary phases was also verified by the conducted Raman measurements. In

addition to structural analysis, the morphological analyses were also carried out to investigate the surface morphology of the fabricated thin film and how the post-annealing process modifies it by performing SEM and AFM measurements. From the results it was revealed that post-annealing process had a significant effect on the morphology of the films by observing an increase in grain sizes with increasing annealing temperature. The increase in grain sizes was in good agreement with results obtained from the XRD study, which implied the improvement in the degree of crystallinity following the heat treatment. The optic band gap of the CZTS thin film annealed at 500 °C was determined through the obtained reflection and transmission spectra and calculated to be 1.5 eV, known to be in very good agreement with those reported in the literature.

For the photo-electrical characterizations, thermally evaporated In contacts in the van der Pauw geometry was preferred. Temperature dependent photo-electrical measurements were conducted in 100-400 K range under both dark and light illumination provided by a halogen lamp with a 50 mW / cm² intensity. The conduction character of the film was determined through the hot-probe technique and found to be p-type. From the variation of conductivity as a function of temperature, two different linear regions were detected, found to be associated with two different acceptor levels located 12 meV and 60 meV above the valance band. Based on literature search, it was found that these acceptor levels are associated with the copper-vacancies (V_{Cu}), arising from the low content of the Cu in a Cu-poor chemical composition in the CZTS structure. While the room temperature resistivity value for the sample measured in the dark was $\sim 2 \times 10^3 \Omega \cdot \text{cm}$, it was reduced to $\sim 1.8 \times 10^3 \Omega \cdot \text{cm}$ under light illumination, which indicates the presence of photoresponse of the fabricated films to the visible light. Finally, from the Hall measurements, the room temperature mobility and hole concentration values were evaluated to be 1.22 cm²/ V. s and $2.6 \times 10^{15} \text{ cm}^{-3}$ for the film annealed at 500 °C, respectively, which are slightly below the respective values reported in the literature. This discrepancy may arise from the quality and stoichiometry of the prepared films. As a planned future study, the optimized CZTS thin films will be employed for the construction of both ZnO-NWs and Si-NWs based core-shell solar cells to improve the power conversion efficiency achieved with the present thesis study.



REFERENCES

- [1] **Karaağaç H., Peksu E., Arici Ü.E., Islam M.S.** . (2016). One-Dimensional Nano-Structured Solar Cells. In D. J. Ünlü H (Ed.), *Low-Dimensional and Nanostructured Materials and Devices* (pp. 351-400). Switzerland: Springer International Publishing.
- [2] **Perera F.** (2018). Pollution from Fossil-Fuel Combustion is the Leading Environmental Threat to Global Pediatric Health and Equity: Solutions Exist. *Int J Environ Res Public Health*, 15, 1-17.
- [3] **Ranabhat K., P. L., Revina A.A., Andrianov K., Lapshinsky V., Sofronova E.** (2016). An introduction to solar cell technology. *Journal of Applied Engineering Science*, 14, 481-491.
- [4] **Kibria M., A. A., Saad M., Sony F., Hossain S.U.I.** (2014). *A Review: Comparative studies on different generation solar cells technology*. Paper presented at the ICEAB 2014, Bangladesh.
- [5] **Fan, Z., Ruebusch, D., Rathore, A., Kapadia, R., Ergen, O., Leu, P., & Javey, A.** (2009). Challenges and prospects of nanopillar-based solar cells. *Nano Research*, 211, 829-843.
- [6] **Garnett, E. C., & Yang, P. D.** (2008). Silicon nanowire radial p-n junction solar cells. *Journal of the American Chemical Society*, 13029, 9224-9225.
- [7] **Czaban, J. A., Thompson, D. A., & LaPierre, R. R.** (2009). GaAs core-shell nanowires for photovoltaic applications. *Nano Letters*, 91, 148-154.
- [8] **Zhang, X., Wang, L. S., & Zhou, G. Y.** (2005). Synthesis of well-aligned ZnO nanowires without catalysts. *Reviews on Advanced Materials Science*, 101, 69-72.
- [9] **Divitini, G., Plank, N. O. V., Snaith, H. J., Welland, M. E., & Ducati, C.** (2010). High-resolution TEM characterization of ZnO core-shell nanowires for dye-sensitized solar cells. *Journal of Physics: Conference Series*, 2411, 012031.
- [10] **Law, M., Greene, L. E., Radenovic, A., Kuykendall, T., Liphardt, J., & Yang, P.** (2006). ZnO–Al₂O₃ and ZnO–TiO₂ Core–Shell Nanowire Dye-Sensitized Solar Cells. *The Journal of Physical Chemistry B*, 11045, 22652-22663.
- [11] **Plank, N. O. V., Snaith, H. J., Ducati, C., Bendall, J. S., Schmidt-Mende, L., & Welland, M. E.** (2008). A simple low temperature synthesis route for ZnO–MgO core–shell nanowires. *Nanotechnology*, 1946, 465603.
- [12] **Zhang M., W. Y. J., Moulin E., Grützmacher D., Chien C. J., Chang P. C., Gao X., Carius R. and Lu J. G.** (2012). Core-shell CdTe–TiO₂ nanostructured solar cell. *Journal of Materials Chemistry*, 2221, 10441-10443.
- [13] **Peksu, E., & Karaagac, H.** (2019). A third generation solar cell based on wet-chemically etched Si nanowires and sol-gel derived Cu₂ZnSnS₄ thin films. *Journal of Alloys and Compounds*, 774, 1117-1122.
- [14] **Karaagac, H., Kaleli, M., & Parlak, M.** (2009). Characterization of AgGa_{0.5}In_{0.5}Se₂ thin films deposited by electron-beam technique. *Journal of Physics D-Applied Physics*, 4216, 165413.

- [15] **Siebentritt, S.** (2011). What limits the efficiency of chalcopyrite solar cells? *Solar Energy Materials & Solar Cells*, 95, 1471-1476.
- [16] **Kuriyama, K., & Nakamura, F.** (1987). Electrical Transport-Properties and Crystal-Structure of Liznas. *Physical Review B*, 368, 4439-4441.
- [17] **Yan B., Zhang. S. C.** (2012). Topological materials. *Rep. Prog. Phys.*, 75, 096501-096523.
- [18] **Rockett A.A.** (2010). Current status and opportunities in chalcopyrite solar cells. *Current Opinion in Solid State and Materials Science*, 14, 143-148.
- [19] **Lee M., L. S. M., Jung S., Ahn S, Cho J. S., Park J., Eh Y., Gwak J., Shin K., Yoon K., Cho Y.S., Yun J.H.** . (2015). Highly efficient flexible $\text{CuIn}_{0.7}\text{Ga}_{0.3}\text{Se}_2$ solar cells with a thick Na/Mo layer deposited directly on stainless steel. *Applied Surface Science*, 346, 562-566.
- [20] **Venkatachalam M.K., J. M., Balasundaraprabhu S., Muthukumarasamy, N.** (2008). Effect of annealing on the structural properties of electron beam deposited CIGS thin films. *Thin Solid Films*, 516, 6848-6852.
- [21] **Benmir A., A. M. S.** (2013). Analytical Modeling and Simulation of CIGS Solar Cells. *Energy Procedia*, 36, 618-627.
- [22] **Li M., C. F., Li C., Xia C., Wang T., Sun M.** (2012). CIS and CIGS thin films prepared by magnetron sputtering. *Procedia Engineering*, 27, 12-19.
- [23] **Jackson P., H. D., Lotter E., Paetel S., Wuerz R., Menner R., Wischmann W. and Powalla M.** (2011). New world record efficiency for $\text{Cu}(\text{In,Ga})\text{Se}_2$ thin-film solar cells beyond 20%. *Progress in Photovoltaics: Research and Applications*, 19.
- [24] **Mehdaoui S., B. N., Benabdeslem M., Aissaoui O., Bechiri L., Portier X.** . (2011). Investigation of Copper-Chalcopyrite Thin Films from Nanoparticle Powder *Energy Procedia*, 10, 94-100.
- [25] **Deshmukh L. P., S. R. V., Masumdar E. U., Sharon M.** . (2012). $\text{Cu}_{1-x}\text{In}_x\text{Se}_2$ thin films: Deposition by spray pyrolysis and characteristics. *Solar Energy*, 86, 1910-1919.
- [26] **Jackson P., H. D., Wuerz R., Kiowski O., Bauer A., Friedlmeier T. M., Powalla M.** (2015). Properties of $\text{Cu}(\text{In,Ga})\text{Se}_2$ solar cells with new record efficiencies up to 21.7%. *physica status solidi (RRL) – Rapid Research Letters*, 9, 28-31.
- [27] **Karaagac, H., Parlak, M.** (2009). Effects of annealing on structural and morphological properties of e-beam evaporated AgGaSe_2 thin films. *Applied Surface Science*, 25511, 5999-6006.
- [28] **Karaağaç H.** (2010). *Electrical, structural and optical properties of $\text{AgGaSe}_{2-x}\text{S}_x$ thin films grown by sintered powder* (PhD Thesis), Middle East Technical University, Ankara, Turkey.
- [29] **Karaagac, H., & Parlak, M.** (2011). Deposition and characterization of layer-by-layer sputtered AgGaSe_2 thin films. *Applied Surface Science*, 25713, 5731-5738.
- [30] **Mitzi, D. B.** (2009). Solution Processing of Chalcogenide Semiconductors via Dimensional Reduction. *Advanced Materials*, 2131, 3141-3158.
- [31] **Repins, I., Contreras, M. A., Egaas, B., DeHart, C., Scharf, J., Perkins, C. L., Noufi, R.** (2008). 19.9 % efficient $\text{ZnO}/\text{CdS}/\text{CuInGaSe}_2$ solar cell with 81.2 % fill factor. *Progress in Photovoltaics*, 163, 235-239.

- [32] **Fontanéa X., I. R. V., Saucedoa E., Schorrb S., Yukhymchukc V. O., Valakhc M. Y., Pérez-Rodrígueza A., Morante J.R. .** (2012). Vibrational properties of stannite and kesterite type compounds: Ramanscattering analysis of $\text{Cu}_2(\text{Fe,Zn})\text{SnS}_4$. *Journal of Alloys and Compounds*, 539, 190-194.
- [33] **Subramaniam, E. P., Rajesh, G., Muthukumarasamy, N., Thambidurai, M., Asokan, V., & Velauthapillai, D.** (2014). Solar cells of $\text{Cu}_2\text{ZnSnS}_4$ thin films prepared by chemical bath deposition method. *Indian Journal of Pure & Applied Physics*, 529, 620-624.
- [34] **Shockley, W., & Queisser, H. J.** (1961). Detailed Balance Limit of Efficiency of p-n Junction Solar Cells *Journal of Applied Physics*, 323, 510-519.
- [35] **Chapin D.M., F. C. S., Pearson G.L.** (1954). A New Silicon p-n Junction Photocell for Converting Solar Radiation into Electrical Power. *Journal of Applied Physics*, 25, 676-677.
- [36] **Schultz-Wittmann O., G. S., Willeke G. P.** (2004). Multicrystalline Silicon Solar Cells Exceeding 20% Efficiency. *Progress in Photovoltaics Research and Applications*, 12, 553-558.
- [37] **Taguchi M., Y. A., Tohoda S., Matsuyama K., Nakamura Y., Nishiwaki T., Fujita K., Maruyama E.** (2014). 24.7% Record Efficiency HIT Solar Cell on Thin Silicon Wafer. *IEEE Journal of Photovoltaics*, 4, 96-99.
- [38] **Wagner S., S. J. L., Migliorato P., Kasper H.M. .** (1974). $\text{CuInSe}_2/\text{CdS}$ heterojunction photovoltaic detectors. *Applied Physics Letters*, 25, 434-435.
- [39] **Kazmerski L.L., W. F. R., Morgan G.K. .** (1976). Thin-film $\text{CuInSe}_2/\text{CdS}$ heterojunction solar cells. *Applied Physics Letters*, 29 268-270.
- [40] **Murthy Y.S., H. O. M., Naidu B.S., Reddy P.J.** (1991). Characterization of p- $\text{AgGaSe}_2/\text{n-CdS}$ thin film heterojunction. *Materials Letters*, 10, 504-508.
- [41] **Katagiri, H., Sasaguchi, N., Hando, S., Hoshino, S., Ohashi, J., & Yokota, T.** (1997). Preparation and Evaluation of $\text{Cu}_2\text{ZnSnS}_4$ Thin Films by Sulfurization of E-B Evaporated Precursors. *Solar Energy Materials and Solar Cells*, 491-4, 407-414.
- [42] **Katagiri H.** (2012). Survey of development of CZTS-based thin film solar cells. *IEEE 3rd International Conference on Photonics, IEEE, Penang, Malaysia*, 1, 345-349.
- [43] **Yan C., H. J., Sun K., Johnston S., Zhang Y., Sun H., Pu A., He M., Liu F., Eder K., Yang L., Cairney J. M., Ekins-Daukes N. J., Hameiri Z., Stride J. A., Chen S., Green M. A. and Hao X.** (2018). $\text{Cu}_2\text{ZnSnS}_4$ solar cell power conversion efficiency breaking the 10% barrier through heterojunction heat treatment. *Nature Energy*, 3, 764–772
- [44] **Xia Y., Y. P., Sun Y., Wu Y., Mayers B., Gates B., Yin Y., Kim F., Yan H.** (2003). One-Dimensional Nanostructures: Synthesis, Characterization, and Applications. *Advanced Materials*, 15, 353-389.
- [45] **Kayes B.M., A. H. A., Lewis N.S.** (2005). Comparison of the device physics principles of planar and radial p-n junction nanorod solar cells. *Journal of Applied Physics*, 97, 114302.
- [46] **Tsakalakos, L., Balch, J., Fronheiser, J., Korevaar, B. A., Sulima, O., & Rand, J.** (2007). Silicon nanowire solar cells. *Applied Physics Letters*, 9123, 2331171-2331173.

- [47] **Yuhas B.D., Y. P.** (2009). Nanowire-Based All-Oxide Solar Cells. *Journal of the American Chemical Society*, 131, 3756-3761.
- [48] **Akbarnejad E., N. F. D. a. G. M.** (2018). Core-shell solar cell fabrication using heterostructure of ZnO-nanowires arrays decorated with sputtered CdTe-nanoparticles. *Journal of Physics D Applied Physics*, 51, 0951051-0951057.
- [49] **Karaagac, H., Parlak, M., Yengel, E., & Islam, M. S.** (2013). Heterojunction solar cells with integrated Si and ZnO nanowires and a chalcopyrite thin film. *Materials Chemistry and Physics*, 1401, 382-390.
- [50] **Bosio, A., & Romeo, A.** (2011). *Thin Film Solar Cells: Current Status and Future Trends*. Hauppauge, NY, USA: Nova Science Publishers.
- [51] **Roy, U. N., Cui, Y., Hawrami, R., Burger, A., Orona, L., & Goldstein, J. T.** (2006). AgGaSe₂: A highly photoconductive material. *Solid State Communications*, 13910, 527-530.
- [52] **Schunemann, P. G., Schepler, K. L., & Budni, P. A.** (1998). Nonlinear frequency conversion performance of AgGaSe₂, ZnGeP₂, and CdGeAs₂. *Mrs Bulletin*, 237, 45-49.
- [53] **Shay, J. L., & Wernick, J. H.** (1975). The Chalcopyrite Structure and Crystal Growth. In B. R. Pamplin (Ed.), *Ternary Chalcopyrite Semiconductors: Growth, Electronic Properties, and Applications* (pp. 3-78). Pergamon.
- [54] **Karaagac, H., Yengel, E., & Islam, M. S.** (2012). Physical properties and heterojunction device demonstration of aluminum-doped ZnO thin films synthesized at room ambient via sol-gel method. *Journal of Alloys and Compounds*, 5211, 155-162.
- [55] **Su, Y., Zou, X. P., Meng, X. M., Teng, G. Q., Yang, G. Q., & Lu, X. M.** (2010). ZnO Nanorod Arrays and Nanowires by Hydrothermal Growth. *Advanced Materials Research*, 123125, 811-814.
- [56] **Wan, H., & Ruda, H. E.** (2010). A study of the growth mechanism of CVD-grown ZnO nanowires. *Journal of Materials Science-Materials in Electronics*, 2110, 1014-1019.
- [57] **Xu, H. J., Hou, Y. M., Gao, J. Y., Zhu, H. C., Zhu, R., Sun, Y. H., . . . Yu, D. P.** (2011). Regrowth of Template ZnO Nanowires for the Underlying Catalyst-Free Growth Mechanism. *Crystal Growth & Design*, 116, 2135-2141.
- [58] **Yuan, D. J., Guo, R., Wei, Y. G., Wu, W. Z., Ding, Y., Wang, Z. L., & Das, S. M.** (2010). Heteroepitaxial Patterned Growth of Vertically Aligned and Periodically Distributed ZnO Nanowires on GaN Using Laser Interference Ablation. *Advanced Functional Materials*, 2020, 3484-3489.
- [59] **Vayssieres, L.** (2003). Growth of arrayed nanorods and nanowires of ZnO from aqueous solutions. *Advanced Materials*, 155, 464-466.
- [60] **Aslan, M. H., Oral, A. Y., Mensur, E., Gul, A., & Basaran, E.** (2004). Preparation of c-axis-oriented zinc-oxide thin films and the study of their microstructure and optical properties. *Solar Energy Materials and Solar Cells*, 824, 543-552.
- [61] Joint Committee on Powder Diffraction Standards (JCPDS) Card No: 31-1240.
- [62] **Patidar, D., Rathore, K. S., Saxena, N. S., Sharma, K., & Sharma, T. P.** (2008). Energy band gap and conductivity measurement of CdSe thin films. *Chalcogenide Letters*, 52, 21-25.

- [63] **Jia, G. B., Steglich, M., Sill, I., & Falk, F.** (2012). Core-shell heterojunction solar cells on silicon nanowire arrays. *Solar Energy Materials and Solar Cells*, 961, 226-230.
- [64] **Kapadia, R., Fan, Z. Y., Takei, K., & Javey, A.** (2012). Nanopillar photovoltaics: Materials, processes, and devices. *Nano Energy*, 11, 132-144.
- [65] **Armstrong, J. C., & Cui, J. B.** (2015). Three-dimensional structures based on ZnO/CdS and ZnO/(Zn,Mg)O core-shell nanowires embedded in Cu(In,Ga)S₂ for solar cell applications. *Solar Energy Materials and Solar Cells*, 1411, 356-363.
- [66] **Chandra, G. H., Hussain, O. M., Uthanna, S., & Naidu, B. S.** (2001). Characterization of p-AgGa_{0.25}In_{0.75}Se₂/n-Zn_{0.35}Cd_{0.65}S polycrystalline thin film heterojunctions. *Materials Science and Engineering B-Solid State Materials for Advanced Technology*, 861, 60-63.
- [67] **Yamada, K., Hoshino, N., & Nakada, T.** (2006). Crystallographic and electrical properties of wide gap Ag(In_{1-x}Ga_x)Se₂ thin films and solar cells. *Science and Technology of Advanced Materials*, 71, 42-45.
- [68] **Soga, T.** (2006). Fundamentals of Solar Cell. In T. Soga (Ed.), *Nanostructured Materials for Solar Energy Conversion* (pp. 3-43). Amsterdam: Elsevier.
- [69] **Peng, K. Q., Xu, Y., Wu, Y., Yan, Y. J., Lee, S. T., & Zhu, J.** (2005). Aligned single-crystalline Si nanowire arrays for photovoltaic applications. *Small*, 111, 1062-1067.
- [70] **Garnett, E., & Yang, P. D.** (2010). Light Trapping in Silicon Nanowire Solar Cells. *Nano Letters*, 103, 1082-1087.
- [71] **Kayes, B. M., Atwater, H. A., & Lewis, N. S.** (2005). Comparison of the device physics principles of planar and radial p-n junction nanorod solar cells. *Journal of Applied Physics*, 9711, Article ID 114302.
- [72] **Musselman, K. P., & Schmidt-Mende, L.** (2011). Nanostructured inorganic solar cells. *Green*, 11, 7-27.
- [73] **Peksu, E., & Karaagac, H.** (2015). Synthesis of ZnO Nanowires and Their Photovoltaic Application: ZnO Nanowires/AgGaSe₂ Thin Film Core-Shell Solar Cell. *Journal of Nanomaterials*, 2015ID 516012, 1-10.
- [74] **Shishiyanu, S. T., Shishiyanu, T. S., & Lupan, O. I.** (2005). Sensing characteristics of tin-doped ZnO thin films as NO₂ gas sensor. *Sensors and Actuators B: Chemical*, 1071, 379-386.
- [75] **Bao, J., Zimmler, M. A., Capasso, F., Wang, X., & Ren, Z. F.** (2006). Broadband ZnO Single-Nanowire Light-Emitting Diode. *Nano Letters*, 6, 1719-1722.
- [76] **Siqueiros, J. M., Diaz, J. A., Contreras, O., & Hirata, G. A.** (1996). Low Resistivity-Highly Transparent ZnO:Ga TCO's Grown by Laser Ablation. *Materials Research Society*, 397, 247-252.
- [77] **Ilcan, S., Caglar, M., & Caglar, Y.** (2010). Sn doping effects on the electro-optical properties of sol gel derived transparent ZnO films. *Applied Surface Science*, 25623, 7204-7210.
- [78] **Khuli, M., Fazouan, N., El Makarim, H. A., El Halani, G., & Atmani, E. H.** (2016). Comparative first principles study of ZnO doped with group III elements. *Journal of Alloys and Compounds*, 688, Part B, 368-375.

- [79] **Lee, J. H., & Park, B. O.** (2003). Transparent conducting ZnO:Al, In and Sn thin films deposited by the sol–gel method. *Thin Solid Films*, 4261–2, 94-99.
- [80] **Chen, K. J., Hung, F. Y., Chen, Y. T., Chang, S. J., & Hu, Z. S.** (2010). Surface Characteristics, Optical and Electrical Properties on Sol-Gel Synthesized Sn-Doped ZnO Thin Film. *Materials Transactions*, 517, 1340-1345.
- [81] **Xing, L. J., Chang, Y. Q., Shao, C. J., & Lin, L. Y. W.** (2016). Room temperature gas sensing property and sensing mechanism of Sn-doped ZnO thin film. *Acta Physica Sinica*, 659, 97302-97308.
- [82] **Sreedhar, A., Kwon, J. H., Yi, J., & Gwag, J. S.** (2016). Improved physical properties of Al-doped ZnO thin films deposited by unbalanced RF magnetron sputtering. *Ceramics International*, 4213, 14456-14462.
- [83] **Holmelund, E., Schou, J., Tougaard, S., & Larsen, N. B.** (2002). Pure and Sn-doped ZnO films produced by pulsed laser deposition. *Applied Surface Science*, 197–198, 467-471.
- [84] **Saleem, M., Fang, L., Wakeel, A., Rashad, M., & Kong, C. Y.** (2012). Simple Preparation and Characterization of Nano-Crystalline Zinc Oxide Thin Films by Sol-Gel Method on Glass Substrate. *World Journal of Condensed Matter Physics*, 21, 10-15.
- [85] **Ajili, M., Castagné, M., & Turki, N. K.** (2013). Study on the doping effect of Sn-doped ZnO thin films. *Superlattices and Microstructures*, 531, 213-222.
- [86] **Do, T. C., Pucci, A., & Wandelt, K.** (2009). *Physics and engineering of new materials*. Berlin: Springer.
- [87] **Malevu, T. D., & Ocaya, R. O.** (2015). Effect of Annealing Temperature on Structural, Morphology and Optical Properties of ZnO Nano-Needles Prepared by Zinc-Air Cell System Method. *International Journal of Electrochemical Science*, 102, 1752 - 1761.
- [88] **Karamdel, J., Dee, C. F., & Majlis, B. Y.** (2011). Effects of Annealing Conditions on the Surface Morphology and Crystallinity of Sputtered ZnO Nano Films *Sains Malaysiana*, 403, 209–213
- [89] **El Hallani, G., Nasih, S., Fazouan, N., Liba, A., Khuili, M., Sajieddine, M., . . . Atmani, E. H.** (2017). Comparative study for highly Al and Mg doped ZnO thin films elaborated by sol gel method for photovoltaic application. *Journal of Applied Physics*, 12113, 1351031-1351037.
- [90] **Nakrela, A., Benramdane, N., Bouzidi, A., Kebbab, Z., Medles, M., & Mathieu, C.** (2016). Site location of Al-dopant in ZnO lattice by exploiting the structural and optical characterisation of ZnO:Al thin films. *Results in Physics*, 6, 133-138.
- [91] **Sahoo, T., Pandian, C., Rahulan, K. M., & Rath, M. K.** (2017). Metal nanoparticle assisted growth of assembled zinc oxide nanostructure by low temperature solution phase technique. *Materials Letters*, 186, 214-216.
- [92] **Sanjeev, S., & Kekuda, D.** (2015). Effect of annealing temperature on the structural and optical properties of zinc oxide (ZnO) thin films prepared by spin coating process. *IOP Conference Series: Materials Science and Engineering*, 731, 0121491-0121495.

- [93] **El hamali, S. O., Cranton, W. M., Kalfagiannis, N., Hou, X., Ranson, R., & Koutsogeorgis, D. C.** (2016). Enhanced electrical and optical properties of room temperature deposited Aluminium doped Zinc Oxide (AZO) thin films by excimer laser annealing. *Optics and Lasers in Engineering*, 80, 45-51.
- [94] **Hodgson, J. N.** (1970). *Optical Absorption and Dispersion in Solids*: London : Chapman & Hall.
- [95] **Kim, M. S., Yim, K. G., Son, J. S., & Leem, J. Y.** (2012). Effects of Al concentration on structural and optical properties of Al-doped ZnO thin films. *Bulletin of the Korean Chemical Society*, 33(4), 1235-1241.
- [96] **Sun, Y., & Wang, C.** (2017). 2D free-standing Ge-doped ZnO: excellent electron-emitter and excitation-power-dependent photoluminescence redshift. *RSC Adv.*, 7(19), 11448-11454.
- [97] **Yung, K. C., Liem, H., & Choy, H. S.** (2009). Enhanced redshift of the optical band gap in Sn-doped ZnO free standing films using the sol-gel method. *Journal of Physics D: Applied Physics*, 42(18), 185002.
- [98] **Aksoy, S., Caglar, Y., Ilcan, S., & Caglar, M.** (2010). Effect of Sn dopants on the optical and electrical properties of ZnO films. *Optica Applicata*, XL, 7-14.
- [99] **Ali, I., Ullah, Z., Siraj, K., Rafique, M. S., & Khaleeq-ur-Rahman, M.** (2014). Sn doped ZnO Thin Films Prepared by Pulsed Laser Deposition for Photovoltaic Applications. *International Journal of Thin Films Science and Technology*, 33, 107-111.
- [100] **Saurdi, I., Mamat, M. H., Ishak, A., & Rusop, M.** (2015). Structural, Optical and Electrical Properties of Nano-structured Sn-doped ZnO Thin Film via Sol Gel Spin Coating Technique. In R. Hassan, M. Yusoff, A. Alisibramulisi, N. Mohd Amin, & Z. Ismail (Eds.), *InCIEC 2014, Proceedings of the International Civil and Infrastructure Engineering Conference 2014* (pp. 937-947). Singapore: Springer.
- [101] **Islam, M. A., Rahman, K. S., Haque, F., Khan, N. A., Akhtaruzzaman, M., Alam, M. M., Amin, N.** (2015). Effect of Sn Doping on the Properties of Nano-Structured ZnO Thin Films Deposited by Co-Sputtering Technique. *Journal of Nanoscience and Nanotechnology*, 15(11), 9184-9191.
- [102] **Guo, J., Zheng, J., Song, X., & Sun, K.** (2013). Synthesis and conductive properties of Ga-doped ZnO nanosheets by the hydrothermal method. *Materials Letters*, 97, 34-36.
- [103] **Blakers, A., Zin, N., McIntosh, K. R., & Fong, K.** (2013). High Efficiency Silicon Solar Cells. *Energy Procedia*, 33, 1-10.
- [104] **Kessler, F., & Rudmann, D.** (2004). Technological aspects of flexible CIGS solar cells and modules. *Solar Energy*, 77(6), 685-695.
- [105] **Kim, J., Hiroi, H., Todorov, T. K., Gunawan, O., Kuwahara, M., Gokmen, T., Mitzi, D. B.** (2014). High Efficiency Cu₂ZnSn(S,Se)₄ Solar Cells by Applying a Double In₂S₃/CdS Emitter. *Advanced Materials*, 26(44), 7427-7431.
- [106] **Zhang, L., Karthikeyan, S., Sibakoti, M. J., & Campbell, S. A.** (2015, 14-19 June 2015). *Cu₂ZnSnS₄ Thin film growth optimization and post rapid thermal annealing of solar cells and its influence on device performance*. Paper presented at the 2015 IEEE 42nd Photovoltaic Specialist Conference (PVSC), New Orleans, LA, USA.

- [107] **Inamdar, A. I., Lee, S., Jeon, K. Y., Lee, C. H., Pawar, S. M., Kalubarme, R. S., Kim, H.** (2013). Optimized fabrication of sputter deposited $\text{Cu}_2\text{ZnSnS}_4$ (CZTS) thin films. *Solar Energy*, 91, 196-203.
- [108] **Vanalakar, S. A., Agawane, G. L., Shin, S. W., Suryawanshi, M. P., Gurav, K. V., Jeon, K. S., . . . Kim, J. H.** (2015). A review on pulsed laser deposited CZTS thin films for solar cell applications. *Journal of Alloys and Compounds*, 619, 109-121.
- [109] **Swami, S. K., Kumar, A., & Dutta, V.** (2013). Deposition of kesterite $\text{Cu}_2\text{ZnSnS}_4$ (CZTS) thin Films by spin coating technique for solar cell application. *Energy Procedia*, 33, 198-202.
- [110] **Ramasamy, K., Malik, M. A., & O'Brien, P.** (2011). The chemical vapor deposition of $\text{Cu}_2\text{ZnSnS}_4$ thin films. *Chemical Science*, 26, 1170-1172.
- [111] **Song, X., Ji, X., Li, M., Lin, W., Luo, X., & Zhang, H.** (2014). A Review on Development Prospect of CZTS Based Thin Film Solar Cells. *International Journal of Photoenergy*, 2014, 11-16.
- [112] **Jiang, F., & Shen, H. L.** (2013). Fabrication and photovoltaic properties of $\text{Cu}_2\text{ZnSnS}_4/\text{i-a-Si}/\text{n-a-Si}$ thin film solar cells. *Applied Surface Science*, 280, 138-143.
- [113] **Fernandes, P. A., Salome, P. M. P., & da Cunha, A. F.** (2009). Growth and Raman scattering characterization of $\text{Cu}_2\text{ZnSnS}_4$ thin films. *Thin Solid Films*, 5177, 2519-2523.
- [114] **Karaagac, H., & Parlak, M.** (2010). Investigation of physical properties of quaternary $\text{AgGa}_0.5\text{In}_0.5\text{Te}_2$ thin films deposited by thermal evaporation. *Journal of Alloys and Compounds*, 5032, 468-473.
- [115] **Ansari, M. Z., & Khare, N.** (2014). Structural and optical properties of CZTS thin films deposited by ultrasonically assisted chemical vapour deposition. *Journal of Physics D-Applied Physics*, 4718, 185101-185106.
- [116] **Xia, Y., Chen, Z., Zhang, Z., Fang, X., & Liang, G.** (2014). A nontoxic and low-cost hydrothermal route for synthesis of hierarchical $\text{Cu}_2\text{ZnSnS}_4$ particles. *Nanoscale Research Letters*, 91, 208-208.
- [117] **Jiang, F., Shen, H. L., Wang, W., & Zhang, L.** (2011). Preparation and properties of $\text{Cu}_2\text{ZnSnS}_4$ absorber and $\text{Cu}_2\text{ZnSnS}_4/\text{amorphous silicon}$ thin-film solar cell. *Applied Physics Express*, 47, 4101-4103.
- [118] **Song, N., Young, M., Liu, F. Y., Erslev, P., Wilson, S., Harvey, S. P., Green, M. A.** (2015). Epitaxial $\text{Cu}_2\text{ZnSnS}_4$ thin film on Si (111) 4 degrees substrate. *Applied Physics Letters*, 10625, 2521021-2521025.
- [119] **Yeh, M. Y., Lei, P. H., Lin, S. H., & Yang, C. D.** (2016). Copper-Zinc-Tin-Sulfur thin film using spin-coating technology. *Materials*, 9526, 1-12.
- [120] **Gunawan, O., & Guha, S.** (2009). Characteristics of vapor-liquid-solid grown silicon nanowire solar cells. *Solar Energy Materials and Solar Cells*, 938, 1388-1393.
- [121] **Aberle, A. G.** (2007). Progress in Crystalline Silicon Thin-Film Solar Cells. In T. P. Hough (Ed.), *Recent Developments in Solar Energy* (pp. 233-248). New York: Nova Science Publishers.
- [122] **Gómez, D., Menéndez, A., Sánchez, B., Martínez, A., Andrés, L. J., Menéndez, A., . . . Sánchez, B.** (2011). *Novel concepts for low-cost and high-efficient thin film solar cells*. Paper presented at the SPIE Solar Energy + Technology.

- [123] **Green, M. A., Emery, K., Hishikawa, Y., Warta, W., & Dunlop, E. D.** (2013). Solar cell efficiency tables (version 42). *Progress in Photovoltaics: Research and Applications*, 215, 827-837.
- [124] **Emsley, J.** (1998). *The Elements* (Third ed.). Oxford: Oxford Univ. Press.
- [125] **Diwate, K., Mohite, K., Shinde, M., Rondiya, S., Pawbake, A., Date, A.,** **Jadkar, S.** (2017). Synthesis and Characterization of Chemical Spray Pyrolysed CZTS Thin Films for Solar Cell Applications. *Energy Procedia*, 1103, 180-187.
- [126] **Tanaka, T., Kawasaki, D., Nishio, M., Guo, Q., & Ogawa, H.** (2006). Fabrication of $\text{Cu}_2\text{ZnSnS}_4$ thin films by co-evaporation. *Physica Status Solidi (c)*, 38, 2844-2847.
- [127] **Aldalbahi, A., Mkawi, E. M., Ibrahim, K., & Farrukh, M. A.** (2016). Effect of sulfurization time on the properties of copper zinc tin sulfide thin films grown by electrochemical deposition. *Scientific reports*, 6, 32431-32431.
- [128] **Nagaoka, A., Yoshino, K., Taniguchi, H., Taniyama, T., Kakimoto, K., & Miyake, H.** (2013). Growth and characterization of $\text{Cu}_2\text{ZnSnS}_4$ single crystals. *Physica Status Solidi (a)*, 2107, 1328-1331.
- [129] **Katagiri, H., Saitoh, K., Washio, T., Shinohara, H., Kurumadani, T., & Miyajima, S.** (2001). Development of thin film solar cell based on $\text{Cu}_2\text{ZnSnS}_4$ thin films. *Solar Energy Materials and Solar Cells*, 651, 141-148.
- [130] **Chen, S., Wang, L. W., Walsh, A., Gong, X., & Wei, S. H.** (2012). Abundance of $\text{CuZn} + \text{SnZn}$ and $2\text{CuZn} + \text{SnZn}$ defect clusters in kesterite solar cells. *Applied Physics Letters*, 10122.
- [131] **Moreno, R., Ramirez, E. A., & Guzmán, G. G.** (2016). Study of optical and structural properties of CZTS thin films grown by co-evaporation and spray pyrolysis. *Journal of Physics: Conference Series*, 6871, 012041.
- [132] **Nagaoka, A., Miyake, H., Taniyama, T., Kakimoto, K., & Yoshino, K.** (2013). Correlation between intrinsic defects and electrical properties in the high-quality $\text{Cu}_2\text{ZnSnS}_4$ single crystal. *Applied Physics Letters*, 10311, 112107.
- [133] **Chen, S., Walsh, A., Gong, X. G., & Wei, S. H.** (2013). Classification of lattice defects in the kesterite $\text{Cu}_2\text{ZnSnS}_4$ and $\text{Cu}_2\text{ZnSnSe}_4$ earth-abundant solar cell absorbers. *Advanced Materials*, 2511, 1522-1539.
- [134] **Ericson, T., Scragg, J. J., Kubart, T., Törndahl, T., & Platzer-Björkman, C.** (2013). Annealing behavior of reactively sputtered precursor films for $\text{Cu}_2\text{ZnSnS}_4$ solar cells. *Thin Solid Films*, 535, 22-26.
- [135] **Cullity, B. L.** (1978). *Elements of X-Ray Diffractions* (M. Cohen Ed. 2. ed. Vol. 102). Canada: Addison-Wesley Publishing Company.
- [136] **Li, Z., Ho, J. C. W., Lee, K. K., Zeng, X., Zhang, T., Wong, L. H., & Lam, Y. M.** (2014). Environmentally friendly solution route to kesterite $\text{Cu}_2\text{ZnSn}(\text{S},\text{Se})_4$ thin films for solar cell applications. *RSC Advances*, 451, 26888-26894.
- [137] **Fernandes, P., Salomé, P., & da Cunha, A. F.** (2011). Study of polycrystalline $\text{Cu}_2\text{ZnSnS}_4$ films by Raman scattering. *Journal of Alloys and Compounds*, 50928, 7600-7606.
- [138] **Fernandes P.A., S. P. M. P., Cunha A.F.D.** (2010). A study of ternary Cu_2SnS_3 and Cu_3SnS_4 thin films prepared by sulfurizing stacked metal precursors. *Journal of Physics D: Applied Physics*, 43.

- [139] **Fernandes P.A., S. P. M. P., Cunha A.F.D.** (2010). $\text{Cu}_x\text{SnS}_{x+1}$ ($x = 2, 3$) thin films grown by sulfurization of metallic precursors deposited by dc magnetron sputtering. *physica status solidi c*, 7, 901-904.
- [140] **Rondiya, S., Rokade, A., Jadhavar, A., Nair, S., Chaudhari, M., Kulkarni, R., . . . Jadkar, S.** (2017). Effect of calcination temperature on the properties of CZTS absorber layer prepared by RF sputtering for solar cell applications. *Materials for Renewable and Sustainable Energy*, 62, 8.
- [141] **Padmavathi, S., & Vathi, P.** (2017). Resemblance or various incalescent annealing CIGS thin film using by flash evaporation method: growth, structural, compositional, optical and electrical properties. *International Journal of Innovative Research in Science, Engineering and Technology*, 67, 1111-1120.
- [142] **Touati, R., Rabe, M. B., & Kanzari, M.** (2014). Structural and Optical Properties of the New Absorber $\text{Cu}_2\text{ZnSnS}_4$ Thin Films Grown by Vacuum Evaporation Method. *Energy Procedia*, 44, 44-51.
- [143] **Lee, S. G., Kim, J., Woo, H. S., Jo, Y., Inamdar, A. I., Pawar, S. M., . . . Im, H. S.** (2014). Structural, morphological, compositional, and optical properties of single step electrodeposited $\text{Cu}_2\text{ZnSnS}_4$ (CZTS) thin films for solar cell application. *Current Applied Physics*, 143, 254-258.
- [144] **Lin, Y. P., Chi, Y. F., Hsieh, T. E., Chen, Y. C., & Huang, K. P.** (2016). Preparation of $\text{Cu}_2\text{ZnSnS}_4$ (CZTS) sputtering target and its application to the fabrication of CZTS thin-film solar cells. *Journal of Alloys and Compounds*, 654, 498-508.
- [145] **Shinde N.M., D. P. R., Patil S.V., Lokhande C.D.** (2013). Aqueous chemical growth of $\text{Cu}_2\text{ZnSnS}_4$ (CZTS) thin films: Air annealing and photoelectrochemical properties. *Materials Research Bulletin*, 48, 1760-1766.
- [146] **Singh O.P., N. M., Singh V.N., Singh B.P. .** (2015). Effect of annealing time on the composition, microstructure and band gap of copper zinc tin sulfide thin films. *Advanced Material Letters*, 6, 2-7.
- [147] **Khare A.W. A., A. L. M., Norris D. J. and Aydil E. S. .** (2011). Size control and quantum confinement in $\text{Cu}_2\text{ZnSnS}_4$ nanocrystals. *Chem. Commun.*, 47, 11721-11723.
- [148] **Riha, S. C., Parkinson, B. A., & Prieto, A. L.** (2009). Solution-Based Synthesis and Characterization of $\text{Cu}_2\text{ZnSnS}_4$ Nanocrystals. *Journal of the American Chemical Society*, 13134, 12054-12055.
- [149] **Deepa, K. G., Sajeesh, T. H., & Nagaraju, J.** (2017). Opto-Electronic Properties of $\text{Cu}_2\text{ZnSnS}_4$ Thin Films Grown by Ultrasonic Spray Pyrolysis. *Journal of Electronic Materials*, 471, 530-535. doi:10.1007/s11664-017-5803-3
- [150] **Liu, F., Zhang, K., Lai, Y., Zhang, Z., & Liu, Y.** (2010). Growth and characterization of $\text{Cu}_2\text{ZnSnS}_4$ thin films by DC reactive magnetron sputtering for photovoltaic applications. *Electrochemical and Solid State Letter*, 1311, 379-381.
- [151] **Scragg, J. J., Dale, P. J., Peter, L. M., Zoppi, G., & Forbes, I.** (2008). New routes to sustainable photovoltaics: evaluation of $\text{Cu}_2\text{ZnSnS}_4$ as an alternative absorber material. *Physica Status Solidi (b)*, 2459, 1772-1778.

- [152] **Rajeshmon, V., Kartha, C., Vijayakumar, K., Chinnappanadar, S., Abe, T., & Kashiwaba, Y.** (2011). Role of precursor solution in controlling the opto-electronic properties of spray pyrolysed Cu₂ZnSnS₄ thin films. *Solar Energy*, 852, 249-255.
- [153] **Tanaka, T., Nagatomo, T., Kawasaki, D., Nishio, M., Guo, Q., Wakahara, A., & Ogawa, H.** (2005). Preparation of Cu₂ZnSnS₄ thin films by hybrid sputtering. *Journal of Physics and Chemistry of Solids*, 6611, 1978-1981.
- [154] **Ito, K., Nakazawa, T.** (1988). Electrical and optical properties of stannite-type quaternary semiconductor thin films. *Japanese Journal of Applied Physics*, 2711, 2094–2097.





CURRICULUM VITAE

Name Surname : Elif PEKSU
Place and Date of Birth : Istanbul, 22.12.1984
E-Mail : elifpeksu@gmail.com



EDUCATION :

- **B.Sc.** : 2007, Trakya University, Faculty of Science and Letters, Department of Physics
- **M.Sc.** : 2013, Istanbul Technical University, Faculty of Science and Letters, Physics Engineering

PROFESSIONAL EXPERIENCE AND REWARDS:

- 2014-2015 Support from the Scientific and Technological Research Council of Turkey (TÜBİTAK), 3001, “Aluminyum Katkılanmış Çinko Oksit (AZO) İnce Filmlerin Sol-Gel Tekniği ile Üretilmesi ve Bunların Hibrid Güneş Pillerine Entegrasyonu”.
- 2017-2019 Support from the Scientific and Technological Research Council of Turkey (TÜBİTAK), 1003, “Düşük Maliyetli ve Yüksek Verimlilikli Transfer Edilebilir $\text{Cu}_2\text{ZnSnS}_4$ Tabanlı 3. Nesil Güneş Hücrelerin Üretimi”.

PUBLICATIONS, PRESENTATIONS AND PATENTS ON THE THESIS:

- **Peksu E.**, Karaağaç H. 2015. Synthesis of ZnO Nanowires and Their Photovoltaic Application: ZnO-Nanowires/AgGaSe₂ Thin Film Core-Shell Solar Cell, *Journal of Nanomaterials*, 2015 (516012), 1-10. (invited paper)
- **Peksu E.**, Karaağaç H. 2018. Doping and Annealing Effects on Structural, Electrical and Optical Properties of Tin-Doped Zinc- Oxide Thin Films, *Journal of Alloys and Compounds*, 764 (2018), 616-625.
- **Peksu E.**, Karaağaç H. 2019. A Third Generation Solar Cell Based on Wet-Chemically Etched Si Nanowires and Sol-Gel Derived $\text{Cu}_2\text{ZnSnS}_4$ Thin Films, *Journal of Alloys and Compounds*, 774 (2019), 1117-1122.
- **Peksu E.**, Terlemezoglu M., Parlak M., Karaağaç H. 2019. Characterization of one-step deposited $\text{Cu}_2\text{ZnSnS}_4$ Thin Films Derived From A Single Crystalline Powder, *Renewable Energy*, 143 (2019), 1133-1142.

- **Peksu E.**, Karaağaç H. 2016. Synthesis of one dimensional nanostructures for photovoltaic applications. İstatiksel Fizik Günleri- İFG 23, June 23-24, 2016 İstanbul Technical University, İstanbul Turkey.(oral presentation)
- **Peksu E.**, Karaağaç H. 2016. ZnO İnce Filmlerin Yapısal, Optiksel ve Elektriksel Özellikleri Üzerinde Sn Katkılamanın ve Isıl İşlemlerin Etkisi. 22. Yoğun Madde Fiziği – YMF Ankara Toplantısı, 16 Aralık 2016, Ankara Üniversitesi, Ankara, Türkiye.(oral presentation)
- **Peksu E.**, Karaağaç H. 2017. Doping and Annealing Effects on Structural, Electrical and Optical Properties of Tin doped Zinc Oxide (SZO) Thin Films. E-MRS 2017 Spring Meeting, May 22-26, 2017, Convention Center of Strasbourg, Strasbourg, France. (poster)
- **Peksu E.**, Terlemezoğlu M., Güller Ö., Parlak M., Karaağaç. H. 2018. Characterization of Electron- Beam Evaporation Cu₂ZnSnS₄ (CZTS) Films Using Single Crystalline Powder. PVCON 2018, July 4-6, 2018. Middle East Technical University, Ankara, Turkey. (poster)
- **Peksu E.**, Karaağaç H. 2018. The synthesis of Si NWs via a Route Based on Electroless Etching Technique and Polystyrene Nano-sphere Lithography. E-MRS 2018 Fall Meeting, September 17-20, 2018, Warsaw University of Technology, Warsaw, Poland. (poster)

OTHER PUBLICATIONS, PRESENTATIONS AND PATENTS:

Book/Chapter:

- H. Karaagac, **E. Peksu**, Arııcı E. U., İslam M.S., Ünlü H., Horing N.J.M., Dabowski J. (Ed.), Çeviri: 2015, One-Dimensional Nano-structured Solar Cells in Low- Dimensional and Nanostructured Materials and Devices- Properties, Synthesis, Characterization, Modelling and Applications. Chapter 15, pp. 351-400, *Springer International Publishing*, Switzerland. ISBN: 978-3-319-25338-1.

Oral Presentation:

- **Peksu E.**, Karaağaç H., İslam M.S. 2015. Synthesis of one- dimensional nanostructures for gas sensing and photovoltaic applications, SPIE Nanoscience + Engineering, August 09-13, 2015, San Diego Convention Center, San Diego, California, USA. (invited talk).

Articles and Proceedings:

- Karaağaç H., **Peksu E.**, İslam M.S. 2015. Synthesis of one- dimensional nanostructures for gas sensing and photovoltaic applications, *Proc. SPIE 9553, Low- Dimensional Materials and Devices*, 9553 (95530S), 1-11 (invited paper).
- Karaağaç H., **Peksu E.**, Behzad H., Akgöz S., Parlak M. 2017. Characterization of CuIn_{0.7}Ga_{0.3}Se₂ Thin Film Deposited by Single Stage Thermal Evaporation Process. *Physical Status Solidi C*, 14 (12), 17001451-7.
- Güller Ö., **Peksu E.**, Karaağaç H. 2017. Synthesis of TiO₂ Nanorods for Schottky-Type UV- Photodetectors and Third Generation Solar Cells. *Physical Status Solidi A*, 215 (4), 1700404 1-6.

- Behzad H., Ghodsi F. E., **Peksu E.**, Karaağaç H. 2018. The effect of Cu content on structural, optical and photo-electrical properties of sol-gel derived $\text{Cu}_x\text{Co}_{3-x}\text{O}_4$ thin films. *Journal of Alloys and Compounds*, 744 (2018), 470-480.
- Karaağaç H., Güller Ö., **Peksu E.**, Humali E., Terlemezoğlu M., Parlak M., Islam M. S. 2019. Transfer of ordered and disordered Si nanowires onto alien substrates for the fabrication of third-generation solar cells. *Proc. SPIE 10982, Micro and Nanotechnology Sensors, Systems, and Applications XI*, 10982 (1098205), 1-11.

Poster Presentations:

- **Peksu E.**, Karaağaç H. 2015. Characterization of Aluminum- Doped Zinc Oxide (AZO) Thin Films Prepared by Sol-Gel Technique and Their Use for a Hybrid Solar Cell Application. E-MRS 2015 Fall Meeting, September 15-18, 2015, Warsaw University of Technology, Warsaw, Poland.
- Akgöz S., **Peksu E.**, Karaağaç H. 2015. Structural, Optical and Electrical Properties of $\text{CuIn}_{0.9}\text{Ga}_{0.1}\text{Se}_2$ Thin Films Fabricated by Thermal Evaporation Technique. E-MRS 2015 Fall Meeting, September 15-18, 2015, Warsaw University of Technology, Warsaw, Poland.
- **Peksu E.**, Karaağaç H. 2016. Photovoltaic Application of Zinc Oxide and Aluminum- Doped Zinc Oxide (AZO) Thin Films/ Nanowires Fabricated via a Route Combinin Sol-Gel and Hydrothermal Techniques. E-MRS 2016 Spring Meeting, May 02-06, 2016, Lille Grand Palais, Lille, France.
- Behzad H., **Peksu E.**, Akgöz S., Karaağaç H. 2016. Characterization of Electron-Beam Deposited $\text{CuIn}_{0.5}\text{Ga}_{0.5}\text{Se}_2$ Thin Films For Photovoltaic Applications. E-MRS 2016 Spring Meeting, May 02-06, 2016, Lille Grand Palais, Lille, France.
- Behzad H., **Peksu E.**, Ghodsi. F. E., Karaağaç H. 2016. Characterization of Sol-Gel Derived $\text{Cu}_x\text{Co}_{3-x}\text{O}_4$ Thin Films For Photovoltaic Applications. E-MRS 2016 Spring Meeting, May 02-06, 2016, Lille Grand Palais, Lille, France.
- **Peksu E.**, Karaağaç H. 2016. Büyütme Parametrelerinin Sol-Jel Yöntemiyle Üretilen AZO İnce Film Özellikleri Üzerindeki Etkileri. 22. Yoğun Madde Fiziği – YMF Ankara Toplantısı, 16 Aralık 2016, Ankara Üniversitesi, Ankara, Türkiye.
- Güller Ö., **Peksu E.**, Karaağaç H. 2016. Hidrotermal Yöntemiyle Titanyum-Dioksit Nanoçubukların Sentezi ve Büyütme Parametrelerine Bağlı Fiziksel Özellikleri. 22. Yoğun Madde Fiziği – YMF Ankara Toplantısı, 16 Aralık 2016, Ankara Üniversitesi, Ankara, Türkiye.
- Güller Ö., **Peksu E.**, Karaağaç H. 2017 Synthesis of TiO_2 Nanorods for Schottky Type Photodetectors and Third Generation Solar Cells. E-MRS 2017 Spring Meeting, May 22-26, 2017, Convention Center of Strasbourg, Strasbourg, France.
- Karaağaç H., **Peksu E.**, Behzad H., Akgöz S., Parlak M. 2017 Preparation of $\text{CuIn}_{0.7}\text{Ga}_{0.3}\text{Se}_2$ Thin Films For The Fabrication of a Si Nanowires Based Third Generation Solar Cell. E-MRS 2017 Spring Meeting, May 22-26, 2017, Convention Center of Strasbourg, Strasbourg, France.
- Güller Ö., **Peksu E.**, Karaağaç. H. 2018. Transfer of Vertically Aligned Silicon Nanowires To Transparent – Conductive and Flexible Substrates For Realization of Third Generation Solar Cells. PVCON 2018, July 4-6, 2018. Middle East Technical University, Ankara, Turkey.

